MICROCOPY RESOLUTION TEST CHART

1.25   1.4   1.6

1.8

2.0   1.1

2.2

2.5   1.0

AFOSR·TR· 87-0180 ②
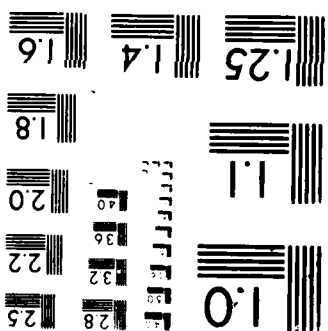
Annual Progress Report To:

The Air Force Office of Scientific Research

For the Project:

"Population Inversions in Ablation Plasmas Generated by Intense Electron Beams"
(AFOSR 86-0012)

Principal Investigators:
R. M. Gilgenbach
T. Kammash
M. L. Brake

Nuclear Engineering Department
The University of Michigan
Ann Arbor, MI 48109

DTIC
ELECTE
S
FEB 2 7 1987
D
D

November 1986

Intense Energy Beam Interaction Laboratory

Ronald M. Gilgenbach
Project Director
(313) 763-1261

Neil Gerl
Project Representative
(313) 763-6438

THE UNIVERSITY OF MICHIGAN 1817

87   2 20 180

REPORT DOCUMENTATION PAGE

1a. REPORT SECURITY CLASSIFICATION	1b. RESTRICTIVE MARKINGS
Unclassified	

2a. SECURITY CLASSIFICATION AUTHORITY	3. DISTRIBUTION/AVAILABILITY OF REPORT
	Approved for public release;
2b. DECLASSIFICATION/DOWNGRADING SCHEDULE	Distribution unlimited

4. PERFORMING ORGANIZATION REPORT NUMBER(S)	5. MONITORING ORGANIZATION REPORT NUMBER(S)
AFOSR Nov. 86	

6a. NAME OF PERFORMING ORGANIZATION	6b. OFFICE SYMBOL (If applicable)	7a. NAME OF MONITORING ORGANIZATION
Nuclear Engineering Dept. University of Michigan		Air Force Office of Scientific Research

6c. ADDRESS (City, State and ZIP Code)	7b. ADDRESS (City, State and ZIP Code)
Cooley Bldg., North Campus Ann Arbor, MI 48109	Bolling Air Force Base Washington, DC 20375 20332 6448

8a. NAME OF FUNDING/SPONSORING ORGANIZATION	8b. OFFICE SYMBOL (If applicable)	9. PROCUREMENT INSTRUMENT IDENTIFICATION NUMBER
Air Force OSR	NP	AFOSR 86-0012

8c. ADDRESS (City, State and ZIP Code)	10. SOURCE OF FUNDING NOS.			
Bolling Air Force Base Washington, DC 20375	PROGRAM ELEMENT NO.	PROJECT NO.	TASK NO.	WORK UNIT NO.
	61103F	2301	A3	

11. TITLE (Include Security Classification)
Population Inversions in Ablation Plasmas... (U)

12. PERSONAL AUTHOR(S)
R. M. Gilgenbach, T. Kammash and M. L. Brake

13a. TYPE OF REPORT	13b. TIME COVERED	14. DATE OF REPORT (Yr., Mo., Day)	15. PAGE COUNT
Annual Report	FROM 11/1/85 TO 11/1/86	1986 Nov. 30	88

16. SUPPLEMENTARY NOTATION

17. COSATI CODES			18. SUBJECT TERMS (Continue on reverse if necessary and identify by block number)
FIELD	GROUP	SUB. GR.	intense electron beams, e-beam pumping, anode plasma, spectroscopy

19. ABSTRACT (Continue on reverse if necessary and identify by block number)

We have performed extensive experiments to investigate the spectroscopic emission from electron beam driven carbon anode plasmas. Diode closure results in three phases of beam-plasma evolution which are summarized below:

Stage I: Deposited electron dose is smaller than that required for anode plasma formation. No light is detected in this phase.

Stage II: Deposited electron dose is large enough for anode plasma formation before the diode shorts. Spectroscopic data for noncrowbarred shots (dose $\approx$ 500-800 J/g) indicate the presence of CII and CIII with a high level of background radiation.

Stage III: Cathode plasma begins shorting A-K gap or anode and cathode plasmas meet. For crowbarred shots (dose > 300 J/g) molecular emission is observed from C_2 and CH. Atomic emission from CII and H. Noncrowbarred shots exhibit intense atomic emission; at early times CIII and CII are the primary components; however emission from CIV has also been

20. DISTRIBUTION/AVAILABILITY OF ABSTRACT	21. ABSTRACT SECURITY CLASSIFICATION
UNCLASSIFIED/UNLIMITED ☒ SAME AS RPT. ☐ DTIC USERS ☐	Unclassified

22a. NAME OF RESPONSIBLE INDIVIDUAL	22b. TELEPHONE NUMBER	22c. OFFICE SYMBOL
Col Weichel	202-767-4904	NP

DD FORM 1473, 83 APR   EDITION OF 1 JAN 73 IS OBSOLETE

observed. Electron temperatures from Boltzmann plots are 2-3 eV. At later times the emission is primarily from CI and CII with T_e 2-3 eV. The electron density is found to be N_e 10^{18} cm^{-3} from Saha equation.

A second thrust of our experimental program has been a study of electron beam induced optical emission in helium. In the course of this research we discovered a new effect which we published in Applied Physics Letters. Relativistic electron beam interactions with very small ratios of nitrogen to helium ($10^{-1}-10^{-4}$) have been found to produce extremely large N_2^+ ($B^2\Sigma_u^+ - X^2\Sigma_g^+$) intensities at 391.4 and 427.8 nm, compared to line intensities originating from helium. These results occurred in the total pressure regime of 0.1-500 Torr. The pressure scaling results discovered are inconsistent with previously proposed kinetic mechanisms for the N_2^+ laser pumped by helium. With a simple model of the chemical kinetics, we have shown that this effect is due to the collisional transfer of energy between excited states of helium atoms and the ground state of N_2^+.

The main goal of the theoretical investigation is to formulate a model which will describe the motion of the carbon plasma and predict the spectrum of emitted light. The predicted spectra may then be directly compared to spectra which are experimentally measured. The model being currently developed is based on previous work done by J. W. Thornhill under AFOSR sponsorship at Michigan. Three main areas must be addressed: hydrodynamic description of the plasma, an ionization dynamics model, and the energy deposition of the incident particle beam. Due to the complexity of the problem numerical methods are used to obtain results.

The main hydrodynamic assumption is that the plasma can be described using single fluid and temperature equations. This places a constraint on the time scale of the problem. Namely that the electron-ion thermalization time should always be smaller than the hydrodynamic time. This constraint is not serious but should be kept in mind. The model is developed in one dimensional Lagrangian coordinates. This simplifies the conservation equations and allows for simulation of situations where extensive compression or expansion occurs.

The Collisional-Radiative Equilibrium (CRE) model is used to describe the ionization dynamics of the system. This model consists of a set of rate equations, one for each quantum state included, which describe the effect of atomic processes on the population and depopulation of a given state. The model used is an equilibrium model since no time dependence is included in the rate equations.

The final component of our theory is the energy depositon model. The approach is simplistic at the present. The stopping power of an incident relativistic electron is integrated over the plasma. This is then multiplied by the current density of the beam at each point in the plasma to obtain the desired result. The stopping power is based on a formalism for relativistic electrons interacting with a plasma which has both free and bound electrons. A collision term was found using Fokker-Planck formalism. Assuming the incident beam can be treated as a delta function in momentum space, the appropriate moment of the collision term yields the stopping power.

Table of Contents

Accesion For

NTIS CRA&I	N
DTIC TAB	[]
U:ianno..iced	[]
Justification	

By
Distribution /

Availability Codes

Dist	Avail a d / or Special
A-1	

DTIC
COPY
INSPECTED
6

Executive Summary

We have performed extensive experiments to investigate the spectroscopic emission from electron beam driven carbon anode plasmas. Diode closure results in three phases of beam-plasma evolution which are summarized below:

Stage I: Deposited electron dose is smaller than that required for anode plasma formation. No light is detected in this phase.

Stage II: Deposited electron dose is large enough for anode plasma formation before the diode shorts. Spectroscopic data for noncrowbarred shots (dose $\approx$ 500-800 J/g) indicate the presence of CII and CIII with a high level of background radiation.

Stage III: Cathode plasma begins shorting A-K gap or anode and cathode plasmas meet. For crowbarred shots (dose > 300 J/g) molecular emission is observed from C_2 and CH. Atomic emission from CII and H. Noncrowbarred shots exhibit intense atomic emission; at early times CIII and CII are the primary components, however emission from CIV has also been observed. Electron temperatures from Boltzmann plots are 2-3 eV. At later times the emission is primarily from CI and CII with $T_e \approx$ 2-3 eV. The electron density is found to be $N_e \approx 10^{18}$ cm^{-3} from the Saha equation.

A second thrust of our experimental program has been a study of electron beam induced optical emission in helium. In the course of this research we discovered a new effect which we published in Applied Physics Letters. Relativistic electron beam interactions with very small ratios of nitrogen to helium (10^{-1}-10^{-4}) have been found to produce extremely large $N_2^+(B^2\Sigma_u^+$-$X^2\Sigma_g^+)$ intensities at 391.4 and 427.8 nm, compared to line intensities originating from helium. These results occurred in the total pressure regime of 0.1-500 Torr. The pressure scaling results discovered are inconsistent with previously proposed kinetic mechanisms for the N_2^+ laser pumped by helium. With a simple model of the chemical kinetics, we have shown that this effect is due to

the collisional transfer of energy between excited states of helium atoms and the ground state of N_2^+.

The main goal of the theoretical investigation is to formulate a model which will describe the motion of the carbon plasma and predict the spectrum of emitted light. The predicted spectra may then be directly compared to spectra which are experimentally measured. The model being currently developed is based on previous work done by J.W. Thornhill under AFOSR sponsorship at Michigan. Three main areas must be addressed: hydrodynamic description of the plasma, an ionization dynamics model, and the energy deposition of the incident particle beam. Due to the complexity of the problem numerical methods are used to obtain results.

The main hydrodynamic assumption is that the plasma can be described using single fluid and temperature equations. This places a constraint on the time scale of the problem. Namely that the electron-ion thermalization time should always be smaller than the hydrodynamic time. This constraint is not serious but should be kept in mind. The model is developed in one dimensional Lagrangian coordinates. This simplifies the conservation equations and allows for simulation of situations where extensive compression or expansion occurs.

The Collisonal-Radiative Equilibrium (CRE) model is used to describe the ionization dynamics of the system. This model consists of a set of rate equations, one for each quantum state included, which describe the effect of atomic processes on the population and depopulation of a given state. The model used is an equilibrium model since no time dependence is included in the rate equations.

The final component of our theory is the energy deposition model. The approach is simplistic at the present. The stopping power of a incident relativistic electron is integrated over the plasma. This is then multiplied by the current density of the beam at each point in the plasma to obtain the desired result. The stopping power is based on a formalism for relativistic electrons interacting with a plasma which has both free and bound electrons. A collision term was found using Fokker-Planck formalism. Assuming the incident beam can be treated as a delta function in momentum space, the appropriate moment of the collision term yields the stopping power.

1.0) Spectroscopy of Electron Beam Induced and Driven Carbon Plasmas

1.1) Experimental Configuration

These experiments are being performed on MELBA (Michigan Electron Long Beam Accelerator) at the University of Michigan. MELBA is driven by a state of the art, long pulse Marx bank with a special Abramyan, reverse-charged capacitor stage for voltage compensation. Typical MELBA parameters that have been obtained are peak voltages < 1 MV, currents < 30 kA, and pulselengths = 0.3 - 4.0 μs. In this section the experimental equipment and configuration are described. In addition some improvements are noted for future experiments where appropriate.

The principal idea in the Abramyan concept is illustrated in Figure 1.1. The voltage $V_k(t)$ is the reverse-charged stage voltage. This is positive initially, with a maximum of about 60 kV, subtracting from the main Marx voltage $V_g(t)$. Note $V_g(t)$ droops due to the natural RC decay of the Marx. This decay is exacerbated with a cold cathode diode load due to collapsing diode impedance. Later in the pulse the reverse charged stage rings negative, adding on to the main Marx voltage. The combination of initial subtraction and later addition of the Abramyan voltage is intended to give the flat total voltage pulse $V_g(t)+V_k(t)$. The design goals were to compensate for an impedance collapse of a diode from 300 Ω to 50 Ω in 1.075 μs, and giving a voltage flat to within ±10%. Figure 1.2 shows comparison of experiment with theory for compensation of the RC decay into a 127 Ω fixed resistive load. Compensation has also been demonstrated with large gap diodes.[1.1]

The MELBA circuit with diode load is shown in Figure 1.3. It displays several important machine features in addition to the Abramyan stage, here represented by the elements R_A, C_A, V_A, L_A. The crowbar circuit, in parallel with the diode load, is designed to switch the voltage away from the diode by shunting the majority of the current to ground. The crowbar gap, a high pressure SF_6 switch, can be command triggered with different time delays in order to obtain different pulselengths. The diode load is represented by the stalk inductance L_S = 400 nh, and a time changing diode
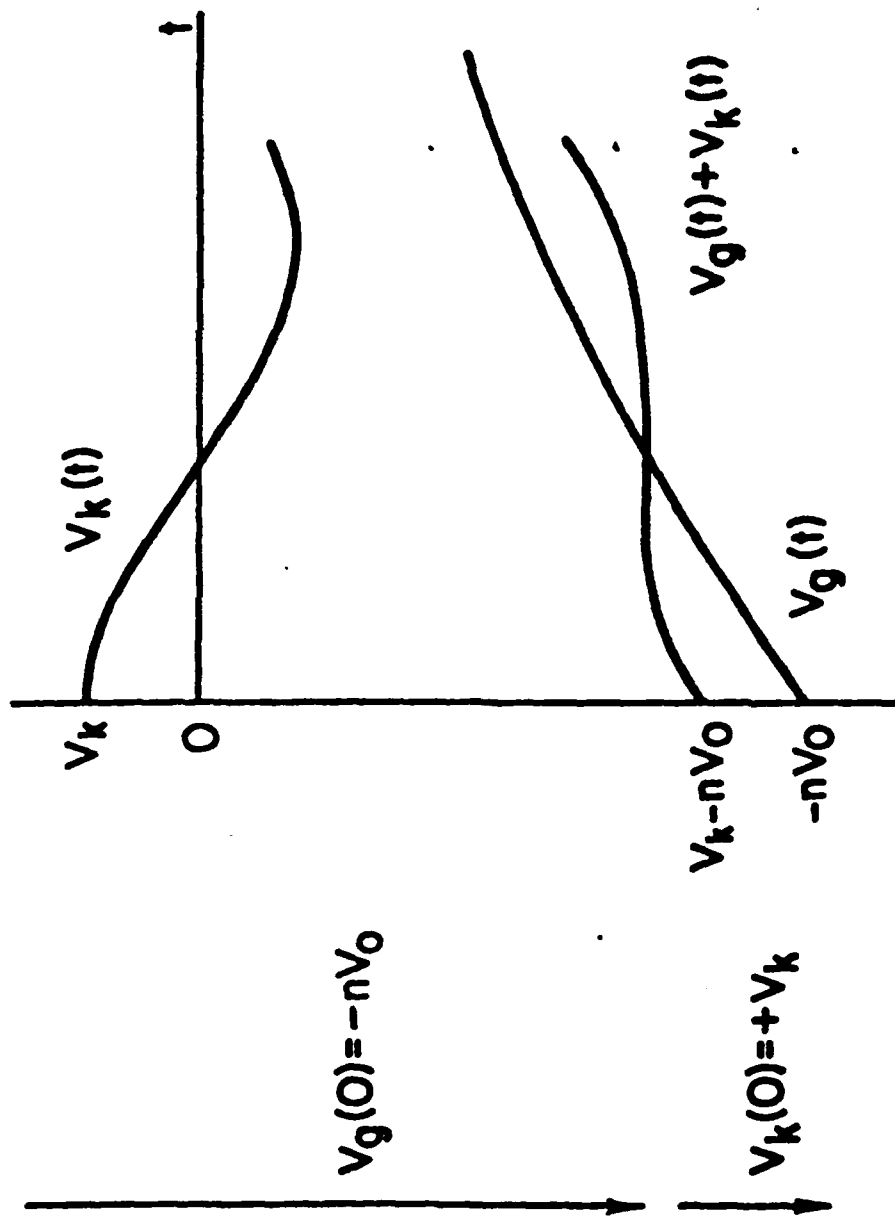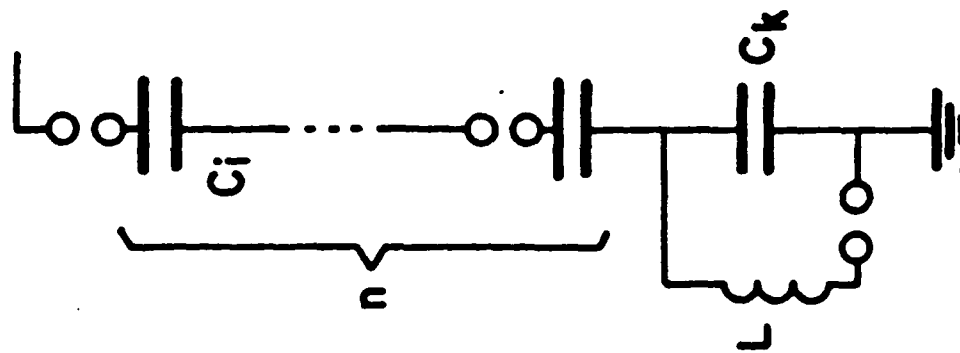
3

ABRAMYAN CIRCUIT CONCEPT

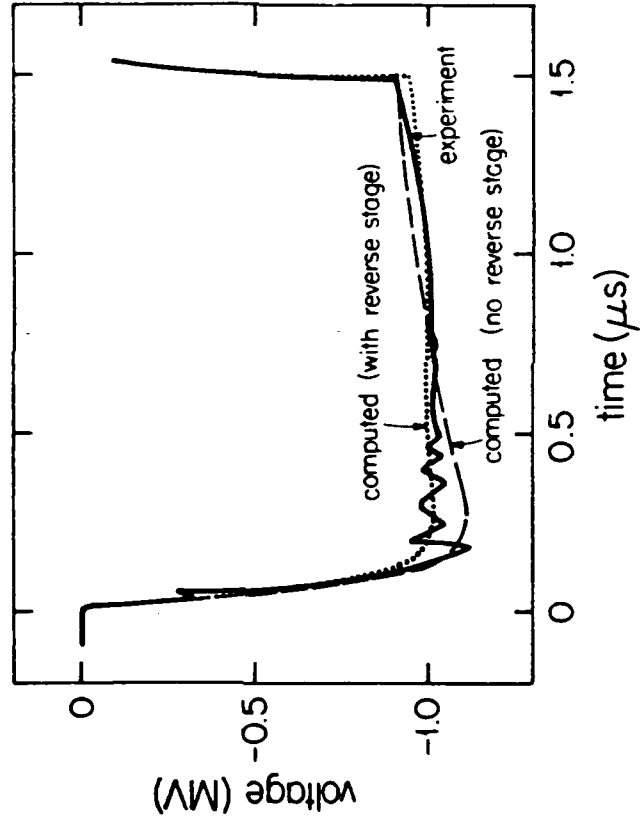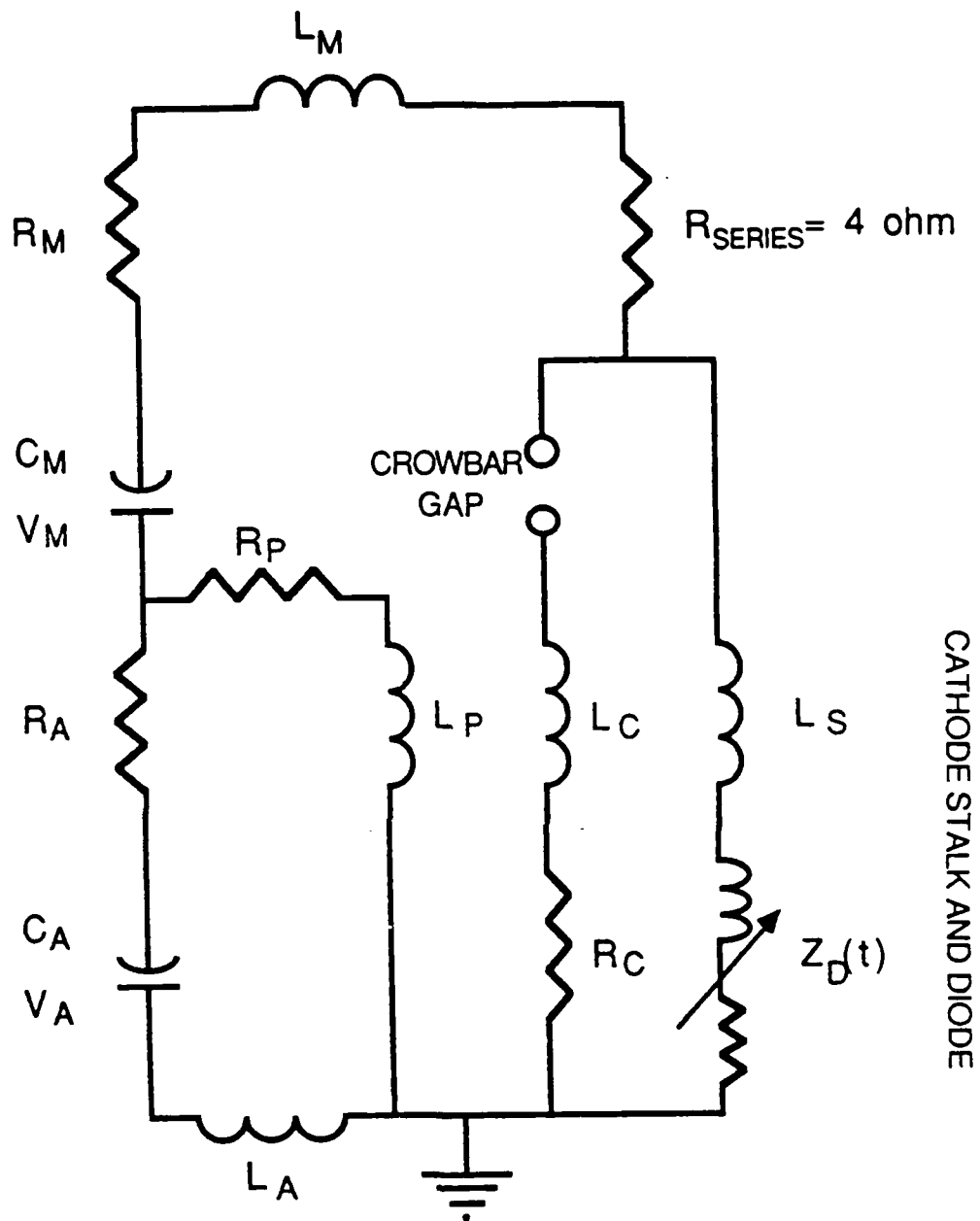Figure 1.1

MELBA OUTPUT VOLTAGE INTO 127 OHM RESISTIVE LOAD

Figure 1.2

SIMPLIFIED MELBA CIRCUIT DIAGRAM

Figure 1.3

impedance $Z_D(t)$ with both inductive and resistive components. The other important feature is the presence of a large series resistance $R_{SERIES} = 4.0$ Ω, intended to take the full generator energy in a crowbar or in the event of a diode short to prevent Marx damage. This resistor plays an important role in determining load dynamics when $R_D < R_{SERIES}$, a case which occurs for smaller gaps and late in time after gap closure has occurred.

The typical stored energy in the Marx bank is 25 kJ. In experiments with large diode gaps (8 - 10 cm) energies of 10 kJ have been delivered to the anode at low current densities (<20 A/cm^2). The experiments discussed in this report were performed at intermediate gaps (3 - 4 cm) and have delivered up to 7 kJ at current densities one to two orders of magnitude larger (>100 A/cm^2). The present study indicates that the critical parameter is not the total delivered energy but the energy density or dose, D (J/gr), which requires knowledge of the current density. In the large gap experiments $D \cong 20$ J/gr. The dose for the intermediate gap experiments was increased by one to two orders of magnitude, resulting in more intense atomic optical emission.

The most recent improvements in the experimental configuration were:

    i)   higher electron current densities by using shorter gaps,

    ii)   exclusive use of noncrowbarred shots,

    iii) extended anode to view plasma immediately on the face,

    iv)   and different cathode and anode materials to distinguish
            cathode plasma from anode plasma.

Further improvements in current density from gap reduction can still be made. In addition, we have designed pulsed magnetic field coils for the diode which have been built by an outside contractor. We are installing them on the diode chamber . The maximum field on axis expected will be 10 KG. The external field will result in increases in current density.
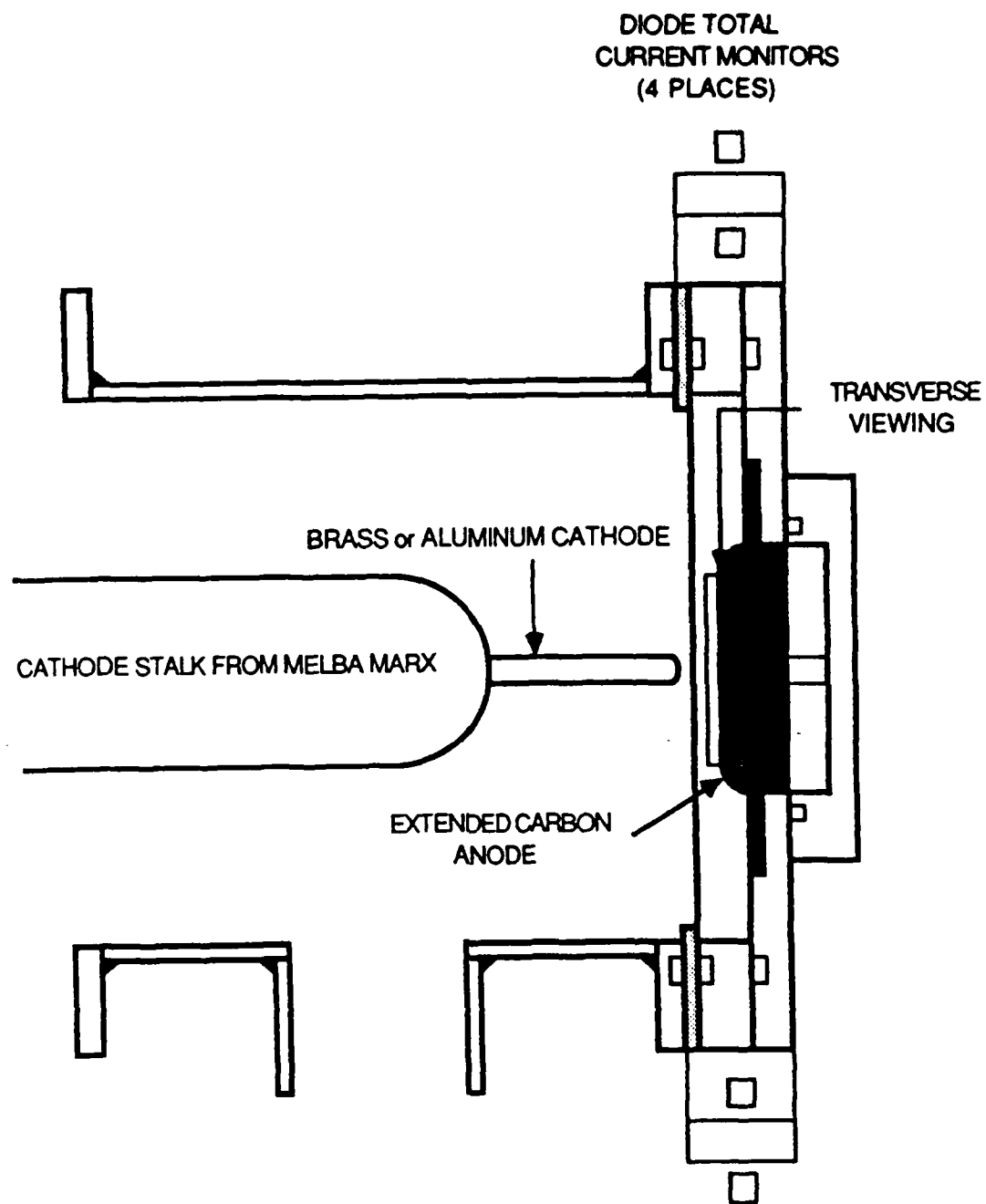
The principle reason that noncrowbarred shots are so desirable is that the current density increases very quickly late in time as the plasma nears closure. This greatly enhances the anode dose. The difference between

7

crowbarred and noncrowbarred shots is an increase in total dose by a factor of two to four by the end of the pulse. The use of different anode and cathode materials in order to distinguish the plasma source is a significant advantage. The cathode plasma components are pump oil and hydrocarbon impurities C_2, CH, H, as well as neutral and singly ionized carbon and cathode metal components. The carbon components from the cathode plasma do not interfere with distinguishing carbon produced from the anode as they are much cooler and contain significant molecular constituents.

The diode configuration is shown in Figure 1.4. The cathodes used were made of either brass or aluminum, with a small cross sectional area and had a blunt nose. One method of making further improvements in the incident current density is to make the cathode have a sharp point. Figure 1.4 also shows the extended anode.
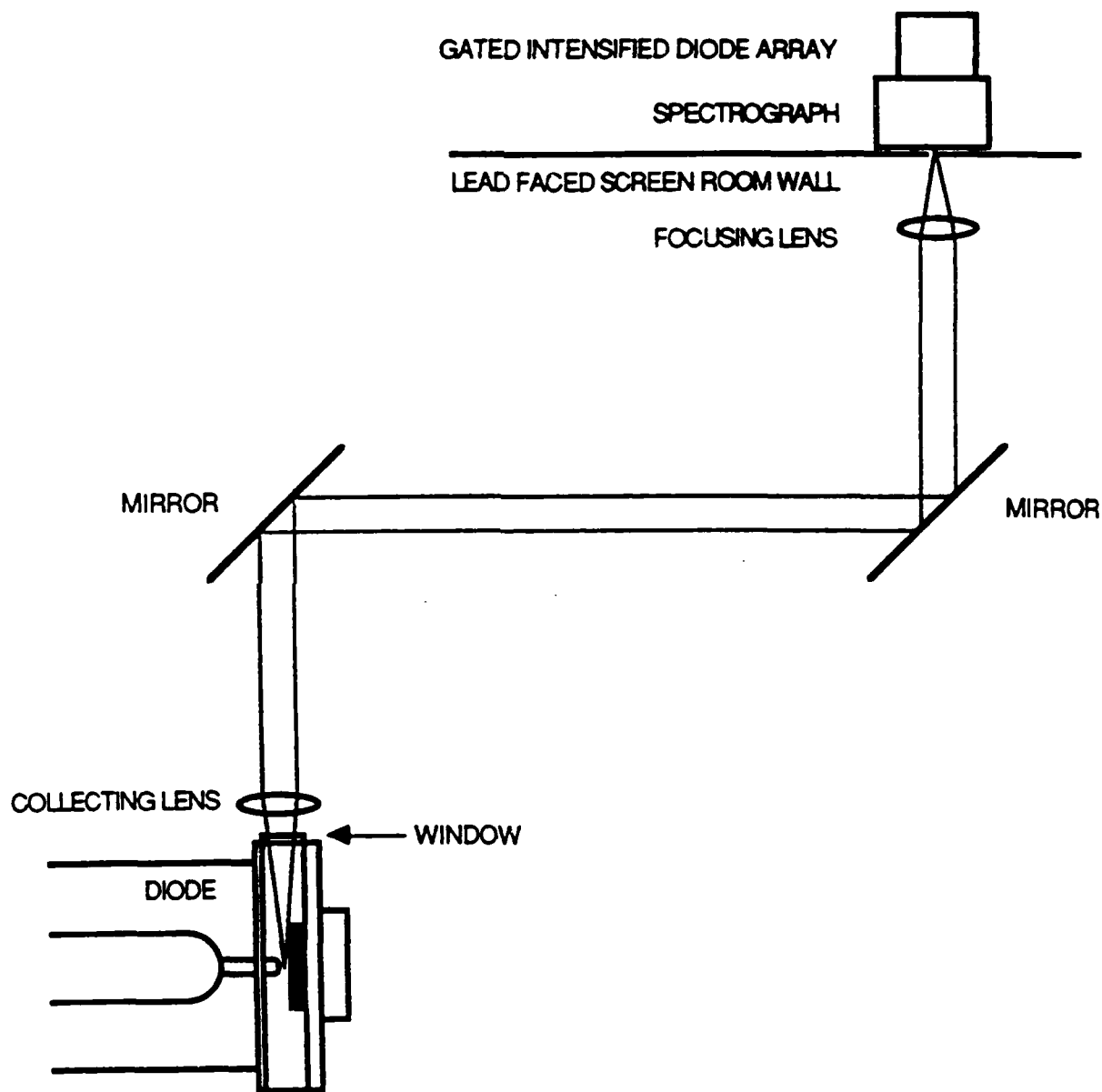
The method of light detection and measurement is shown in Figure 1.5. The initial collecting lens is intended to collimate the source light which is transmitted to the optical multichannel analyzer (OMA) via mirrors and a final focusing lens. Without taking into account the finite optical depth of the lenses, the system has a spatial resolution of about 100 μm, the size of the final slit ($M_T \cong 1$). In experiments thus far the light has never been perfectly collimated. The acrylic windows we are using in the current experiments have a cut off for transmission below about 3800 Å. Future experiments at shorter wavelengths will require quartz optics and windows and an evacuated optical path. Some of the quartz lenses have been already purchased. The acrylic windows become clouded with a film by the carbon vapor and cannot be cleaned with conventional methods. The quartz windows can be recovered to new optical quality by baking them at 450 °C for 24 hours.

The OMA equipment is housed in a lead faced screen room to prevent damage to the sensitive electronics by hard x-rays. The OMA consists of a 0.275 meter Jarell Ash spectrograph and a Tracor Northern 1024 channel gated intensified diode array. Plans are being made to replace the 0.275 meter spectrograph with a 1.0 meter version (supported by AFOSR), greatly increasing our resolution capabilities. For example, typical best resolution for the 0.275 meter spectrograph is about 10 Å. This is expected to be reduced to 0.2 Å with the 1.0 meter model.

DIODE TOTAL
CURRENT MONITORS
(4 PLACES)

TRANSVERSE
VIEWING

BRASS or ALUMINUM CATHODE

CATHODE STALK FROM MELBA MARX

EXTENDED CARBON
ANODE

DIODE CONFIGURATION

Figure 1.4

GATED INTENSIFIED DIODE ARRAY

SPECTROGRAPH

LEAD FACED SCREEN ROOM WALL

FOCUSING LENS

MIRROR

MIRROR

COLLECTING LENS

WINDOW

DIODE

EXPERIMENTAL CONFIGURATION

Figure 1.5

1.2) Experimental Modeling

1.2.a) Diode Analysis

One of the principle features of this beam-plasma experiment different from others is that the interaction occurs in the diode region. Plasma formed in the diode affects the electron beam coupling as a result of the diode dynamics and the diode-generator coupling. For example, the formation of an anode plasma in an electron diode can result in an increased electron current due to space charge neutralization. It may also short out the diode faster if it has a finite velocity. Another possibility is that it may increase the demands on the generator or the cathode plasma more quickly or past the point where they can be supplied, resulting in an opening of the gap, rather than continued impedance collapse. Thus diode physics is an important part of this study in determining details about the beam plasma coupling.

An idealized, pictorial example of the diode time development is shown in Figure 1.6. The position of the OMA gate relative to these possible light producing events in the diode determines the source of the detected light. Thus diode physics is also important in order to determine what is happening in the diode when the OMA is gated. An extended analysis and modeling o⁴ the voltage and current is required. For the purposes of this discussion and modeling, the evolution of the diode proceeds through three stages, defined in Figure 1.7 and as follows.

STAGE I - Initial stages of cathode plasma formation and expansion. The anode dose is below that required for anode plasma formation. No light would be detected.

STAGE II - In this stage the dose exceeds some minimum required dose for anode plasma formation before the cathode plasma has completely crossed the gap and shorted the diode. In response to the presence of anode ions, we expect a bipolar current. The anode plasma may or may not close. Some shots may not have this stage. In electron diodes, carbon anode plasmas are

11

IDEALIZED DIODE TIME DEVELOPMENT

THE POSITION OF THE OMA GATE RELATIVE TO THESE POSSIBLE LIGHT
PRODUCING EVENTS DETERMINES THE SOURCE OF THE DETECTED LIGHT.
AN EXTENDED ANALYSIS IS REQUIRED IN ORDER TO ASSESS WHICH ARE
OCCURING DURING THE GATE.

STAGE I - DOSE SMALLER THAN THAT REQUIRED FOR ANODE PLASMA FORMATION
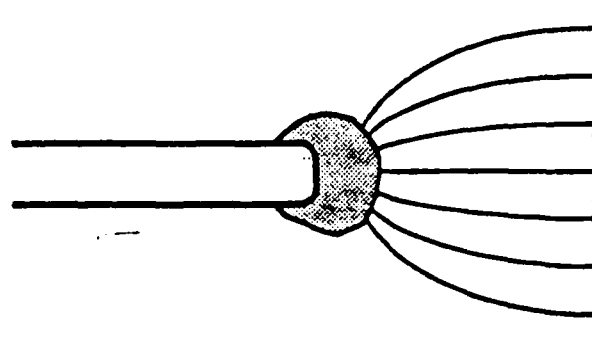
STAGE II - DOSE LARGE ENOUGH TO FORM ANODE PLASMA BEFORE SHORTING
(SOME SHOTS MAY NOT HAVE THIS STAGE)
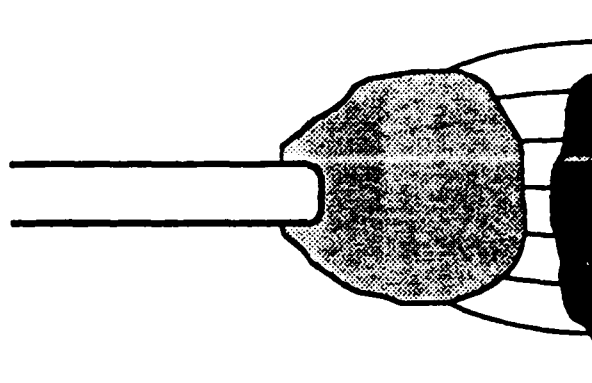
STAGE III

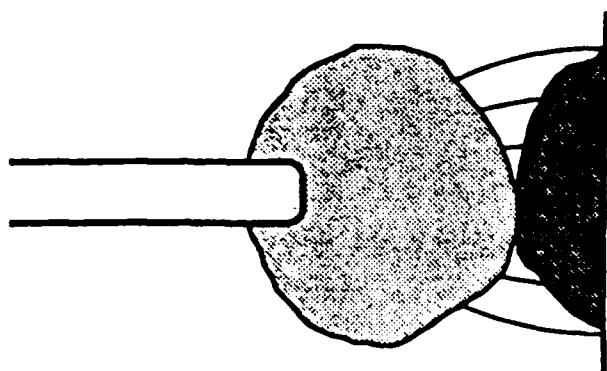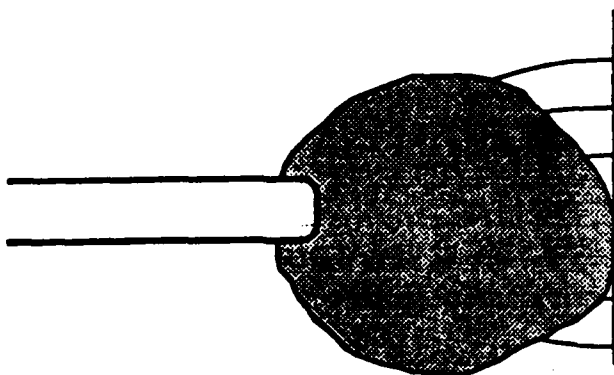CATHODE PLASMA BEGINS SHORTING   OR   ANODE AND CATHODE PLASMAS
MEET AND SHORT GAP

Figure 1.6

expected to be formed between 350 and 600 J/gr. These plasmas are formed from ionized carbon vapor from a heated outgassing carbon anode. The vaporization dose for direct carbon sublimation is $\equiv$ 56 kJ/gr at a temperature of 3600 $^{\circ}$C.

STAGE III- If no anode plasma has formed, then the cathode plasma starts to short out the gap. As the plasma gradually fills the whole diode and touches the entire anode surface, the emission surface for space charge emitted electrons is gradually shut off and the diode acts in more of a glow discharge or vacuum arc mode. This is a transition region where both an electron beam and an arc exist. For shots which have had a stage II, the anode and cathode plasmas meet and the same type of gradual transition takes place. We distinguish between early, middle and late divisions of stage III. Early stage III contains the transition region, thus is a mixture of beam and arc.

What follows is a discussion of the diode physics necessary to determine the events in the diode and the stage for a particular shot. It includes a discussion of diode closure analysis, a simple diode current model and an anode dose model. The diode closure analysis yields the cathode closure velocity u, (an input to the current model and the dose model), and effective diode area, (an input to the current model). The closure velocity analysis gives the expected cathode plasma diode shorting time T_{SHORT}. The position and width of the OMA gate relative to this time is important for two reasons. First it gives an estimate of the time to expect the transition to the arc mode, and secondly when to expect cathode plasma components to become visible. We must keep in mind that this velocity is only an apparent, average uniform velocity for the cathode plasma. The actual plasma probably has faster and slower components and is nonuniform. Use of this velocity is valid for comparison since the same method is applied for each shot.

The ability to model the diode current is important in order to verify that the diode is behaving in a mode we understand, and to ascertain when bipolar effects may come into play. This would give some confirming

13

evidence for the presence of an anode plasma. Finally, the dose model, here only a crude estimate of the incident electron energy density, again gives some indication of whether to expect an anode plasma during the OMA gate, and to tentatively decide what stage the shot is in. The dose model is more certain in the portion of the pulse that can be modeled well by space charge. Again the uncertainty in the dose model is unimportant as all shots are treated identically. An accurate determination of the dose would require an actual measurement of current density, rather than current. Following the theory discussion is a sample application to modeling idealized data.

i) Diode Closure

The Child -Langmuir law for a space charge limited infinite planar diode is given by:

$$I_{CL} = \frac{2.336 \times 10^{-6} \, \Pi \, (KR_C)^2 V^{3/2}}{(d_0 - u_c(T - T_{START}))^2} \qquad (1.1)$$

In this equation, d_0 is the initial gap spacing, u_c is the cathode plasma closure velocity, R_C is the cathode radius, T_{START} is the start of the Child Langmuir behavior region or the diode opening time, and K is a constant ($\neq 1$) to account for relativistic, nonplanar, and ion effects.

To perform the closure analysis solve Equation 1.1 for the denominator:

$$d_{eff}(t) = d_0 - u_c(T - T_{START}) = 2.709 \times 10^{-3} R_{eff}(1/P)^{1/2} \qquad (1.2)$$

In this equation $P = I_{exp}/V_{exp}^{3/2}$, and $R_{eff} = KR_C$. Now perform a linear best fit to the quantity $(1/P)^{1/2}$ determined from experimental data. The fit should be performed between the times T_{START} and T_{END}. These times are chosen so that the fit has a high correlation coefficient which signifies that the space charge flow model is expected to give a good match to the data. The best fit yields the equation $(1/P)_{fit}^{1/2} = A - B(T - T_{START})$ where A and B are the intercept and slope respectively of the best fit line to points between T_{START} and T_{END}. The $(1/P)^{1/2}$ best fit analysis is depicted

14

in Figure 1.7. Substitute this fit for $(1/P)^{1/2}$ in Equation 1.2 to obtain the best fit representation for $d_{eff}(t)$. Now define $T_{SHORT} = d_0/u_c + T_{START}$. At $T = T_{SHORT}$ d_{eff} is defined to be zero. Use this property in the best fit representation for $d_{eff}(t)$ above and solve for u_C:

$$U_c = d_0 B / A \qquad (1.3)$$

Other estimates of the shorting time, for example d_{eff} is zero at T_{END} will yield the same estimate for u_C. The quantity R_{eff} can also be determined from this same best fit analysis. Assuming that at T_{START}, d_{eff} is physically equal to the initial gap spacing d_0 yields:

$$R_{eff}^{fit} = KRc = \frac{d_0}{2.709 \times 10^{-3} A} \qquad (1.4)$$

ii) Current Model

The diode closure analysis yields both u_C and R_{eff}^{fit}. Thus a model for the diode perveance during the space charge portion of the pulse is completely determined by the linear best fit to $(1/P)^{1/2}$.

$$\frac{I_{exp}(t)}{V_{exp}(t)^{3/2}} = P_{exp}(t) = P_{model}(t) = \frac{2.336 \times 10^{-6} \Pi R_{eff}^2}{(d_0 - u_c(T - T_{START}))^2} \qquad (1.5)$$

The currents predicted by this model match the experimental currents well until near T_{END}. Recall that T_{END} was chosen to give the best fit with the highest correlation coeficient. The match of the current model to measured current, the real indicator of pure space charge behavior, is now used to fine tune the position of T_{END}. T_{END} is adjusted so that for $T > T_{END}$ the unipolar space charge model does not match the experimental data. Again this procedure is illustrated in Figure 1.7.

Another informative rearrangement of the space charge equation involves solving for the R_{eff} required in order to match the instantaneous experimental current:

$$R_{eff}(t) = 369.14[d_0 - u_c(T - T_{START})] [P_{exp}(t)]^{1/2} \qquad (1.6)$$

The best fit R_{eff} oscillates around the instantaneous Reff(t) during the portion of the pulse where the space charge model is a good match (as expected). After T_{END} , $R_{eff}(t)$ decreases towards zero, a decrease in the effective diode perveance, corresponding to a change in diode operating mode, possibly representing the transition to an arc. The diode or load resistance continues to drop during the transition. At this point the resistance of the load is only a few ohms. In the limit of zero load resistance, the series resistor limits the generator current to $\cong V/4 \le 25$ kA for voltages late in the pulse. This current is approximately the limit on late time current measured. The shot to shot variation of R_{eff} and u is large. Physically this represents a changing effective diode load. Thus the reproducability of the shots is poor. This is another reason why comparisons require an extended analysis.

iii) Dose Analysis

The dose is calculated by performing the integral:

$$D(t) = \int_0^{T_{END}} \frac{J(t)V(t)}{R[V(t)]} dt + \int_{T_{END}}^{T_F} \frac{I(t)V(t)}{AR[V(t)]} dt \qquad (1.7)$$

where J(t) is given by Child-Langmuir scaling with best fit closure velocity (Equation 1.1 divided by $\Pi(KR_c)^2$), R[V(t)] is the CDSA range in gm/cm^2 fit as a function of voltage, T_F is the limit of recorded data, and A is the plasma cross sectional area $\approx \Pi R_c^2$. This formulation neglects conduction effects in the affected electron maximum range thick anode layer, a valid assumption for the short timescale of the pulselength. The first integral contains the contribution from space charge flow in the diode. The second is a conservative estimate of the dose from the period of the pulse were space charge flow for the current is not a good model

(after T_{END}). This period contains the transition region and the full arc mode. The first part of the integral is by far the largest contribution. Note that this integral requires a cutoff when Child Langmuir scaling is used for J(t). If the integration is performed until $T = T_{SHORT}$, the integral will diverge. Setting the cutoff at T_{END} is a conservative estimate.

An approximate analytical form of this analysis predicts that in the space charge phase higher doses are delivered for slower closure velocities for a given initial gap spacing:

$$D_{SPACECHARGE} \approx \frac{4.25\,Vo}{dou}\ln[1/(1-C)] \tag{1.8}$$

In Equation 1.8, D is in KJ/gr, u in cm/μs, Vo, the peak voltage in MV, do the initial gap spacing in cm, and $C = T_{END}/T_{SHORT}$ some fraction of T_{SHORT} in order to make the result finite. Higher doses are also delivered for smaller initial gaps. Although J(t) increases faster for higher u, the limits of integration are cutoff sooner, leading to lower doses. The analysis also shows that the increase in dose due to range shortening at lower voltages is offset by the decrease due to smaller electron current densities, and the dose actually increases with Vo.

iv) Idealized Data

An idealized version of typical noncrowbarred experimental data and analysis is shown in Figure 1.7. This is an aid to developing and understanding the voltage and current analysis. There are several important features displayed in this figure. The position and width of the OMA gate is of course variable. The voltage always displays the peaking up or opening behavior late in time as if the load impedance were increasing. In previous experimental analysis we thought that the dip in voltage was associated with arcs or anomalous crowbar behavior. The current modeling implies that the peaking behavior is anomalous. The peaking behavior is inconsistent with falling diode resistance which is expected due to closure or because of anode initiated bipolar effects. Diode inductive effects in response to pinching are not large enough to cause such a large

17

voltage increase. Also note that in the modeling of the current, bipolar effects are not invoked. However, that model does not agree with experiment, starting at the beginning of this opening behavior. Often, the dose at that point is well into the range for expected anode plasma formation, which is consistent with experiments where light is measured. The final feature to note is that the predicted shorting time is usually well after the end of the voltage "opening". Some theories consistent with these observations involve the load-generator coupling.

After the anode plasma is formed due to some required dose being surpassed, the impedance of the diode will drop by almost a factor of two, immediately demanding more current from the generator. If the demand is greater than the generator can supply, or the cathode plasma density is not large enough to meet extraction demands, the cathode and/or anode plasma emissive surface may be pushed back and the gap opens. This type of voltage peaking can also be created by nonuniform filling of the space charge potential in the gap or by load mismatch effects. The understanding of this behavior is very important since it seems to be related to anode plasma production and is required for a clear interpretation of the spectra.

We have developed an interactive, graphical computer code EDIODE3, which greatly enhances our diode analysis and understanding. This code is based on the physics discussed in the current section. Figure 1.8 is a flow chart showing the analysis pathway. Figure 1.17 is an example of the code output.
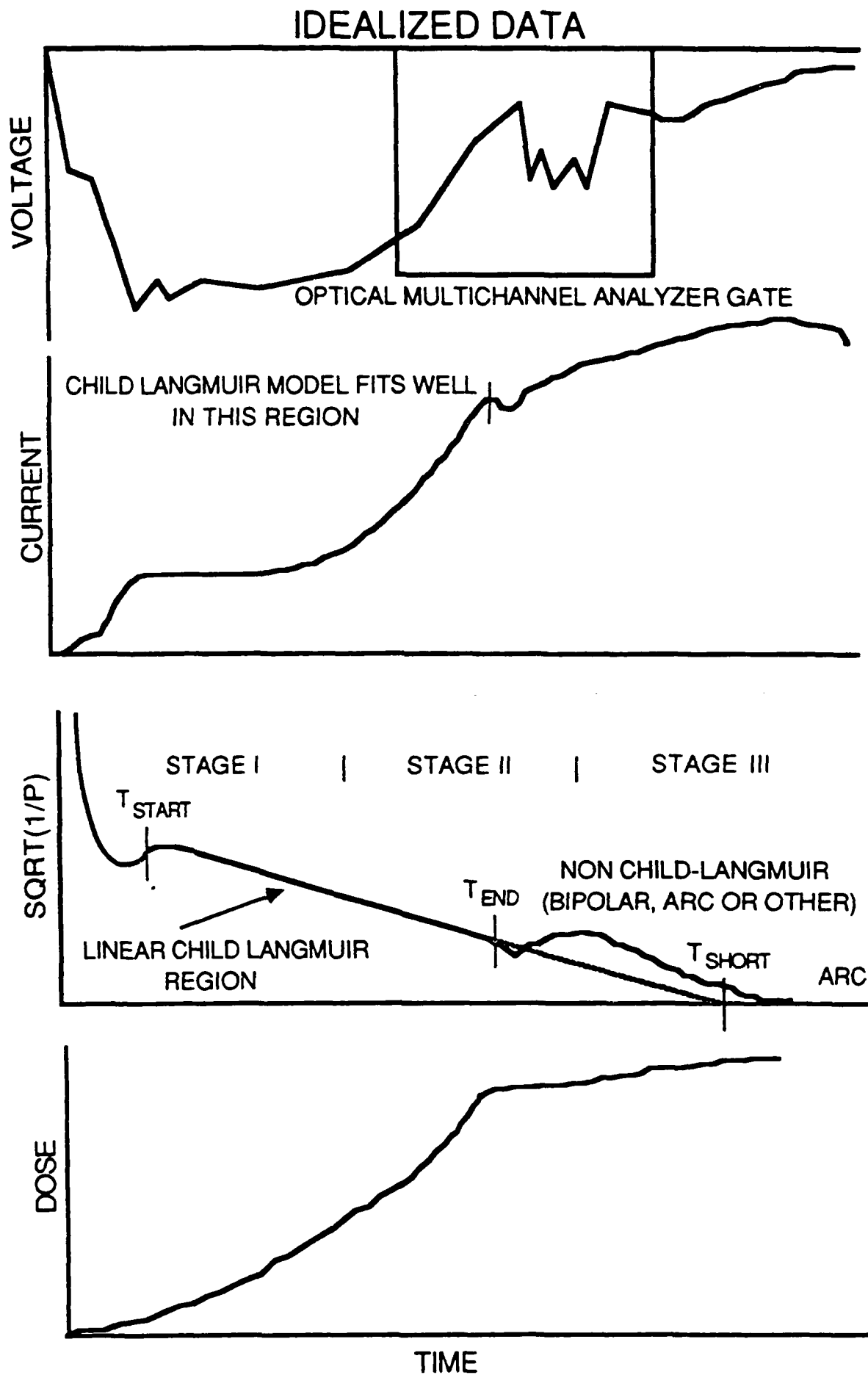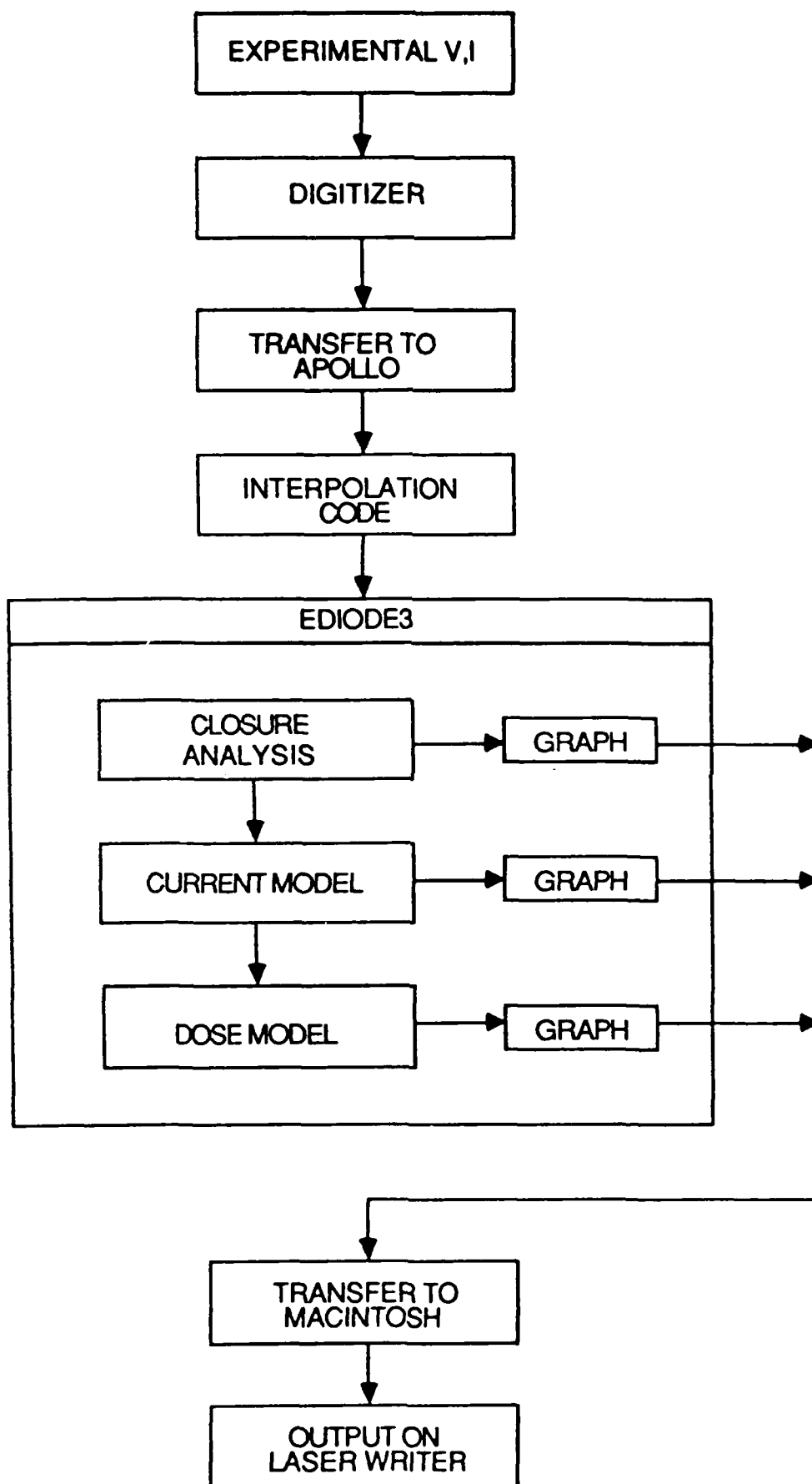
IDEALIZED DATA

VOLTAGE

OPTICAL MULTICHANNEL ANALYZER GATE

CURRENT

CHILD LANGMUIR MODEL FITS WELL
IN THIS REGION

SQRT(1/P)

STAGE I | STAGE II | STAGE III

T_{START}

T_{END}

NON CHILD-LANGMUIR
(BIPOLAR, ARC OR OTHER)

T_{SHORT}

ARC

LINEAR CHILD LANGMUIR
REGION

DOSE

TIME

Figure 1.7

```
EXPERIMENTAL V,I
        |
        v
    DIGITIZER
        |
        v
  TRANSFER TO
    APOLLO
        |
        v
  INTERPOLATION
      CODE
        |
        v
```

EDIODE3

CLOSURE ANALYSIS → GRAPH

CURRENT MODEL → GRAPH

DOSE MODEL → GRAPH

TRANSFER TO MACINTOSH

OUTPUT ON LASER WRITER

Figure 1.8

1.2.b) Spectral Analysis

i) Theory

Some of the principle goals in plasma emission spectroscopy are to determine the plasma constituents, densities, and temperatures. These properties can often yield information about the state of the plasma, whether it be equilibrium or non-equilibrium. This is an important consideration as a population inversion is a non-equilibrium state. What follows is a brief discussion of various ways to model and assess the plasma state and a description of a preliminary analysis of a measured spectrum.

The state of a plasma in complete thermodynamic equilibrium (CTE) can be described analytically. The principle assumptions for a rigorous definition of a CTE plasma are:

i)   Electron and heavy particle velocity distributions are Maxwellian.

$$f_{e,i}(\underline{v}_{e,i}) = (m_{e,i}/2\Pi k T_{e,i})^{3/2} \exp\text{-}(m_{e,i} v_{e,i}{}^2/2kT_{e,i}) \tag{1.9}$$

ii) Equipartition of translational energy exsists between electrons and heavy components.

$$T_e = T_i = T \tag{1.10}$$

iii) The occupation of bound electronic states are described by the Boltzmann equation (excitation equilibrium).

$$N_j = N\, g_j \exp(\text{-}E_j/kT)/P(T) \tag{1.11}$$

$$P(T) = \sum_j g_j \exp(\text{-}E_j/kT) \tag{1.12}$$

$$N_j/N_i = (g_j/g_i)\, \exp[\text{-}(E_j - E_i)/kT] \tag{1.13}$$

$$I_{ij} = CN_j A_{ji}/\lambda_{ij} \tag{1.14}$$

where N_j and N_i are the population densities for the ion of interest of the upper and lower state respectively, N is the total density, E_j and E_i the energies of the upper and lower state and P is the state sum or partition function. Equation 1.14 is only valid for an optically thin medium and is not strictly applicable for CTE plasmas. In that equation, I_{ij} is the optical intensity, λ_{ij} the transition wavelength, A_{ji} the transition probability and C is a constant which depends on geometry.

iv) The concentration of densities of electrons, neutral, and ionized species are described by the Saha equation (ionization equilibrium).

$$N_e N_{z+1}/N_z = 2(2\Pi m_e kT/h^2)^{3/2}[P_{z+1}(T)/P_z(T)]exp-[\chi_z/kT] \tag{1.15}$$

$$N_e N_{z+1,k}/N_{z,j} = 6 \times 10^{21}(kT)^{3/2}[g_{z+1,k}/g_{z,j}]exp-[(\chi_z + E_k - E_j)/kT] \tag{1.16}$$

where N_{z+1} and N_z are the number densities for charge states z +1 and z respectively regardless of energy level, and χ_z is the ionization potential for charge state z. In the second version, the Boltzmann equation (Eq. 1.11) has been used to specify particular excited state densities $N_{z+1,k}$ and $N_{z,j}$. E_k is the upper state energy for the kth level in the z+1 ion, while E_j is the upper state energy for the jth level of the z ion.

v) The radiation field is described by a Planck distribution.

Because of energy loss due to nonabsorption of radiation, real plasmas are almost never in CTE. In this case a condition known as local thermodynamic equilibrium (LTE) may exist and conditions (i) - (iv) can be satisfied pointwise rather then with a global, uniform temperature.

Condition (v) no longer applies. In general, for LTE to exsist, collisional processes must be more important than radiative ones, so that the shortfall of radiative energy does not matter. Ionization and excitation must take place primarily through collisions. This is equivalent to requiring a high enough electron density. A more quantitative requirement for LTE is that[1.2]

$$N_e \geq 1.1 \times 10^{14} T_e^{1/2} (E_j - E_i)^3 \quad (cm^{-3}) \tag{1.17}$$

where $\Delta E = E_j - E_i$ is the transition energy from state j to state i of the same ion species and T_e and ΔE are in ev. This equation can be rearranged to find the principle quantum level i for which the above condition is satisfied.

$$E_i \geq E_j - 2.08 \times 10^{-5} N_e^{1/3} / T_e^{1/6} \quad (ev) \tag{1.18}$$

Levels at and above i are in LTE, while those below are in a nonequilibrium state for which other models must be used. This is known as a condition of partial local thermodynamic equilibrium (PLTE). Figure 1.9[1.3] presents the density limits above which the ground states of the various carbon ions will be in LTE. The conditions 1.17 and 1.18 are the hardest to satisfy for transitions involving the ground state.

These four remaining conditions can be used to define LTE with the useful notion of a multitemperature description.[1.4,1.5] The temperatures associated with requirement (i) and (ii) are the species kinetic temperatures. In a 3-species carbon plasma, for example, one notation for the kinetic temperatures would be T_e, T_C, T_{CII}. The conventional, relevant plasma temperature is of course the electron kinetic temperature T_e. The temperatures associated with requirement (iii) are defined as the excitation temperatures, in this example T^{ex}_{CI}, T^{ex}_{CII}. They are obtained from the Boltzmann equation and the bound electronic state distribution. The relevant temperature for requirement (iv) is defined as the ionization temperature T^I_e and is obtained from the Saha equation and the current plasma species concentrations. For the above example of a three component plasma (electrons, neutral carbon-CI and singly ionized carbon-CII), there are thus 6 relevant temperatures. For a plasma in *kinetic equilibrium* the

23

requirements (i) and (ii) of a Maxwellian particle distribution and equipartition of translational energy imply $T_C = T_{CI} = T_e$. A plasma is defined to be in *ionization equilibrium* if $T^I_e = T_e$. *Excitation equilibrium* is defined by the requirement that $T^{ex}_{CI} = T^{ex}_{CII} = T_e$. Thus, in this example, LTE exists when $T_e = T_C = T_{CII} = T^I_e = T^{ex}_{CI} = T^{ex}_{CII} = T$, i.e. there is only one relevant local thermodynamic temperature. Each of these particular types of equilibrium is promoted by increasing electron density. Ionization equilibrium however is destroyed by recombination. Both ionization and excitation equilibrium also depend on the various characteristic rates of the plasma which are a function of pumping power, plasma hydrodynamic time scales determined by expansion and material supply rate, recombination time scales, and atomic relaxation time scales. Further work is required to identify the specific conditions required for each type of equilibrium, and to evaluate these characteristic rates for our plasma.

In the absence of LTE it is still possible to calculate atomic level populations, but only if the relevant collision cross sections and transition probabilities are known. This requires a great deal of atomic data which may only be be known accurately for H-like and He-like systems. The next most common approximation in this category is the coronal equilibrium (CE) model, which is appropriate for high temperature, low density plasmas. For some plasmas, a combination of LTE and CE may be appropriate. Figure 1.10[1.3] presents the density limits below which the lower states of the various carbon ions are in CE.

The collisional-radiative equilibrium (CRE) model is a steady state solution to the atomic level rate equations, requiring even more atomic data. We have a 56 level, steady-state CRE code to calculate the ionization dynamics of a carbon plasma. This code gives ion fractional abundances versus temperature with the total ion density as a parameter. See section 3.0 of this report for a discussion of this code, its applications to modeling our experimental results, and other theoretical work.

ii) Modeling

A population inversion can only exist in non-equilibrium plasmas, thus the importance of assessing the plasma state. For example, population inversions can occur in a *supercooled* plasma, partially defined by the
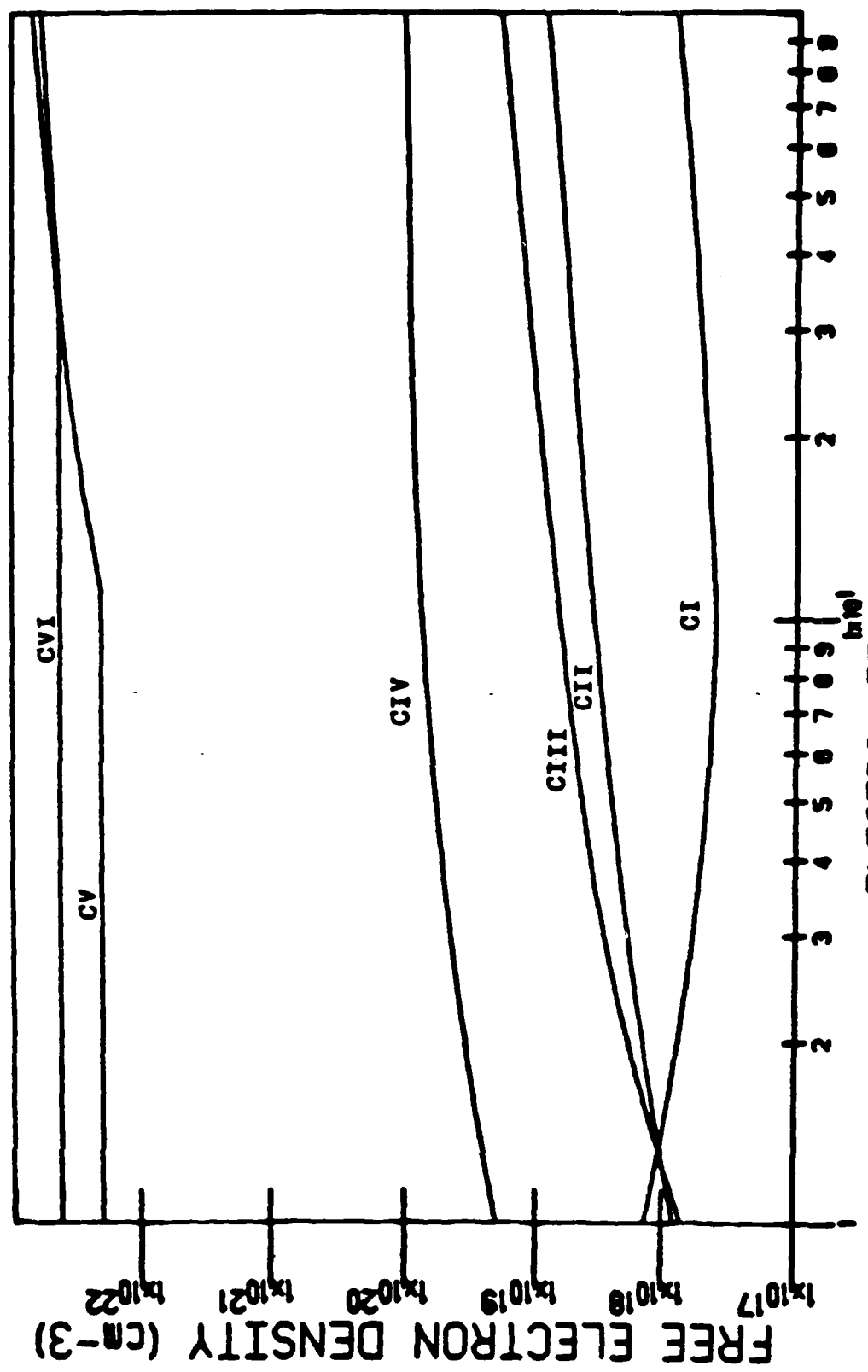
24

ELECTRON TEMPERATURE (ev)

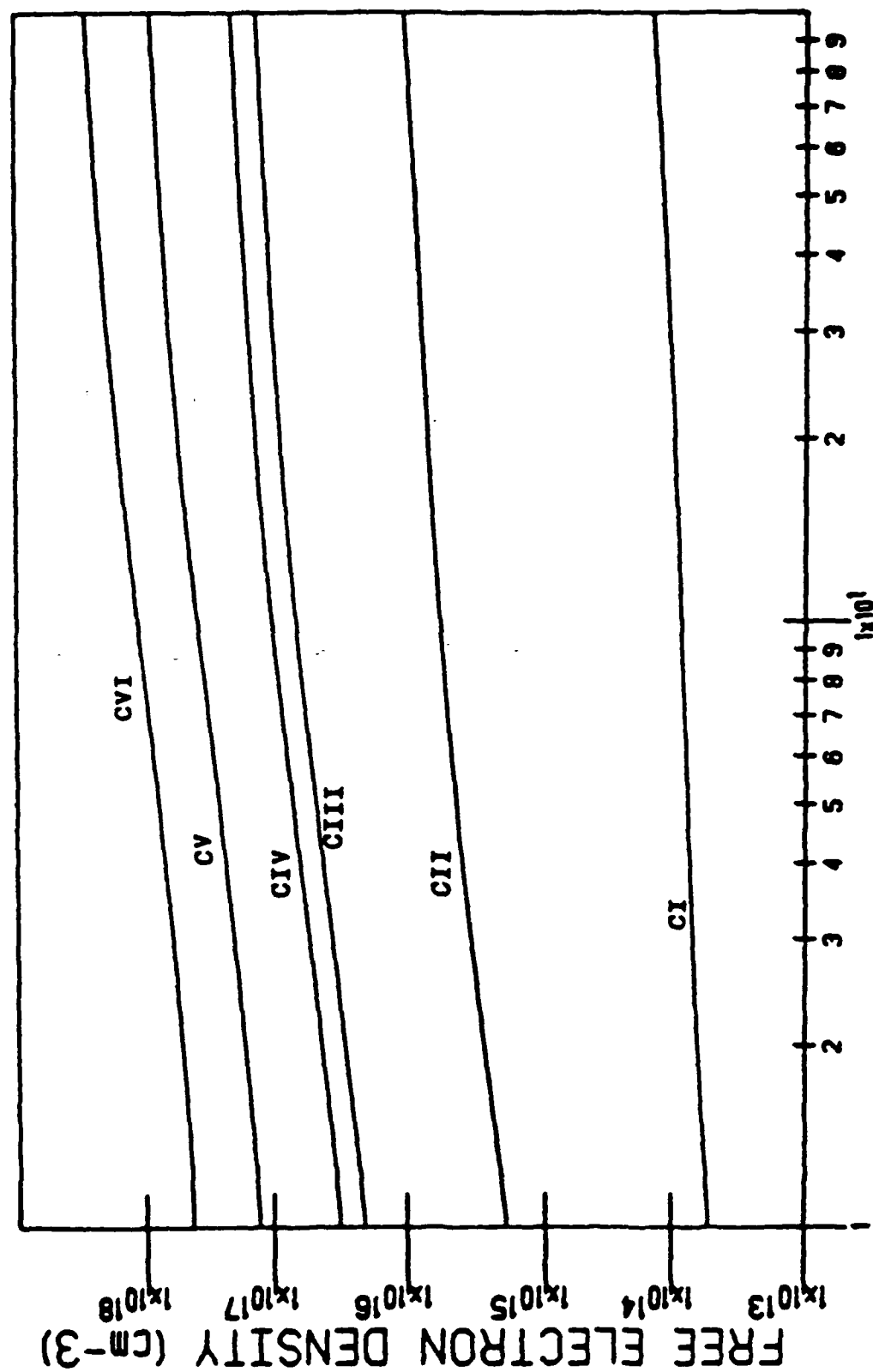Figure 1.9 : REGIONS OF VALIDITY FOR LTE MODEL

Figure 1.10 • CORONAL LIMITS FOR THE ION STAGES OF CARBON

property that $T^I_e > T_e$. In this plasma type of plasma the degree of ionization is much higher than that implied by the electron kinetic temperature. Inversions can occur either in a transient ionization build-up phase or in a recombination phase. Both have been demonstrated with electron beam pumping but in the latter case it is possible that a steady state supercooled plasma can be achieved. Other promising non-equilibrium situations have been demonstrated in the distribution of bound electronic states.[1.6]

We have performed very preliminary initial analysis of the measured spectra. Electronic temperatures have been obtained from Boltzmann plots for some of the spectra. These are based on a rearrangement of the Boltzmann equation for bound electronic state densities of a common ionization state. Substituting Equation 1.14 into Equation 1.11, lumping the constants, and taking the logarithim of both sides one finds:

$$\ln(I_{ji}\lambda_{ij}/A_{ji}g_j) = \text{constant} - E_j/kT \tag{1.19}$$

A plot of $\ln(I\lambda/Ag)$ versus upper state energy E_j will yield a straight line if those excited state populations follow the Boltzmann equation. An important possible source of error in this analysis is the assumption of optically thin lines. Other errors arise due to uncertainties in A, often quite large. In order to obtain meaningful Boltzmann plots the measured spectra must satisfy the following conditions:

i) The line is strictly or primarily identified with one atomic species and one particular transition or multiplet. If other components or transitions are coincident or close (within instrumental resolution) , they may have to be excluded from the calculation.

ii) The signal to continuum ratio must be adequate for each peak.

iii) The transition probability must be available for each line. One line can often be associated with a particular g-degenerate multiplet, which cannot be separated because of instrumental resolution.

iv) Electronic temperature estimates from line ratios require at least 2 peaks satisfying requirements (i) - (iii) with

different ΔE_{upper} (preferably a large difference to reduce error). Many such peaks are needed to get an adequate Boltzmann plot.

If 3 or more peaks satisfying these requirements are available, the negative inverse of the slope of the linear best fit line gives the excitation temperature for that species. Electronic equilibrium for that species exists if the correlation coefficient of that line is high (> 0.9). Because of the resolution limits of the current 0.275 meter spectrograph only a few of the spectra obtained satisfy these requirements. We expect this limitation will be removed when our new 1.0 meter spectrograph becomes available in the next couple of months.

If the plasma components all have similar excitation temperatures, this *suggests* that this temperature may also be the electron temperature. For example in shot M835 the Boltzmann analysis yields T^{ex}_{CII}= 2.4 ± 0.3 ev (Figure 1.11), and T^{ex}_{CIII}= 2.7 ± 0.2 ev (Figure 1.12). Since these are identical within experimental error, our initial method of spectral analysis assumed that the electron temperature is ≅ 2.5 ev *and* that the plasma is in LTE. The use of the Saha equation is then valid. With the approximate charge state distribution in spectra M835, we find the electron density ≅ $10^{18}cm^{-3}$. This density is consistent with LTE but care must also be taken to assure that the argument does not become circular.

The assumption, made in the above analysis, that $T_e = T^I_e = T^{ex}_{CII}=T^{ex}_{CIII}$ is strictly unjustified. Another approximate method we have used to estimate the plasma state uses the CRE code and compares experimental and predicted relative ion abundances. The method involves finding an electron temperature required to give a charge state abundance consistent with experiment for a particular density. This procedure is also not strictly correct as the presence of particular lines in a spectrum does not directly translate to ion abundances. However the technique can yield some useful qualitative information about the plasma state and plasma properties.

The spectra for shot M835 and M836 (taken at similar times in the pulse evolution) indicate that CIII and CII are the principle constituents, with enough CIV to also contribute to line emission. CIII is probably more abundant than CII as the CIII lines detected have high upper state energies

BOLTZMANN PLOT - EARLY STAGE III

M835

CII

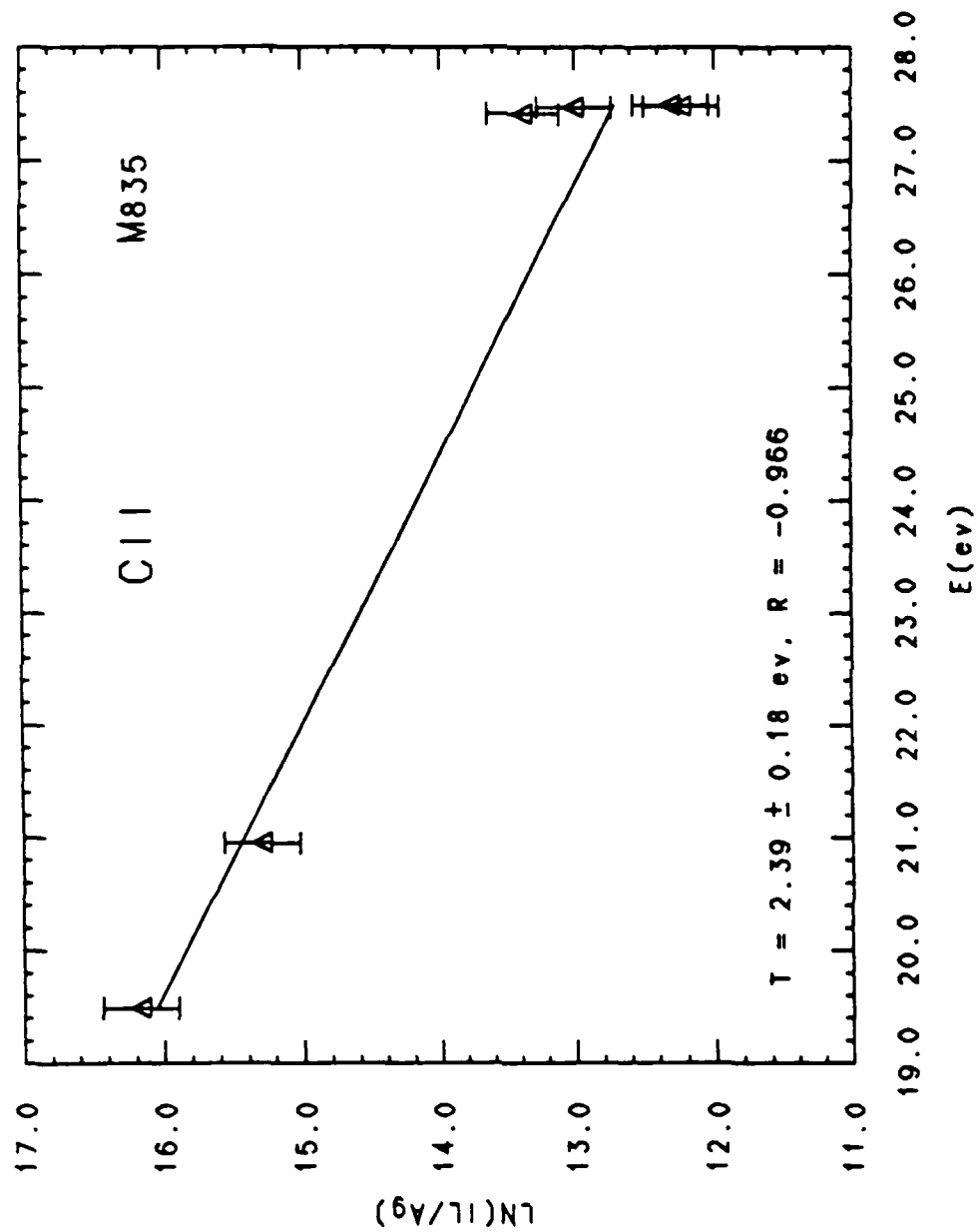T = 2.39 ± 0.18 ev, R = -0.966

E(ev)

LN(IJ/Ag)

Figure 1.11

(30-40 ev), which would only be expected in a hotter, more highly ionized plasma. Thus we are looking for a density and temperature consistent with abundances decreasing in this order: CIII, CII, CIV. We expect negligible CI and CV to be present. Crossover temperatures, T_c, can be defined at the points where various ion abundances are equal (see Figure1.13).[1.3] There are two crossover temperatures describing the region where a particular ion species dominates. For example, for $T > T_{CII:CIII}$ of the crossover CII to CIII, the ion abundance of CIII is greater than that of CII. Likewise for for $T < T_{CIII:CIV}$ of the crossover of CIII to CIV, the CIII abundance is greater than the CIV abundance. Hence, in the temperature range $T_{CII:CIII} < T < T_{CIII:CIV}$, CIII is the dominant plasma constituent. Finally for $T < T_{CII:CIV}$ for the crossover of CII to CIV, the ion abundance of CII is greater than that for CIV. These three temperatures are ordered $T_{CII:CIII} < T_{CII:CIV} < T_{CIII:CIV}$. The temperature range required in order to be consistent with experiment is $T_{CII:CIII} < T < T_{CII:CIV}$. Table 1.1 contains these crossover temperatures, obtained from Figures 1.13 to 1.16[1.3], for four different densities.

Table 1.1 shows that the allowed range for the actual electron temperature (provided by the first two columns) is larger than the excitation temperatures (2-3 ev) for these four densities. Considering the experimental error, the case for $N_e = 10^{17}$ cm^{-3} is close to agreement. An upper bound on the temperature is provided by the third column, the temperature at which CIV becomes more abundant than CIII. These arguments provide some evidence that equilibrium assumptions may not apply to this plasma, and the actual electron temperature may be somewhat higher than the excitation temperature.

Table 1.1

|	$T_{crossover}$(ev)		
N_e(cm^{-3})	CII:CIII	CII:CIV	CIII:CIV
10^{12}	4	7	10
10^{15}	3	5	8
10^{17}	3	4	5
10^{19}	4	5	6

A better way to utilize the CRE code is to first obtain an independent

experimental determination of electron density, perhaps through line broadening. This density combined with a relative or absolute measurement of line intensities, can be compared with the CRE prediction for those particular lines, to determine the temperature. Several different lines or pairs of lines can be used to cross check the results. In addition an independent measurement of T_e would be desirable. At present our instrumental broadening dominates the peak widths for the carbon species. An estimate using the H_β line (hydrogen being the principle impurity), may be possible if it can be separated from close carbon lines. Stark broadening is expected to be very large for hydrogen (and hydrogen-like) species. These possibilities are expected to become accesible when our new 1.0 meter spectrograph becomes available.
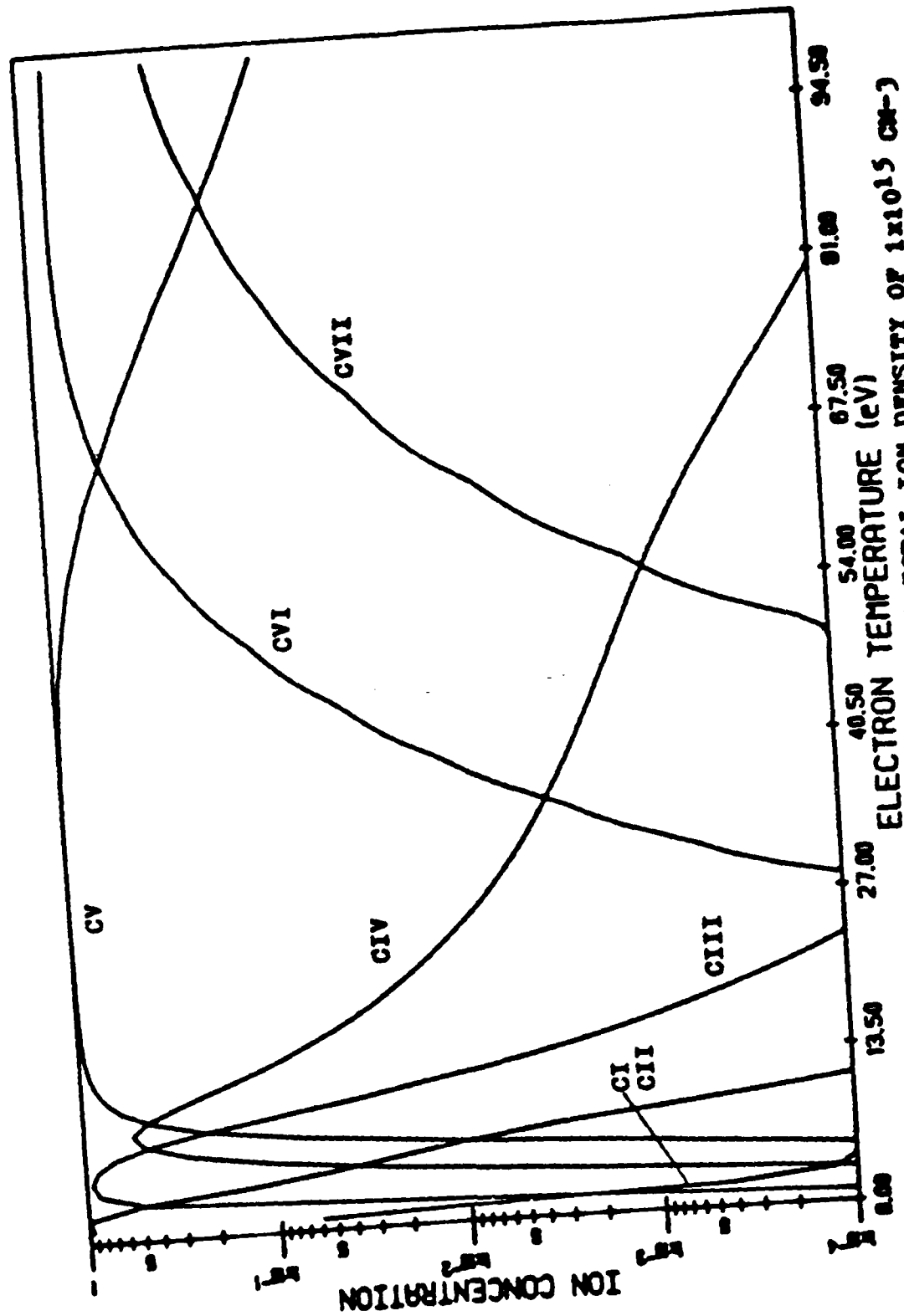
CRE MODEL, ION ABUNDANCE CURVES FOR A TOTAL ION DENSITY OF 1×10^{15} CM^{-3}

Figure 1.14
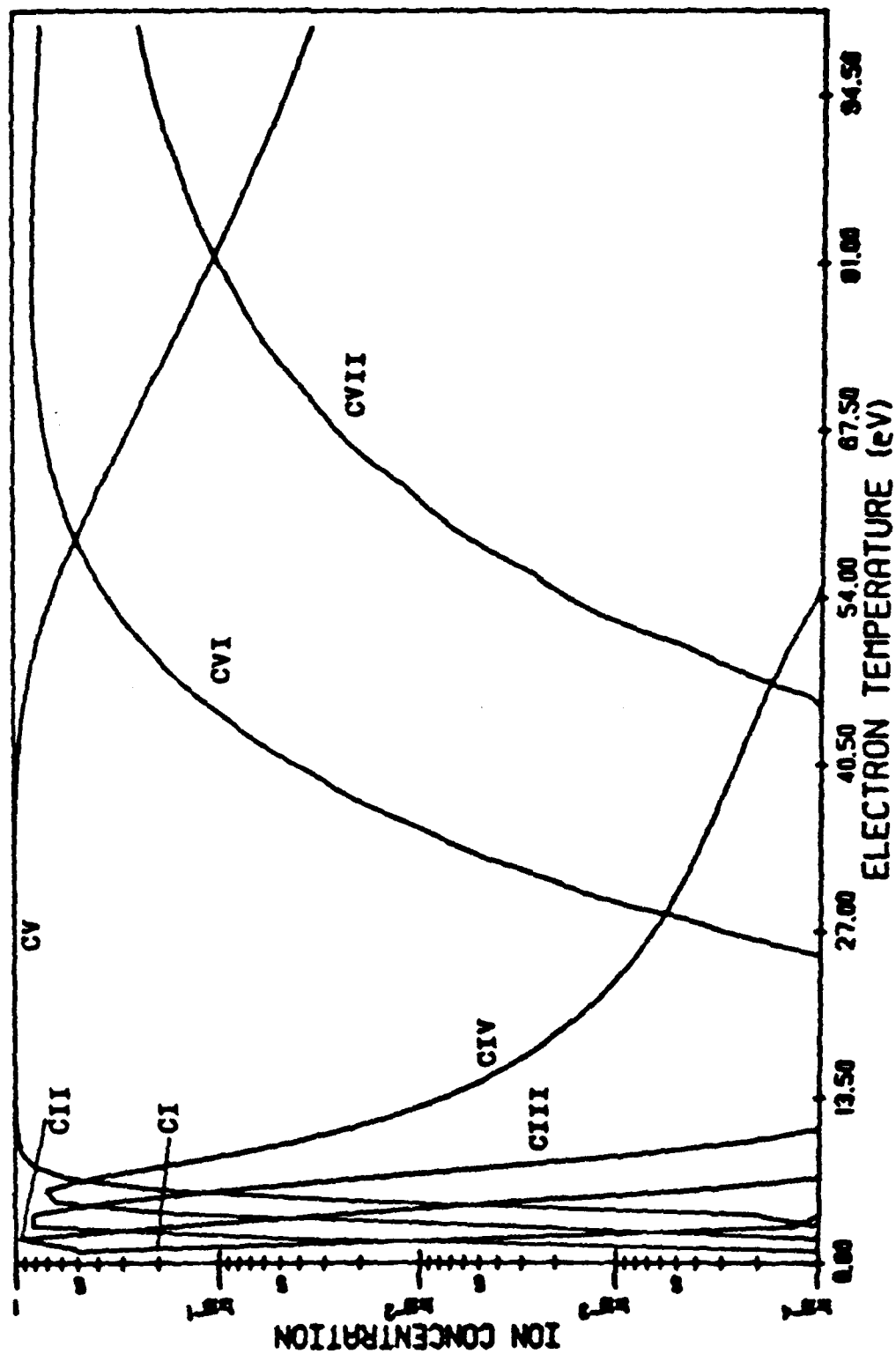
CRE MODEL, ION ABUNDANCE CURVES FOR A TOTAL ION DENSITY OF 1x10^{17} CM^{-3})

Figure 1.15

CRE MODEL: ION ABUNDANCE CURVES FOR A TOTAL ION DENSITY OF 1×10^{19} CM-)
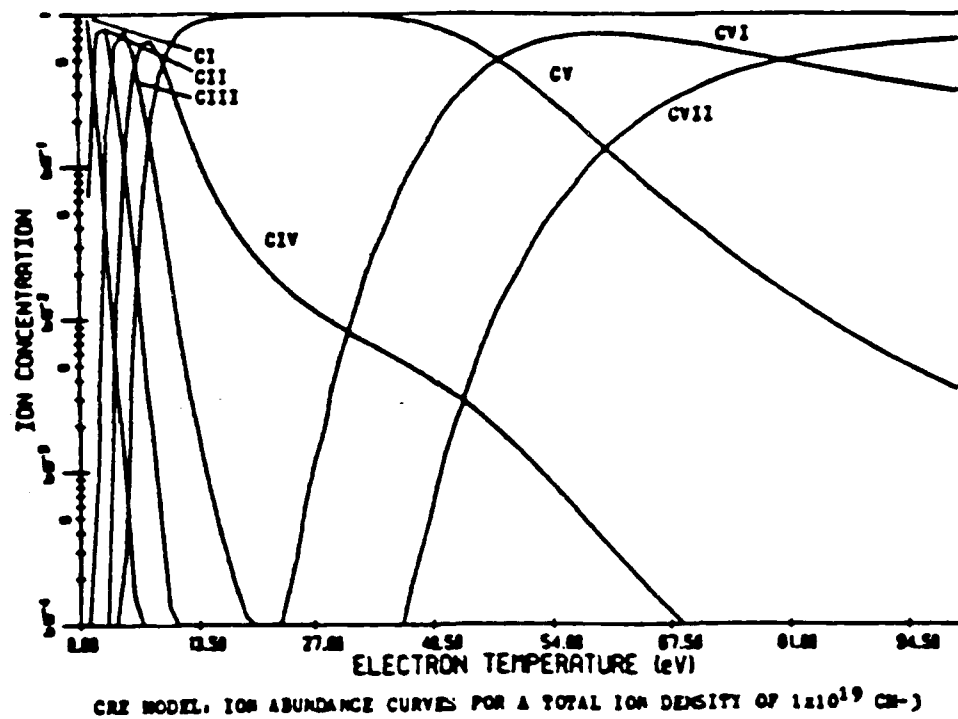
Figure 1.16

1.3) Discussion of Spectroscopic Results

This section of the report contains complete diode analysis and spectra for a selection of crowbarred and noncrowbarred shots. The diode analysis consist- of four plots: voltage, current with current model, closure analysis, and dose, just as in Figure 1.7. Recall section 1.2.a.iv and the discussion on idealized data. The OMA gate information is displayed on the voltage, closure and dose plots. The time scale for the OMA is referenced with t = 0.0 at the initial rise of the voltage. Presented on the closure plots are the closure velocity and the predicted diode shorting time. The spectra are labeled with the measured wavelengths, peak identification, stage identification, and excitation temperatures when available. All spectra are presented on the same relative intensity scale.

a) Crowbarred Shots

The first two shots M713 and M718, Figures 1.17 and 1.18, are examples of stage I crowbarred shots where no light is detected. For both shots the dose during the gate is below 200 J/gr. This is well below the expected lower limit for anode plasma formation, about 350 J/gr.

In shot M717 the light detected was primarily singly ionized carbon C II, with some molecular emission from C_2. Note the low level of background emission. The spectrum is shown in Figure 1.19a. T_{ex}, the excitation temperature is about 2.2 ev. The OMA was gated from 52 to 631 ns, nominally 600 ns wide. The diode analysis, in Figure 1.19b, shows that the dose has increased to > 370 J/gr before the end of the OMA gate so there is evidence consistent with the presence of an anode plasma. The closure analysis implies a shorting time of 720 ns, which is after the end of the gate at 631 ns. One might therefore conclude that this is an example of a stage II crowbar. The closure velocity analysis, however shows that there may be a change in the velocity as if anode plasma closure was coming into play. The current model with bipolar effects does not matc⁴ experiment well when this apparent change in velocity occurs. There are several possibilities. The first is that the change is only an artifact of experimental error although there still is an anode plasma. There may not
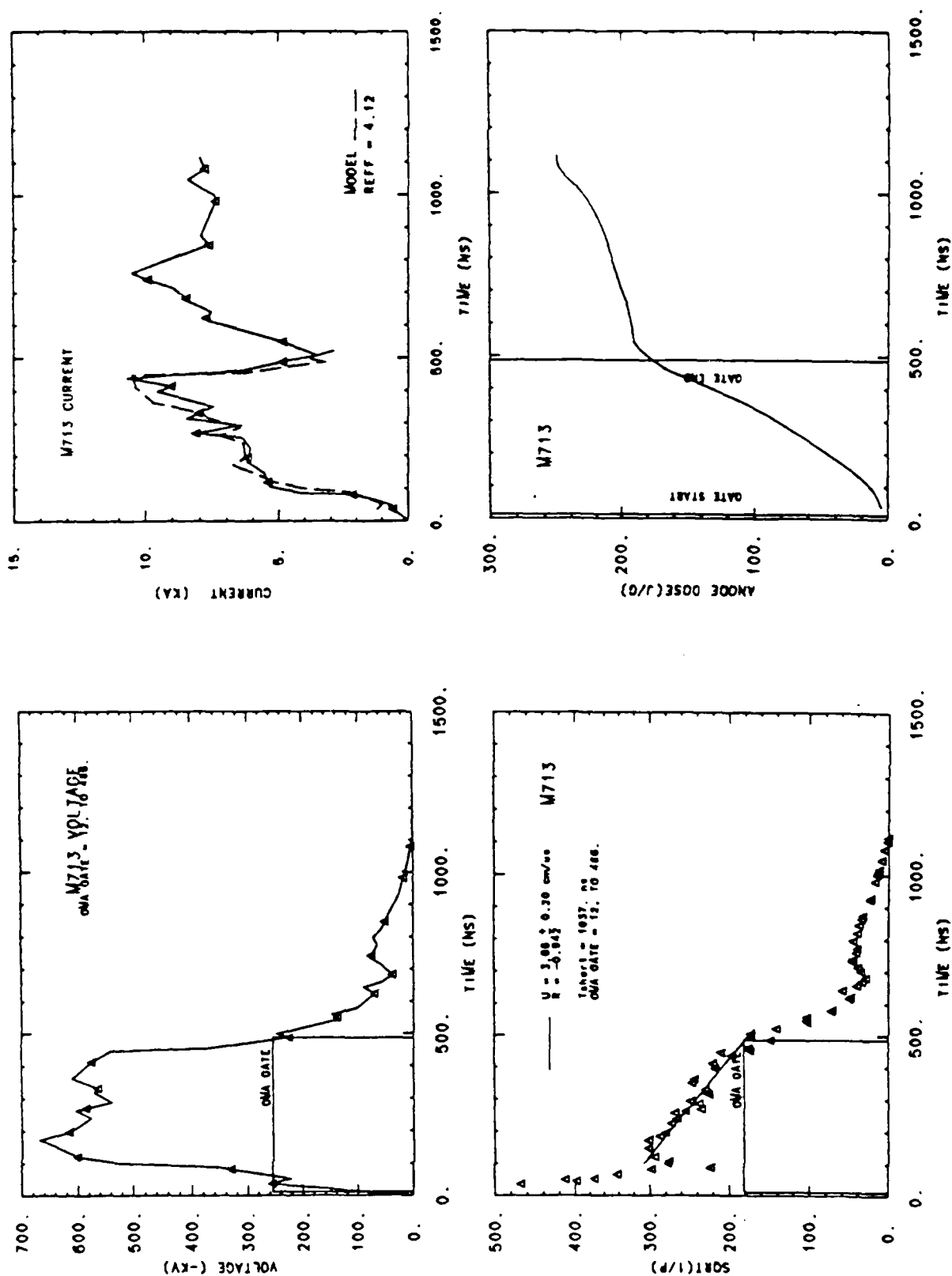
CROWBAR - STAGE I EXAMPLE
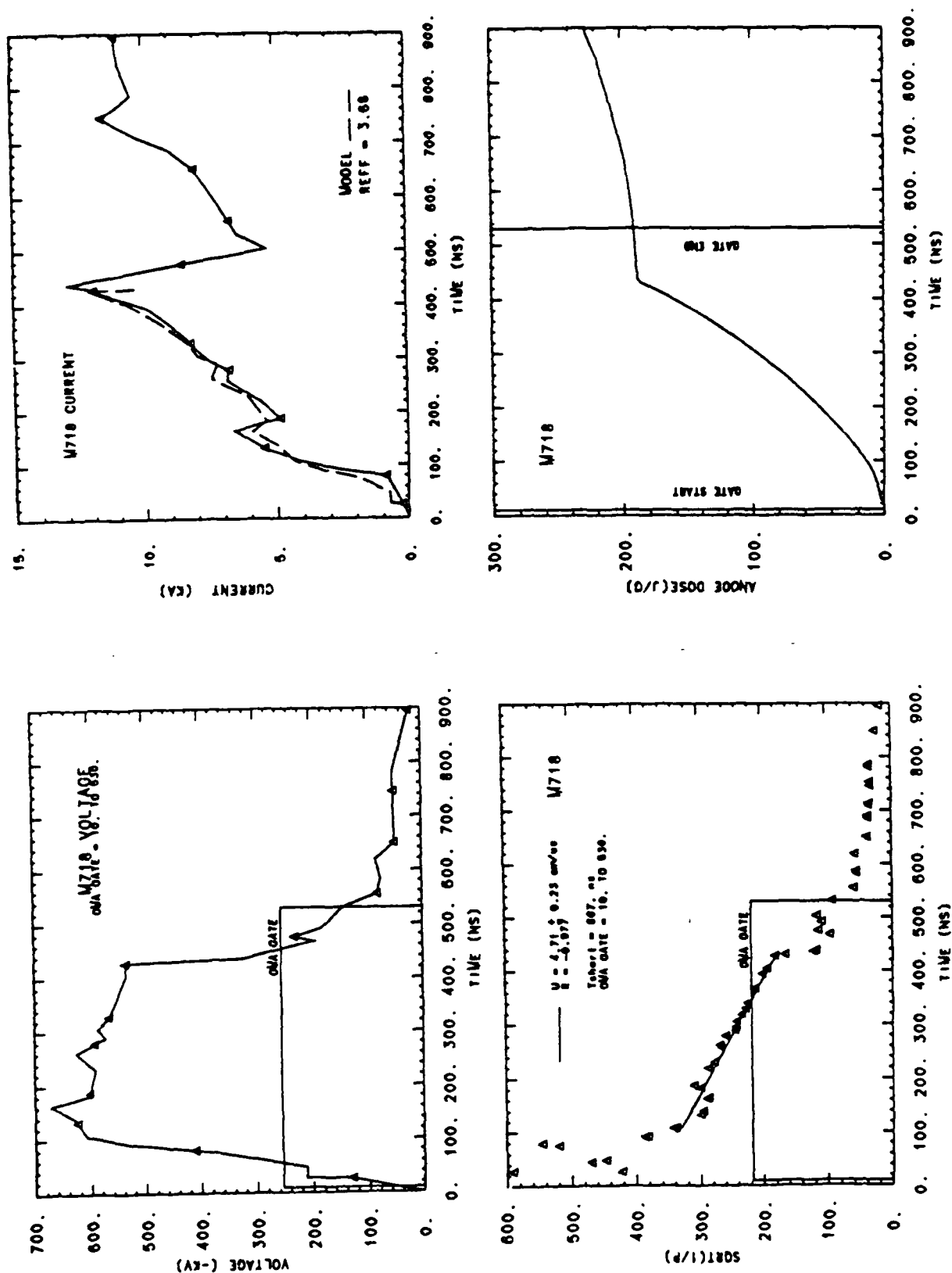

Figure 1.17

CROWBAR - STAGE I EXAMPLE

Figure 1.18

CROWBAR

M717

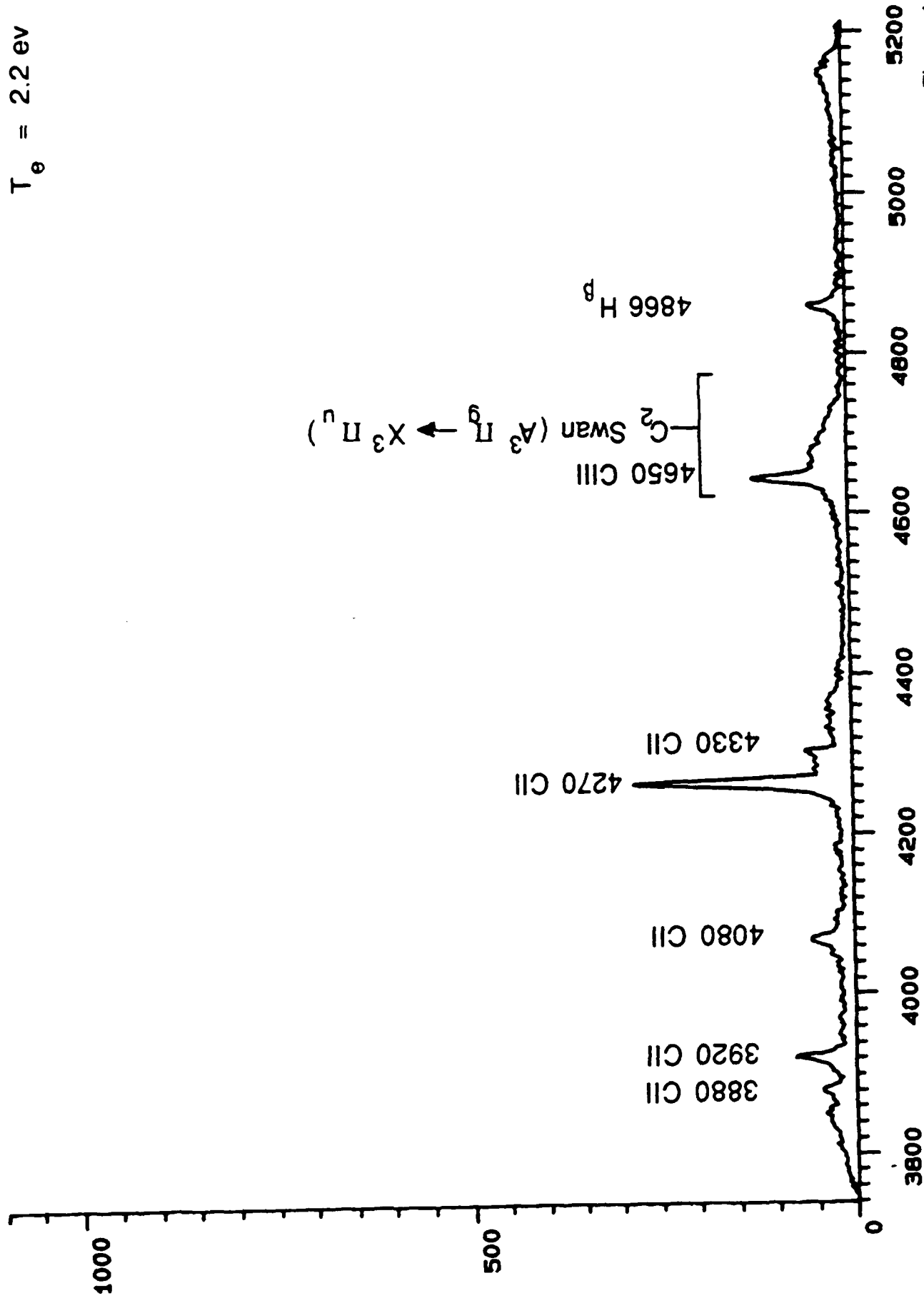Stage: II, Early III ?

T_e = 2.2 ev

4866 H_β

C_2 Swan ($A^3 \Pi_g \leftarrow X^3 \Pi_u$)

4650 CIII

4330 CII

4270 CII

4080 CII

3920 CII
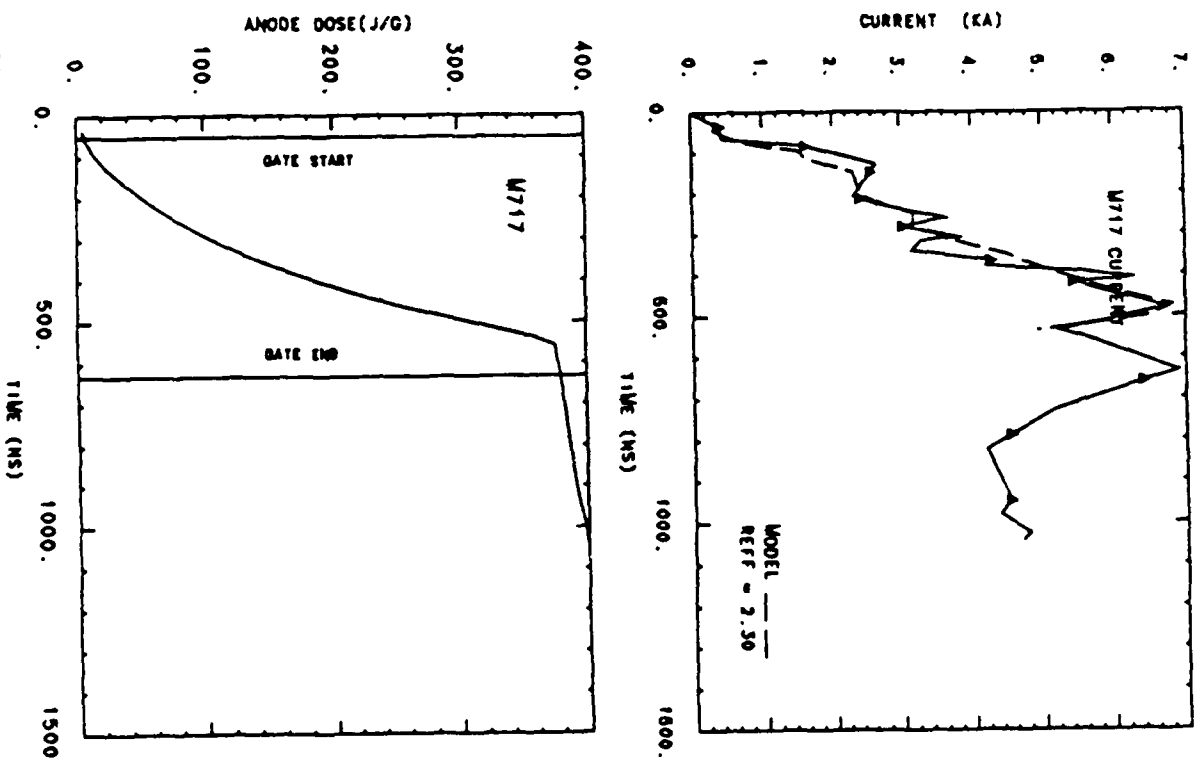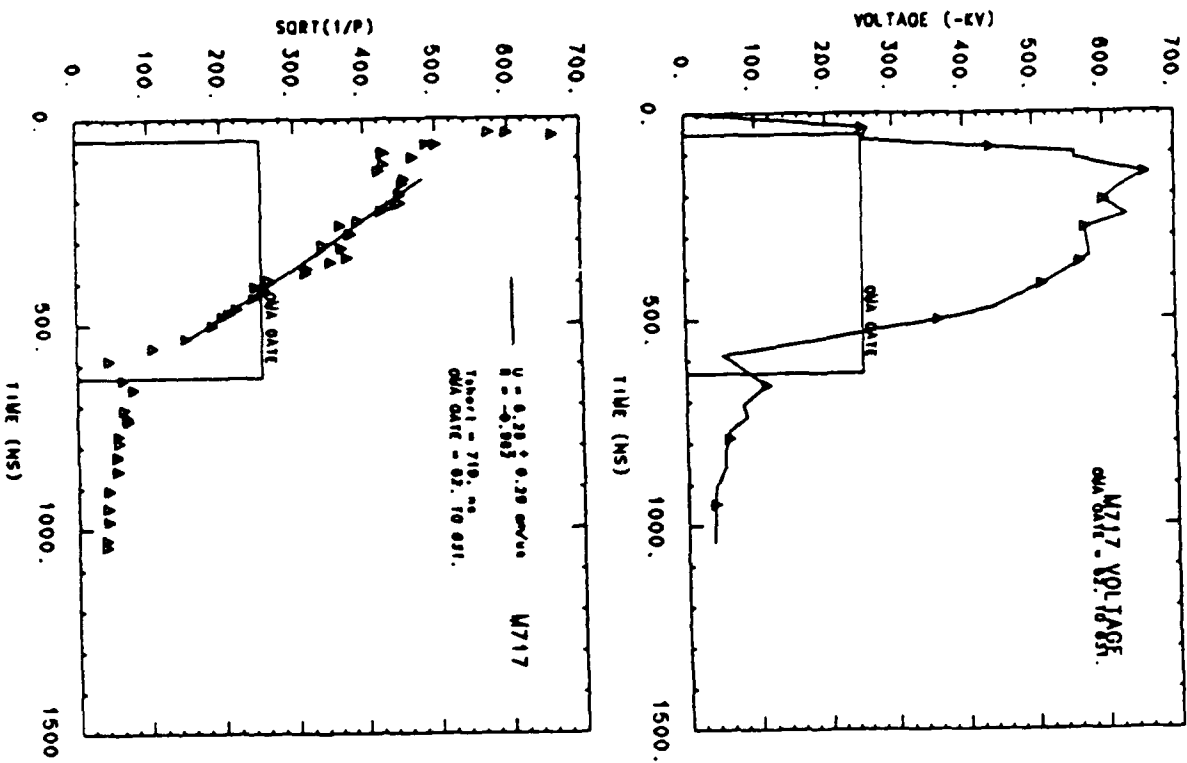
3880 CII

1000

500

0

3800

4000

4200

4400

4600

4800

5000

5200

Figure 1.19a

Figure 1.19b

in fact be an anode plasma. Another possibility is that a simple 0-d static, lumped, uniform plasma model probably cannot effectively simulate the diode-generator and plasma dyanamics with anode effects in 3-d geometry. A more complicated current model would be required. A final possibility is that this is a transition region where arc and space charge effects contribute to the current. If this does indeed represent anode plasma closure then the diode shorts at about 600 ns, less than the end of the OMA gate. Thus, in this case, and because of our uncertainty in the diode dynamics during this period, the light may also be contributed from a short section of early stage III.

Shot M719 spectra and analysis are shown in Figures 1.20a and 1.20b. In this shot the OMA was gated from 461 ns to 978 ns, about 400 ns later than M717 with a nominally 500 ns wide gate. Keep in mind that direct comparisons between shots are not justifed unless the closure velocity and effective diode area are close. Due to the irreproducability of the cathode plasma this is often not the case. The shorting time in this shot is about the same, 710 ns which places it in about the middle of the gate. Possible contributions to the detected light are therefore anode plasma, cathode plasma and arc components.

The dose from space charge limited current incre ases to > 320 J/gr. Recall that this is a conservative estimate of the space charge dose due to use of a simple current density model but also due to uncertainty in assigning a cutoff for the dose integral. This cutoff was chosen so that the current model agreed with experimental current, hence space charge assumptions were justified. After this cutoff, in the transition and arc region, a very conservative dose estimate is used. The actual dose after this cutoff therefore probably increases faster than shown. Thus there may be stage II anode plasma contributions to the emitted light. Note the presence of ionized carbon as would be expected from an anode plasma with incident ionizing electrons. As the shorting time is in the middle of the gate, cathode plasma and arc components would also be visible thus the designation of early stage III. The molecular components are all consistent with cool hydrocarbon cathode contaminants. The increase in maximum detected counts (as well as total integrated counts) is probably due to heating by the high current ($\cong 10$ kA) low voltage arc later in time.

The OMA gate for shot M720 is from 976 ns to 1494 ns, approximately
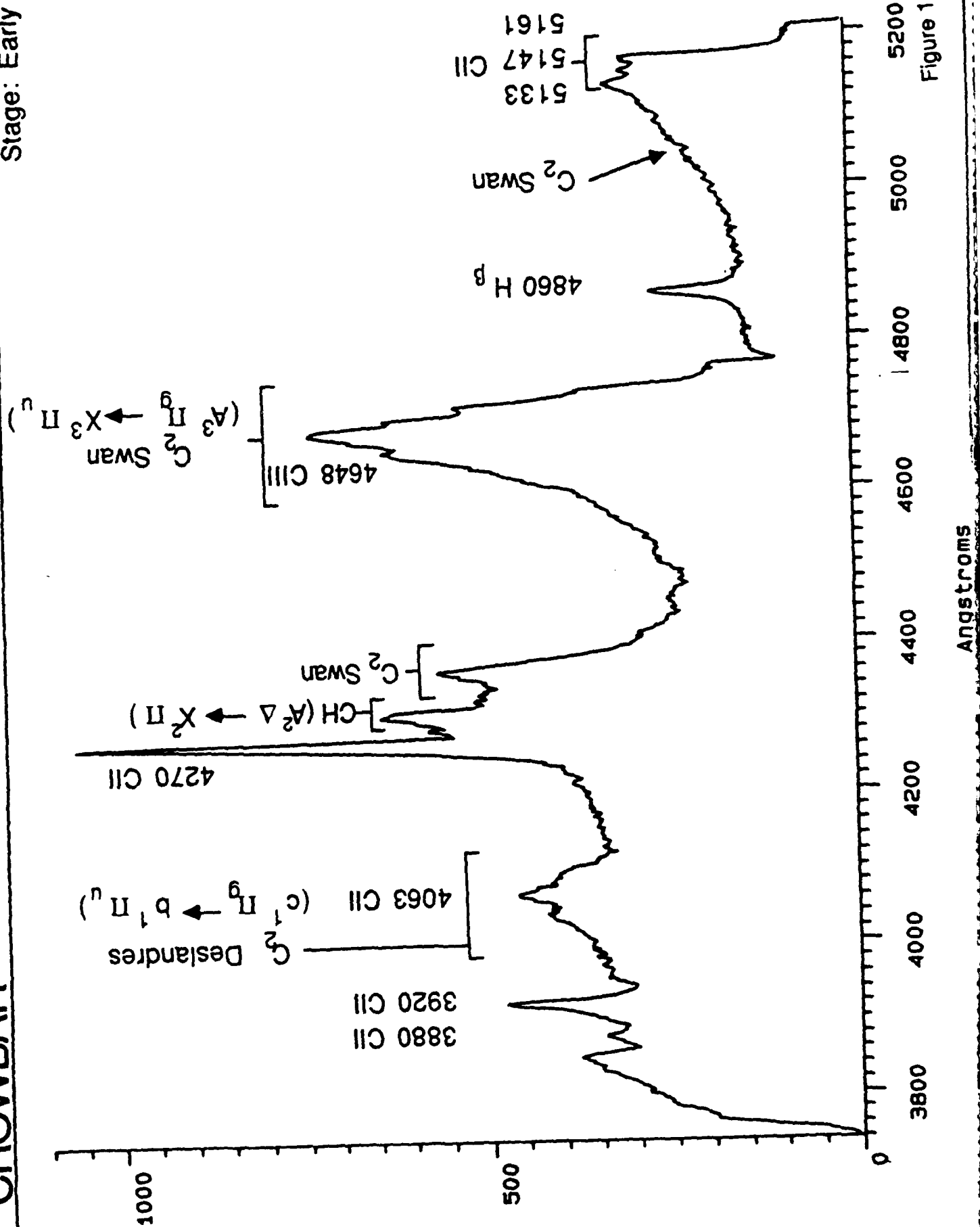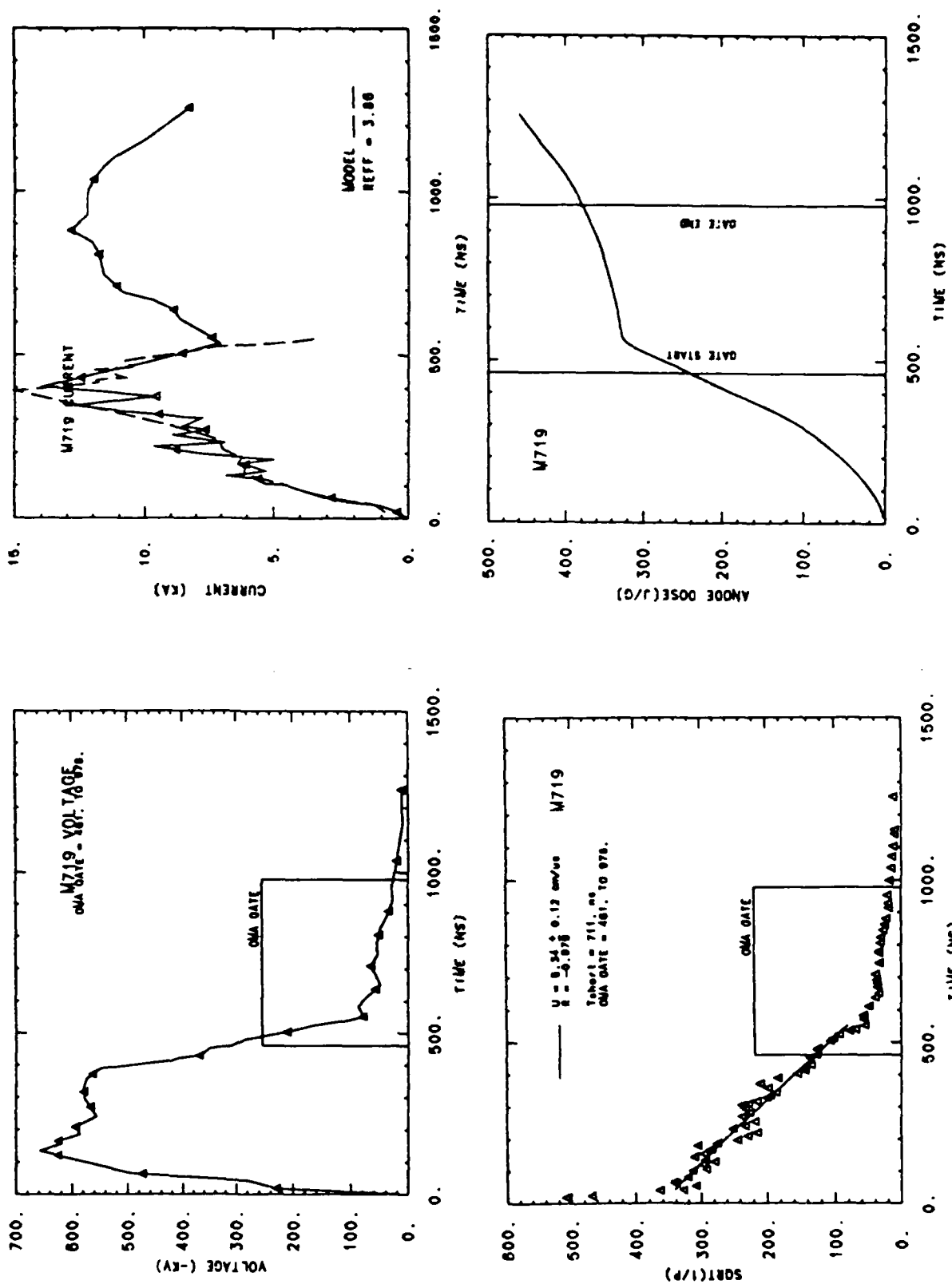
42

CROWBAR

M719

Stage: Early III

3880 CII
3920 CII

4063 CIII $\quad \tilde{C}_2$ Deslandres $\quad (c^1\Pi_g \rightarrow b^1\Pi_u)$

4270 CII

CH $(A^2\Delta \rightarrow X^2\Pi)$

C_2 Swan

4648 CIII $\quad \tilde{C}_2$ Swan $\quad (A^3\Pi_g \rightarrow X^3\Pi_u)$

4860 H$_\beta$

C_2 Swan

5133
5147 CII
5161

Angstroms

Figure 1.20a

Figure 1.20b
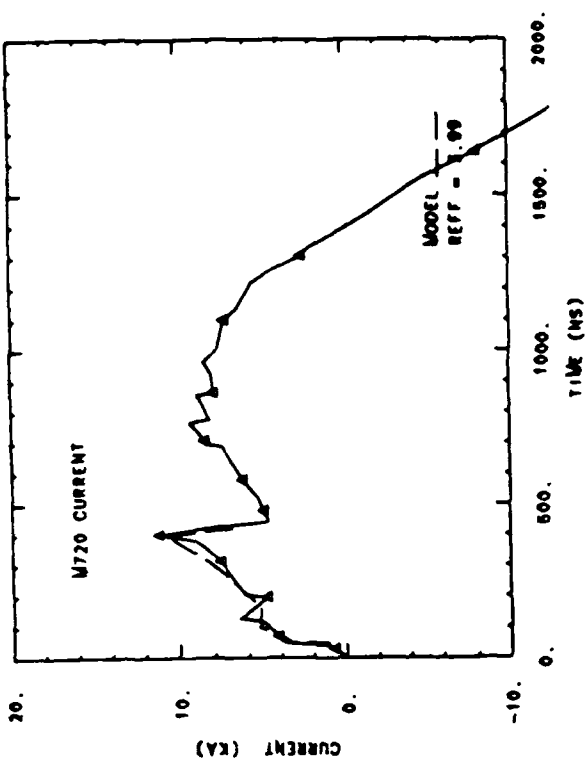
CROWBAR

M720

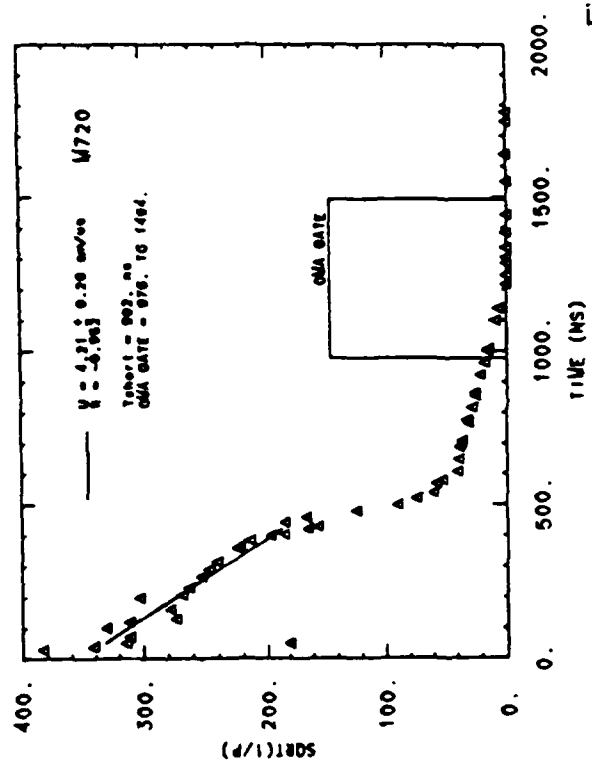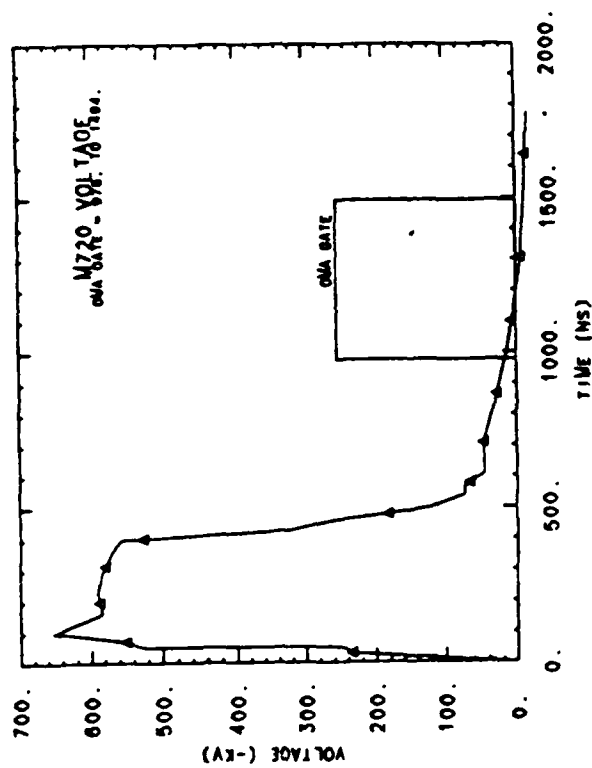Stage: Middle III
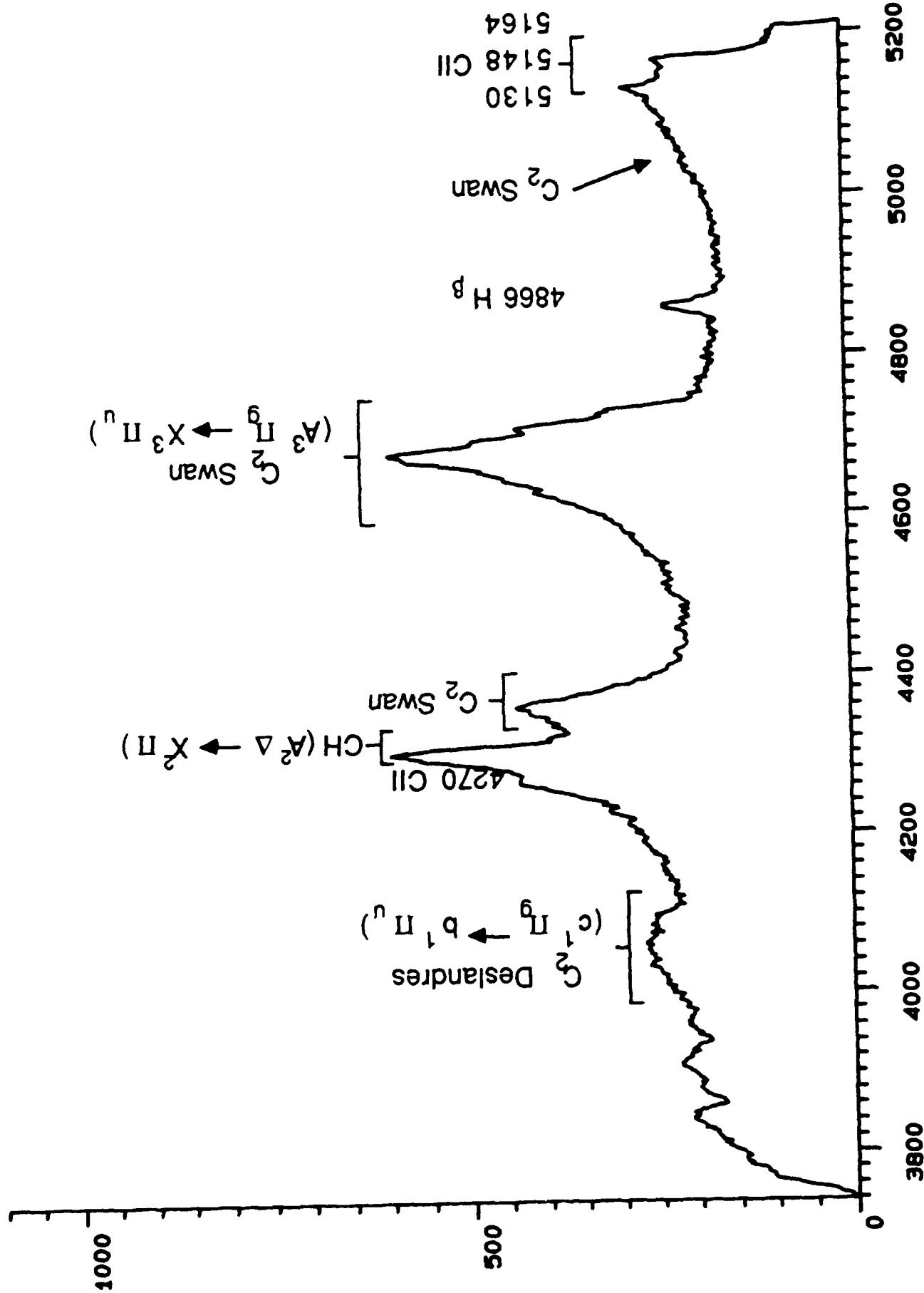
Figure 1.21a
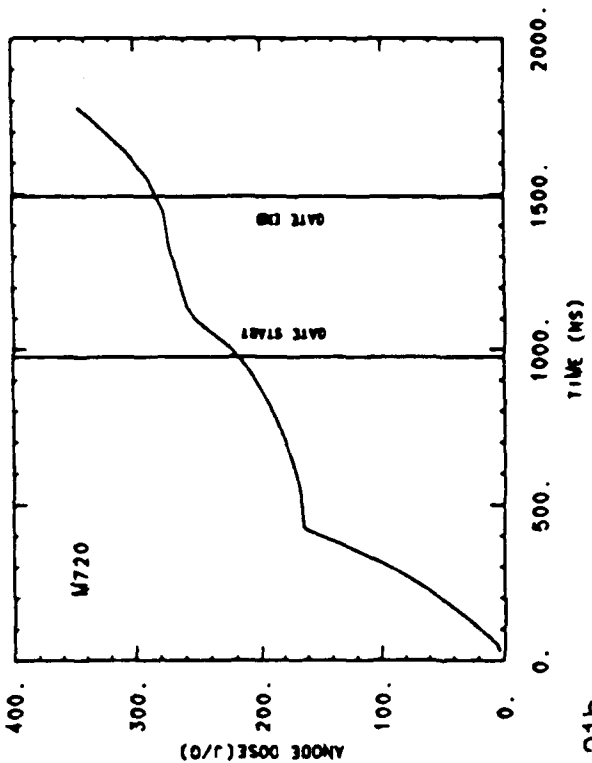
Figure 1.21b

500 ns later in time than M719. The constituents in the spectrum, Figure 1.21a, are identical with that shot, but at slightly reduced intentsities. The signal to noise ratio for the atomic peaks are poor. These two features are consistent with a plasma that is cooling and recombining, which correlates with the falling current. The diode analysis in Figure 1.21b gives a shorting time of 902 ns, hence the gate is after the arc transition region, and hence the classification of middle stage III.

The last three shots have been gated sequentially later in time. Due to the width of the gates, they make up a long time integrated temporal evolution study, and give a good idea of what the plasma components are. The uncertainty in the source of the plasma due to the width of the gates is not critical since we desire a more highly ionized plasma. Another difficulty in deciding what stage a particular shot is in, aside from wide OMA gates, is that the crowbars end just as the dose is getting up into the "interesting regime" where anode plasmas are expected. In noncrowbarred shots, as discussed before, the doses before shorting will be larger.

b) Noncrowbarred Shots

Due to the voltage opening behavior discussed earlier, the interpretation of noncrowbarred shots is not necessarily easier than crowbarred ones. Shot M831 is an example of this. The spectrum, Figure 1.22a shows low intensity atomic emission from CII and CIII. We have tentatively associated the background with Cerenkov emission by high energy electrons slowing down in the acrylic window. This feature is confusing as its appearance on a given experimental run seems to be random, however it does not appear when gates are during the low energy portions of the pulse. The OMA gate from 0 to 950 ns goes beyond the apparent shorting time of 873 ns (see Figure 1.22b). The dose before shorting has reached > 550 J/gr well into the range for anode plasma initiation. The background noted on the spectrum is consistent with the formation of the plasma during stage II. Due to the width of the gate the line emission did not necessarily occur during stage II and there may be early stage III elements in this plasma. The uncertainty in the plasma dynamics because of the voltage opening behavior and the inability to model the current would put uncertainty in the identification of the

47
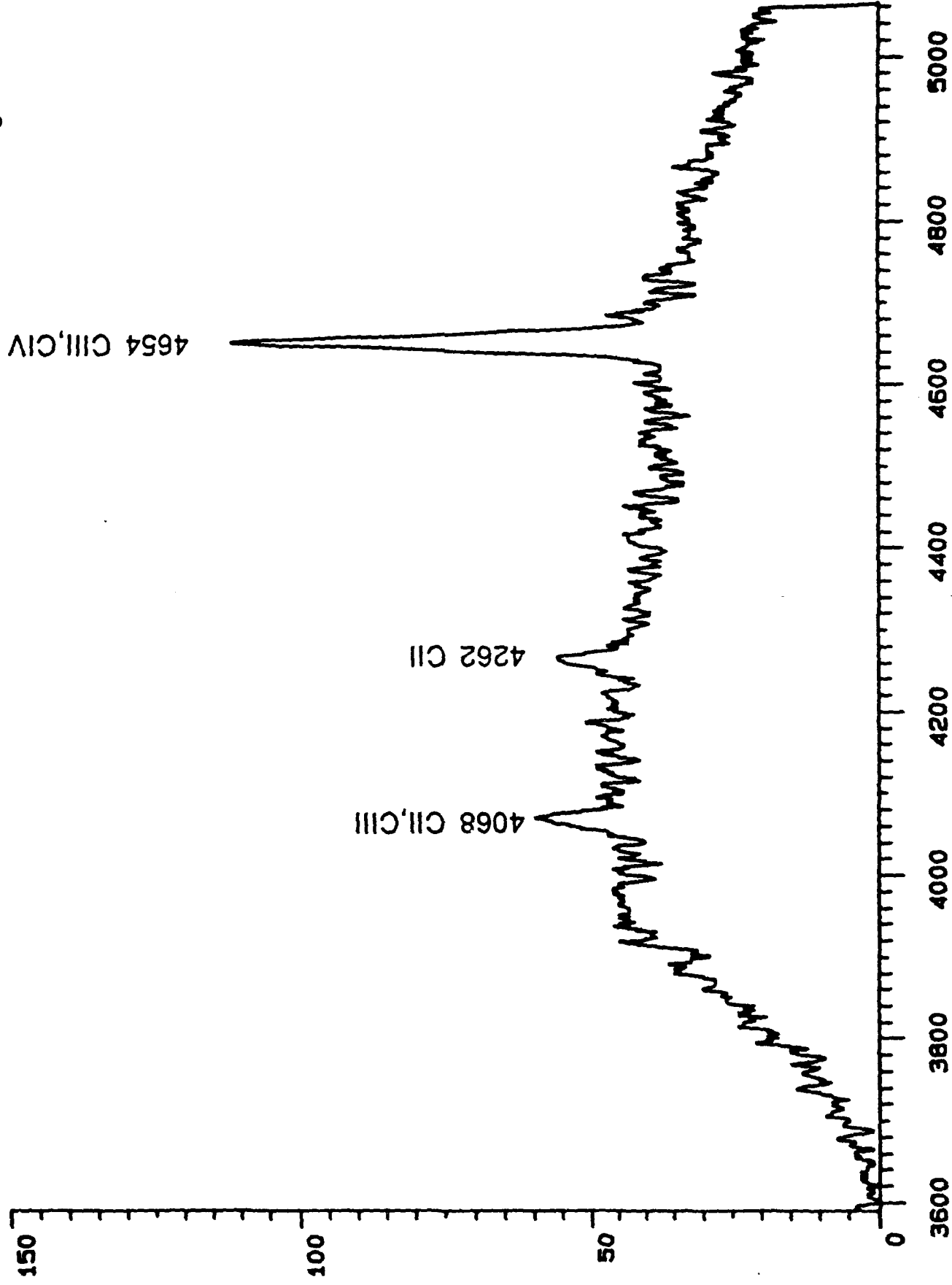
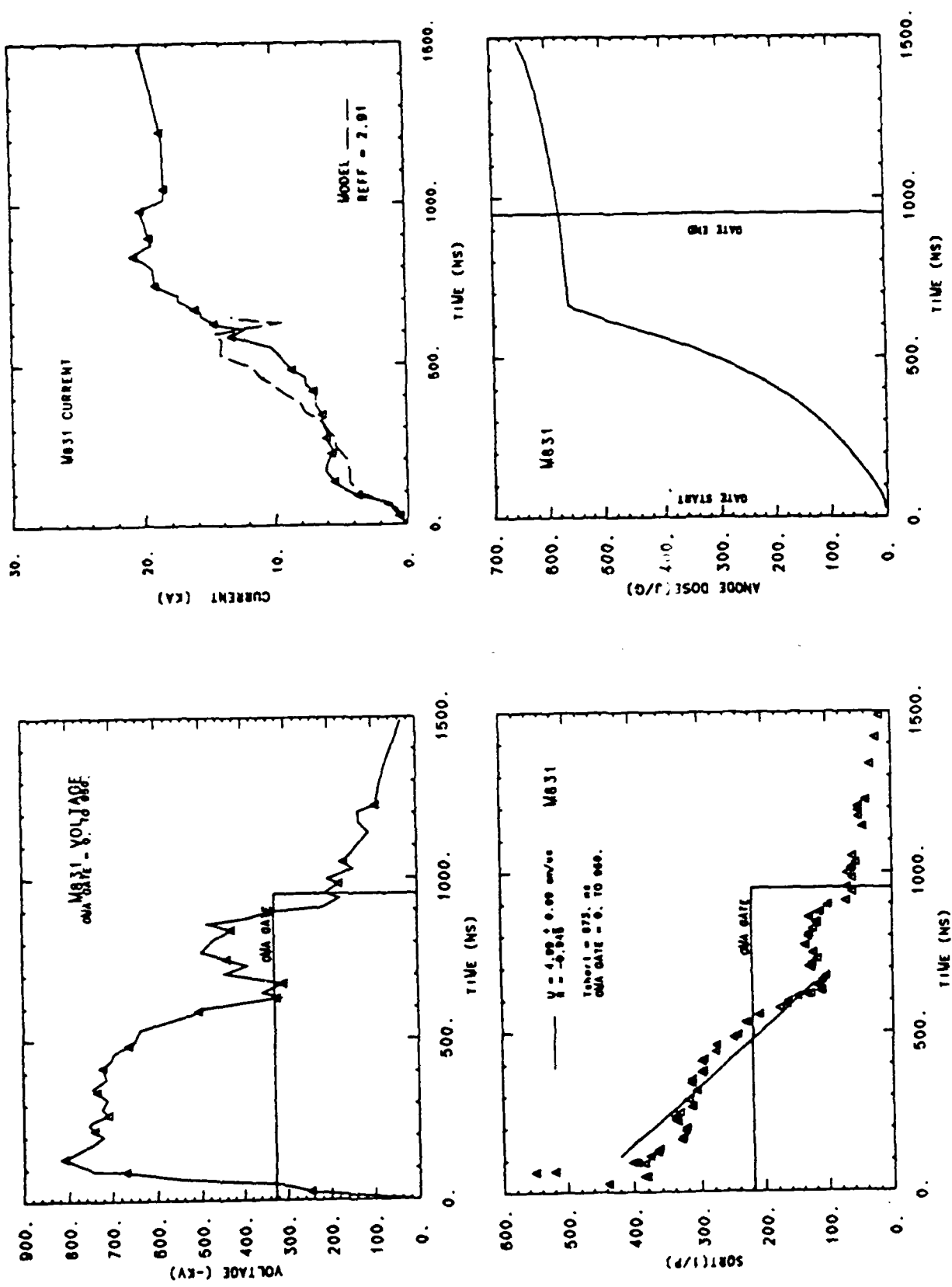NONCROWBAR   M831

Stage: II,Early III ?

4654 CIII,CIV

4262 CII

4068 CII,CIII

Angstroms

3600   3800   4000   4200   4400   4600   4800   5000

Figure 1.22a

Figure 1.22b

NONCROWBAR

M839

Stage: II?, Early III

Boltzmann Temperatures
CII: T = 1.8 ± 0.6 ev (2 lines)

4621 CII
4675 CIII,CIV
4746 CI,CII
4832 CI
4871 H$_\beta$,CII
4933 CI
5152 CII
5698 CIII
5801 CIV
5891 CII

500
400
300
200
100
0

4800   5000   5200   5400   5600   5800   6000

Angstroms
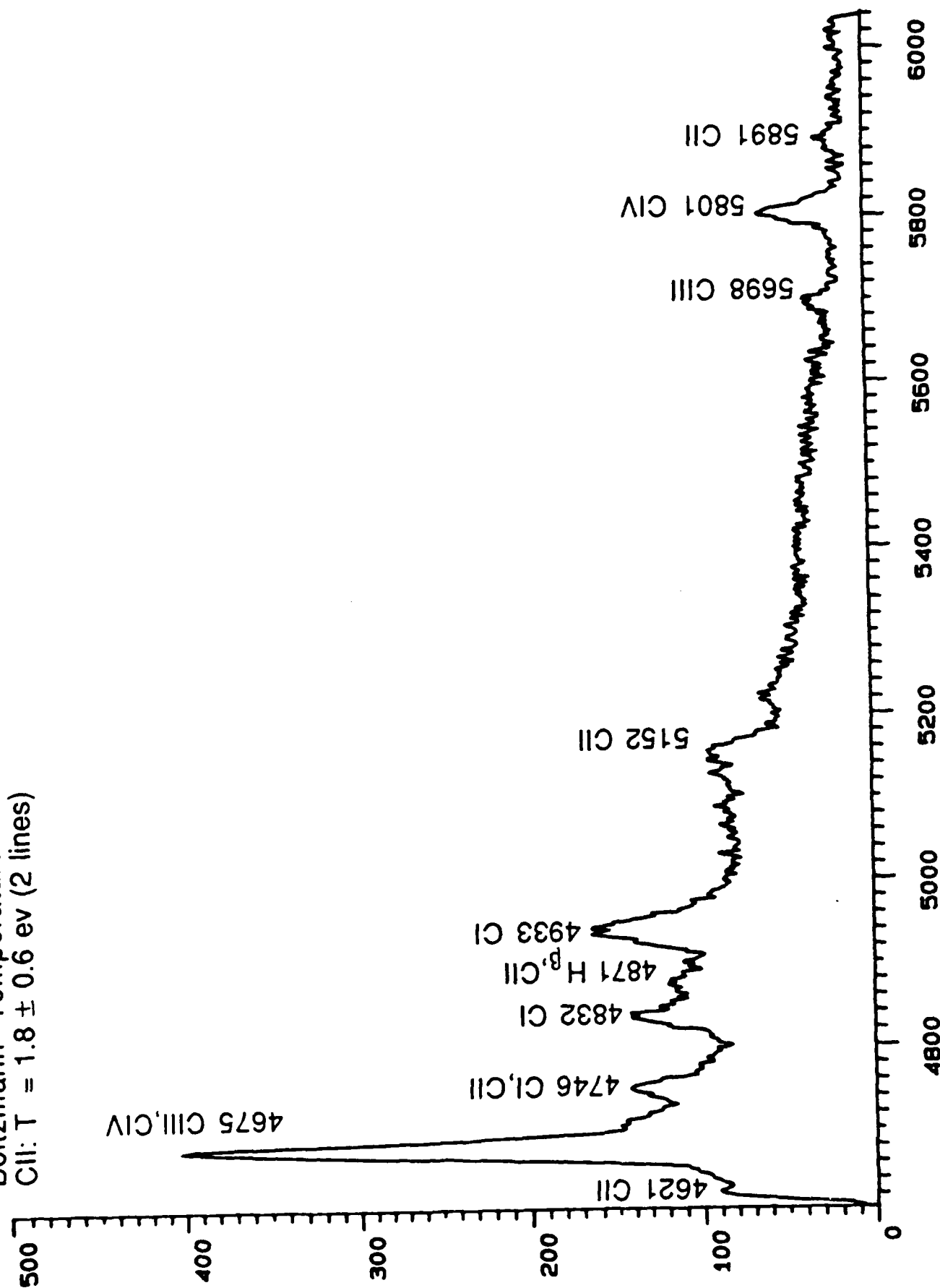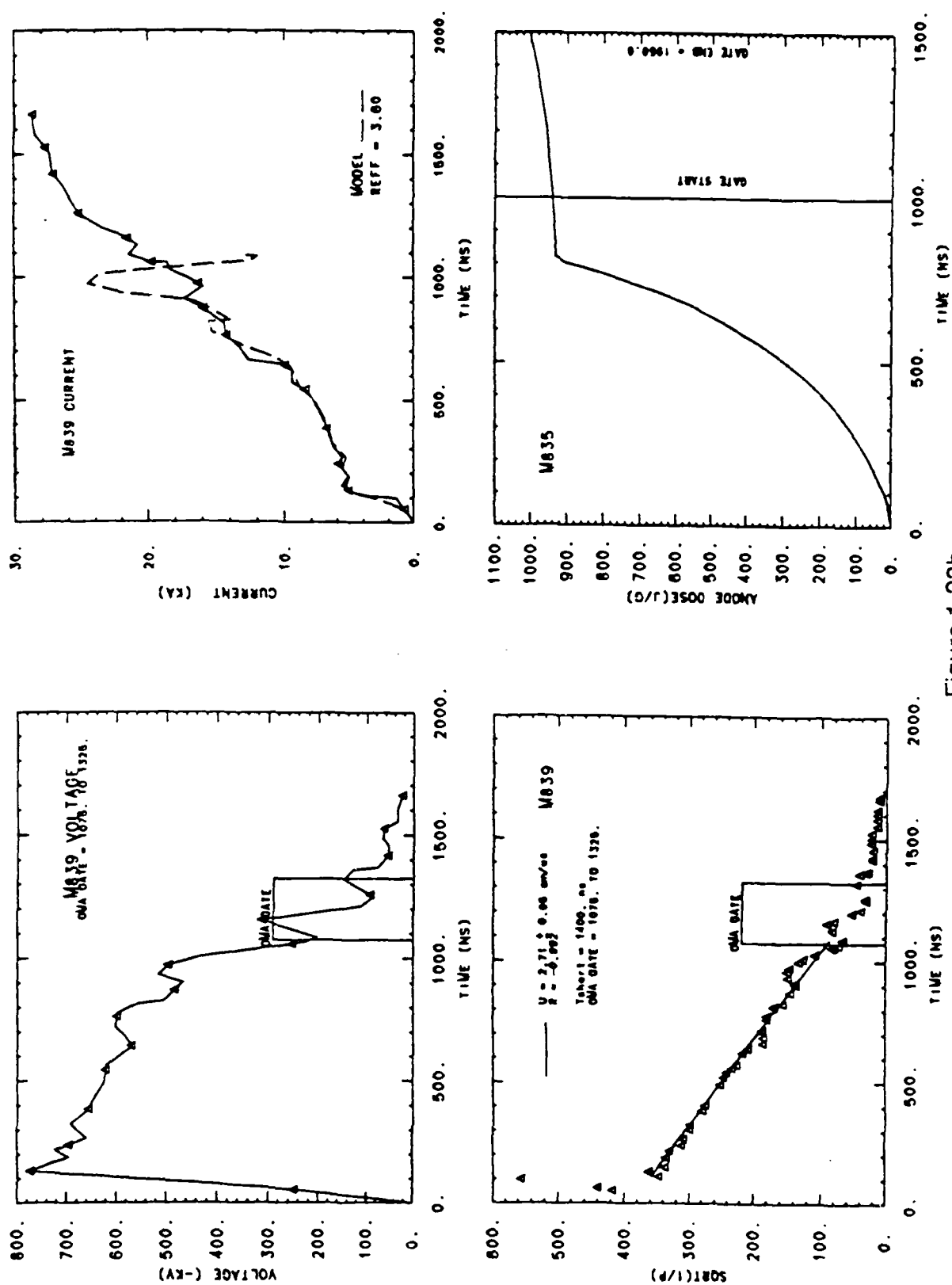
Figure 1.23a

Figure 1.23b

plasma source even had the gate been of smaller width. The next shot is an example of this.

The OMA gate on the next shot is the shortest presented in this report, from 1075 to 1325, only 250 ns wide. The shorting time is 1400 ns (Figure 1.23b), hence the gate ends before predicted shorting. The opening behavior seems to be turning on and off from $\approx$ 950 to 1250 ns, thus preventing a clear interpretation of the spectra. The dose reaches > 940 J/gr. The measured spectrum, Figure 1.23a, shows many highly ionized carbon peaks, including a probable CIV line. Note the change in closure velocity from 5.0 to 2.7 cm/μs in shots M831 and M839 respectively, demonstrating the irreproduceability of the diode load.

The next six shots make up another long time integrated temporal evolution study of the 3 μs following the shot, in two different wavelength regions. A specific discussion of the analysis is not necessary as it is clear that these are all stage III shots. The six shots, their OMA gates, wavelength regions and figure numbers are listed in Table 1.2 below.

Table 1.2

Shot	OMA gate (μs)	Wavelength (Å)	Figure
M835	1.0 - 1.95	3597-5066	1.24a,b
M840	2.05 - 3.1	3597-5066	1.25a,b
M842	3.0 - 4.075	3597-5066	1.26a,b
M836	1.05 - 1.95	4602-6043	1.27a,b
M837	1.95 - 2.95	4602-6043	1.28a,b
M838	3.05 - 4.05	4602-6043	1.29a,b

Each succesive shot has a gate of nominally 1.0 μs wide, with an additional 1.0 μs of delay. The shot M831 gated 0.0 - 0.95 μs is an example of a spectrum taken during the first 1.0 μs. Below are presented various comparisons of total integrated light intensity vs. time. We will ignore randomly varying window attenuation, and differences in calibration and light sensitivity for different grating settings. The actual difference in detectable or emitted light in those wavelength regions may be obscured by these effects. Differences may also be due to changes in diode parameters.
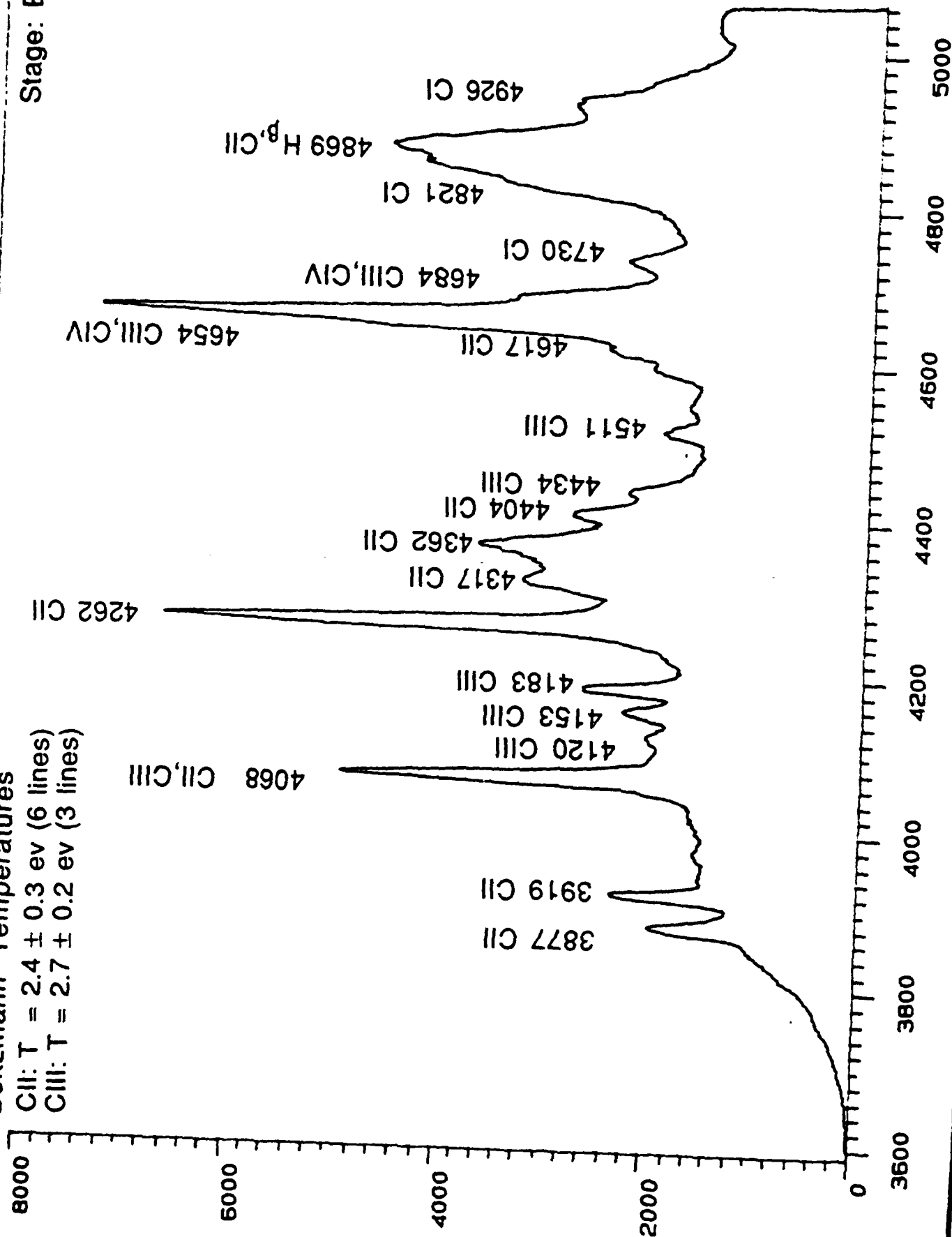
52

NONCROWBAR   M835

Stage: Early III

Boltzmann Temperatures
CII: T = 2.4 ± 0.3 ev (6 lines)
CIII: T = 2.7 ± 0.2 ev (3 lines)

3877 CII
3919 CII
4068 CII,CIII
4120 CIII
4153 CIII
4183 CIII
4262 CII
4317 CII
4362 CII
4404 CII
4434 CIII
4511 CIII
4617 CII
4654 CIII,CIV
4684 CIII,CIV
4730 CI
4821 CI
4869 H$_\beta$,CII
4926 CI

Angstroms
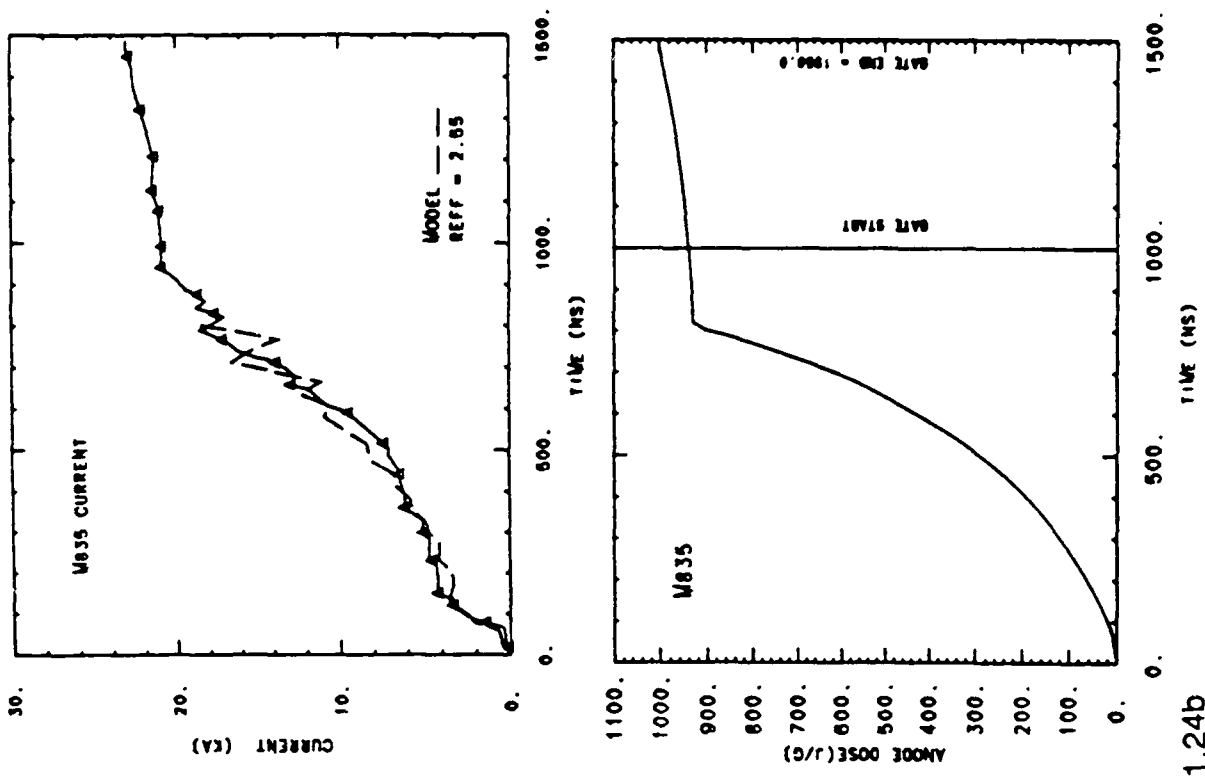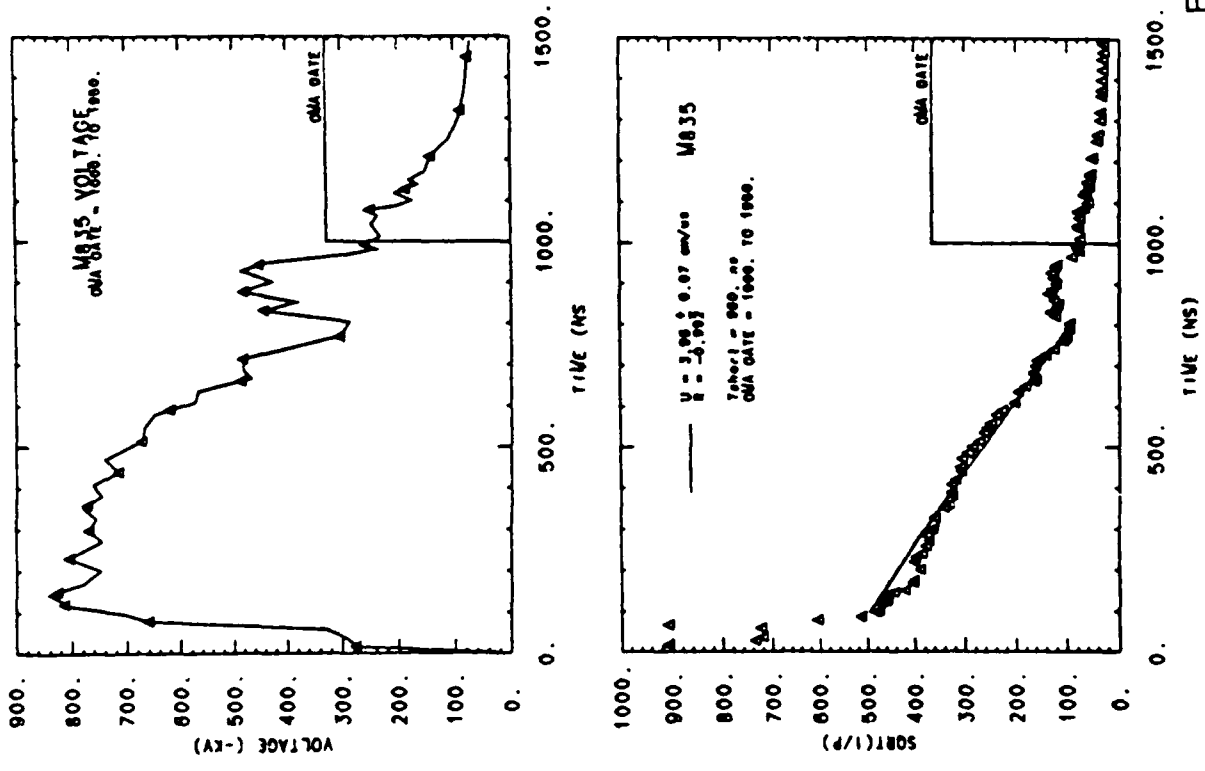
Figure 1.24a

Figure 1.24b

NONCROWBAR
M840

Stage: Middle III

Boltzmann Temperatures
CII: T = 2.8 ± 0.2 ev (6 lines)
CIII: T = 2.9 ± 0.3 ev (3 lines)

3877 CII
3919 CII
4068 CII,CIII
4118 CIII
4153 CIII
4179 CIII
4262 CII
4317 CII
4368 CII
4407 CII
4506 CIII
4617 CII
4654 CIII,CIV
4679 CIII,CIV
4723 CI
4766 CI
4812 CI
4864 H$_\beta$,CII
4920 CI
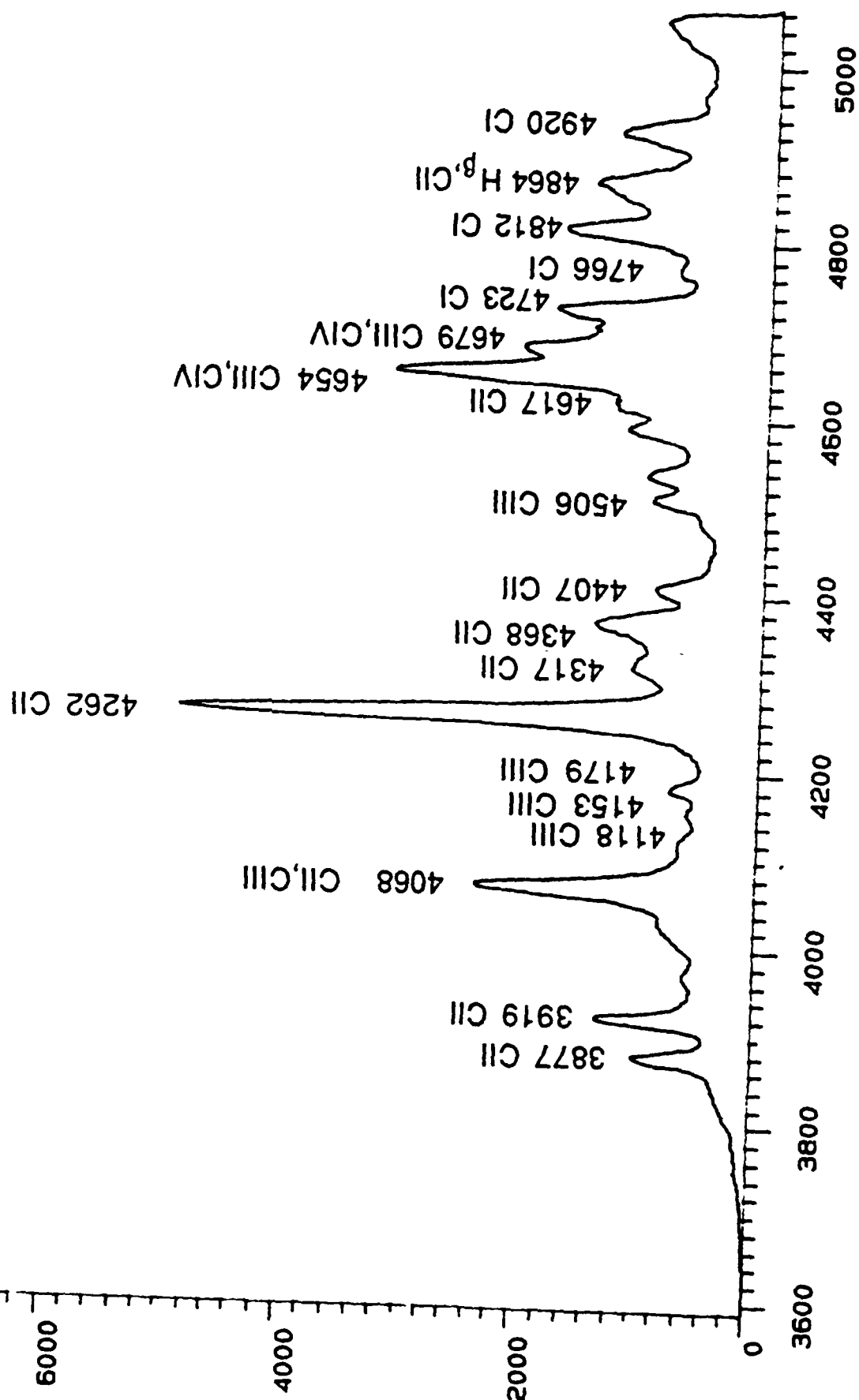
Angstroms
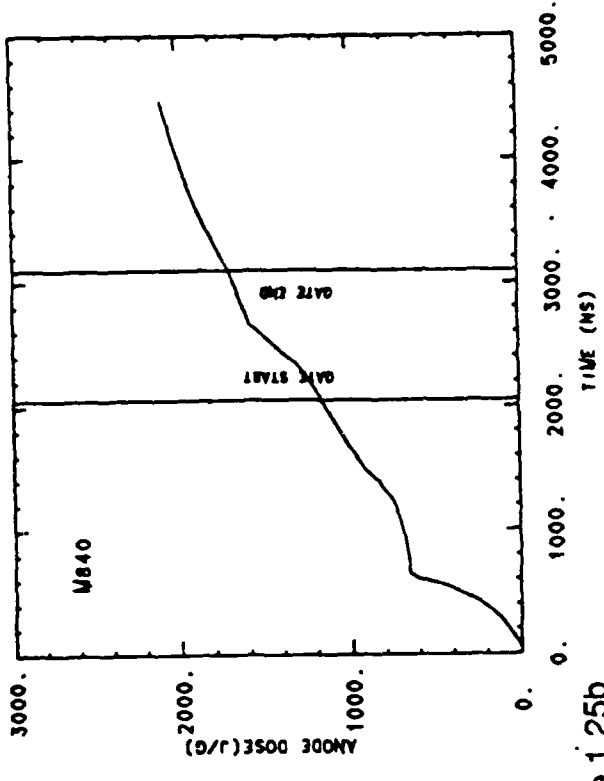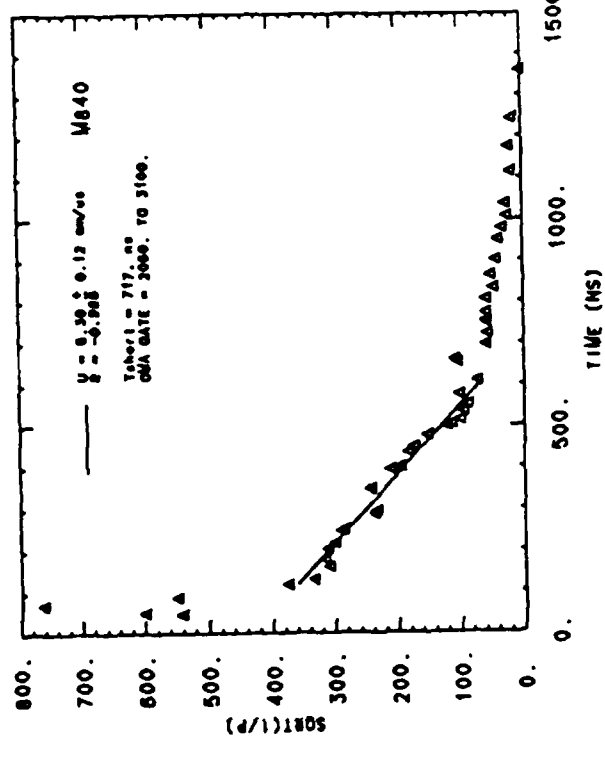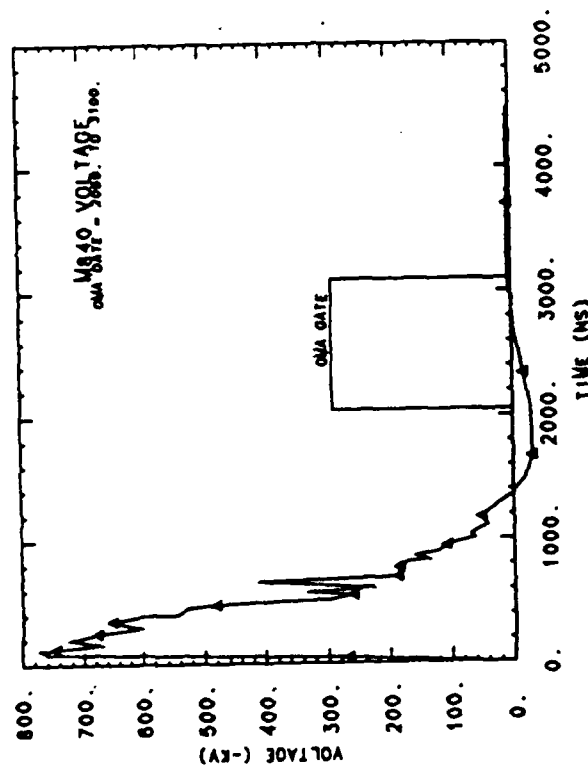
Figure 1.25a

Figure 1.25b

NONCROWBAR

M842

Boltzmann Temperatures
CII: T = 1.4 ± 0.1 ev (3 lines)
CIII: T = 3.0 ± 0.3 ev (3 lines)

Stage: Late III

3964 CI
4026 CI
4062 CI,CII
4265 CI,CII
4372 CII
4408 CII
4508 CIII
4654 CIII
4723 CI
4769 CI
4814 CI
4867 H βCII
4923 CI
5019 CI
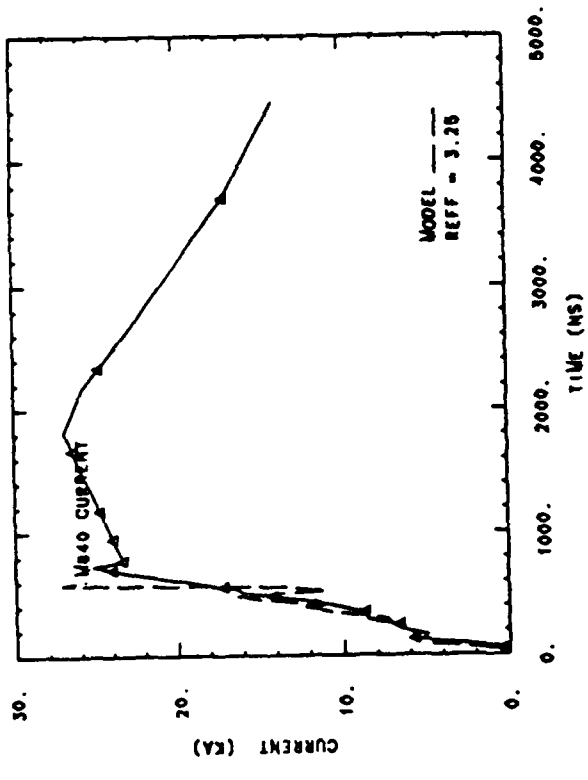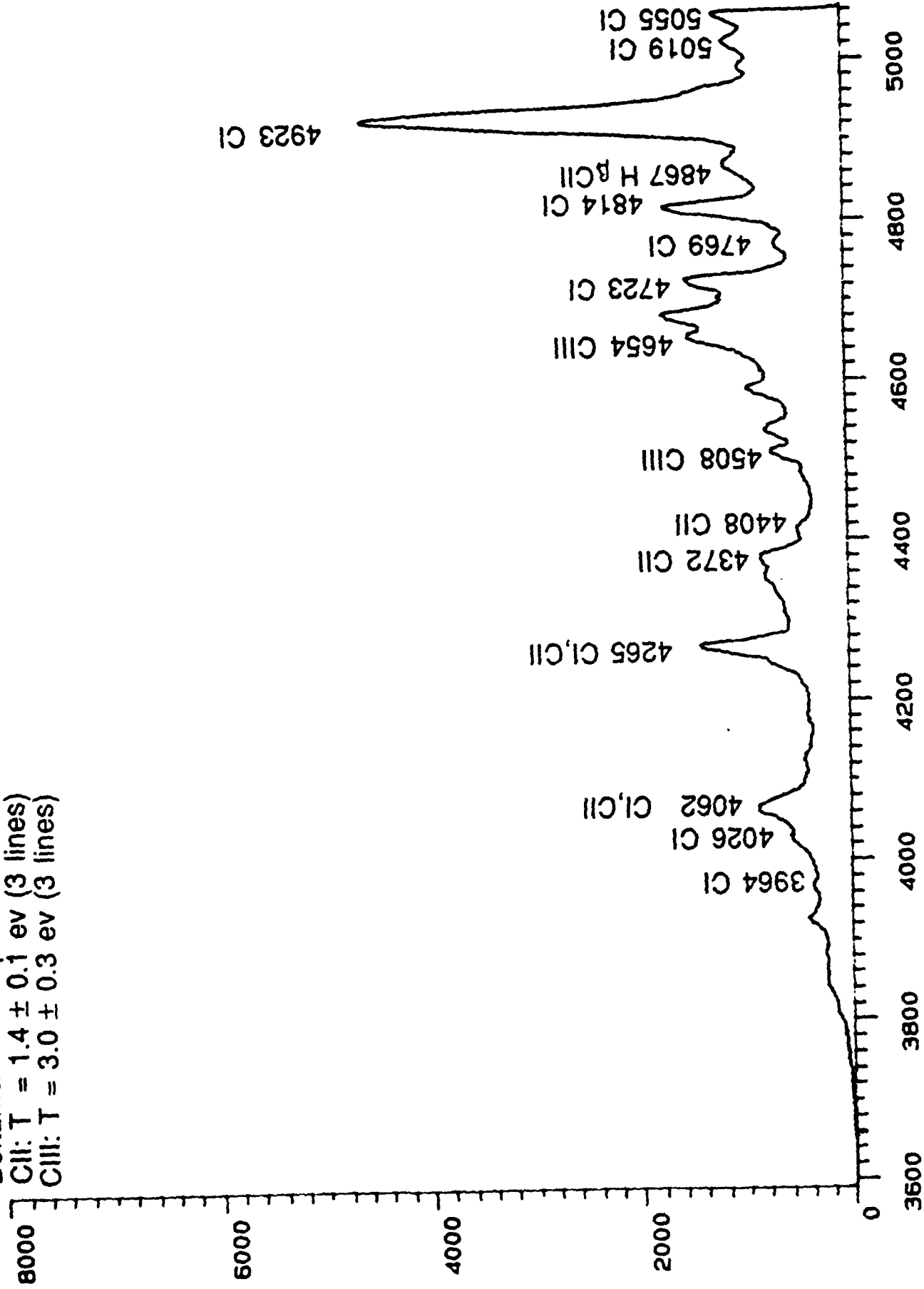5055 CI

Angstroms
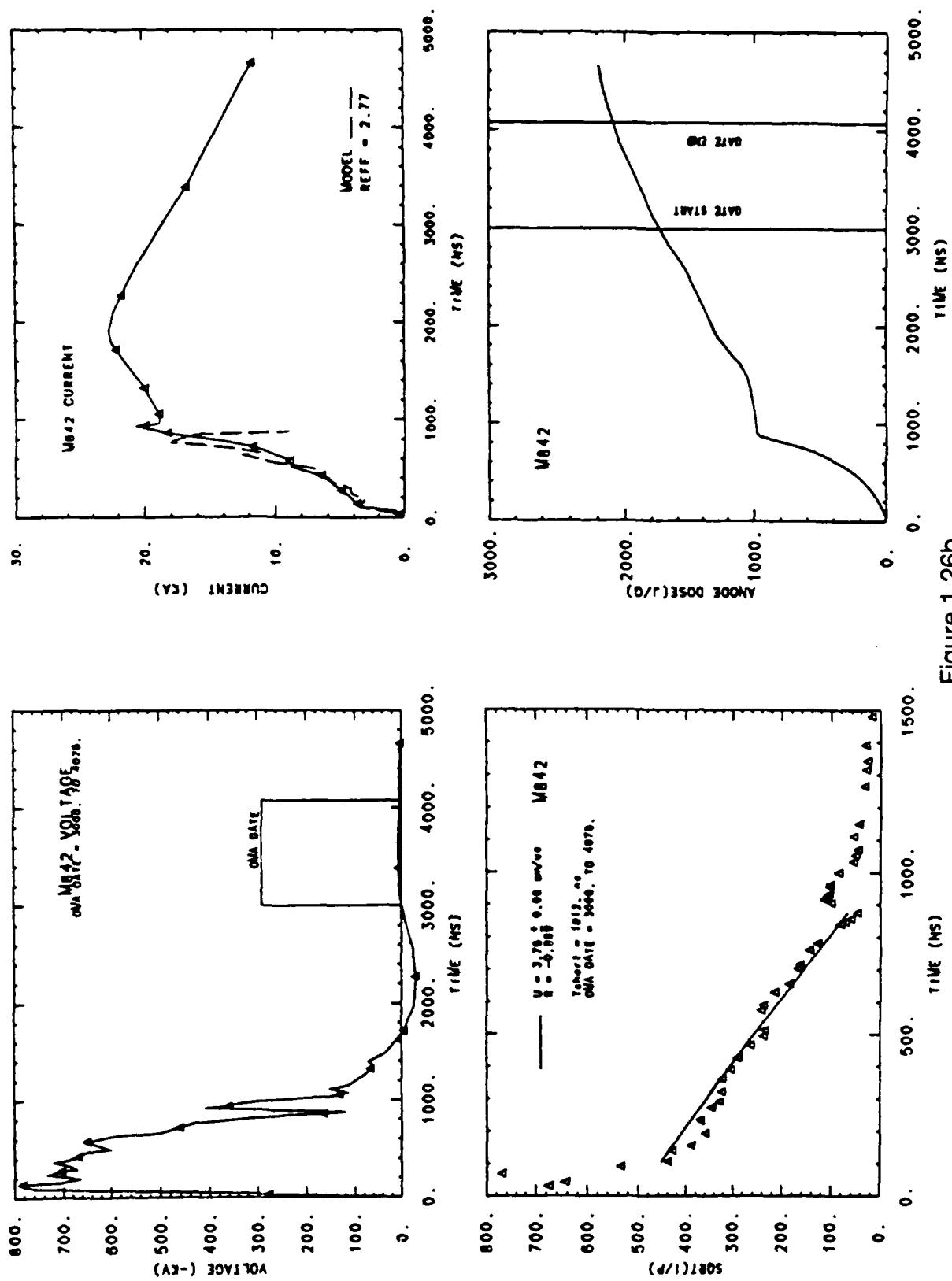
Figure 1.26a

Figure 1.26b

NONCROWBAR

M836

Stage: Early III

Boltzmann Temperatures

CII: T = 1.5 ± 0.3 ev (2 lines)

4673 CIII,CIV

4747 CI,CII

4840 CI

4875 Hβ,CII

4934 CI

5138 CII

5683 CIII

5788 CIV

5798 CIV

5879 CII
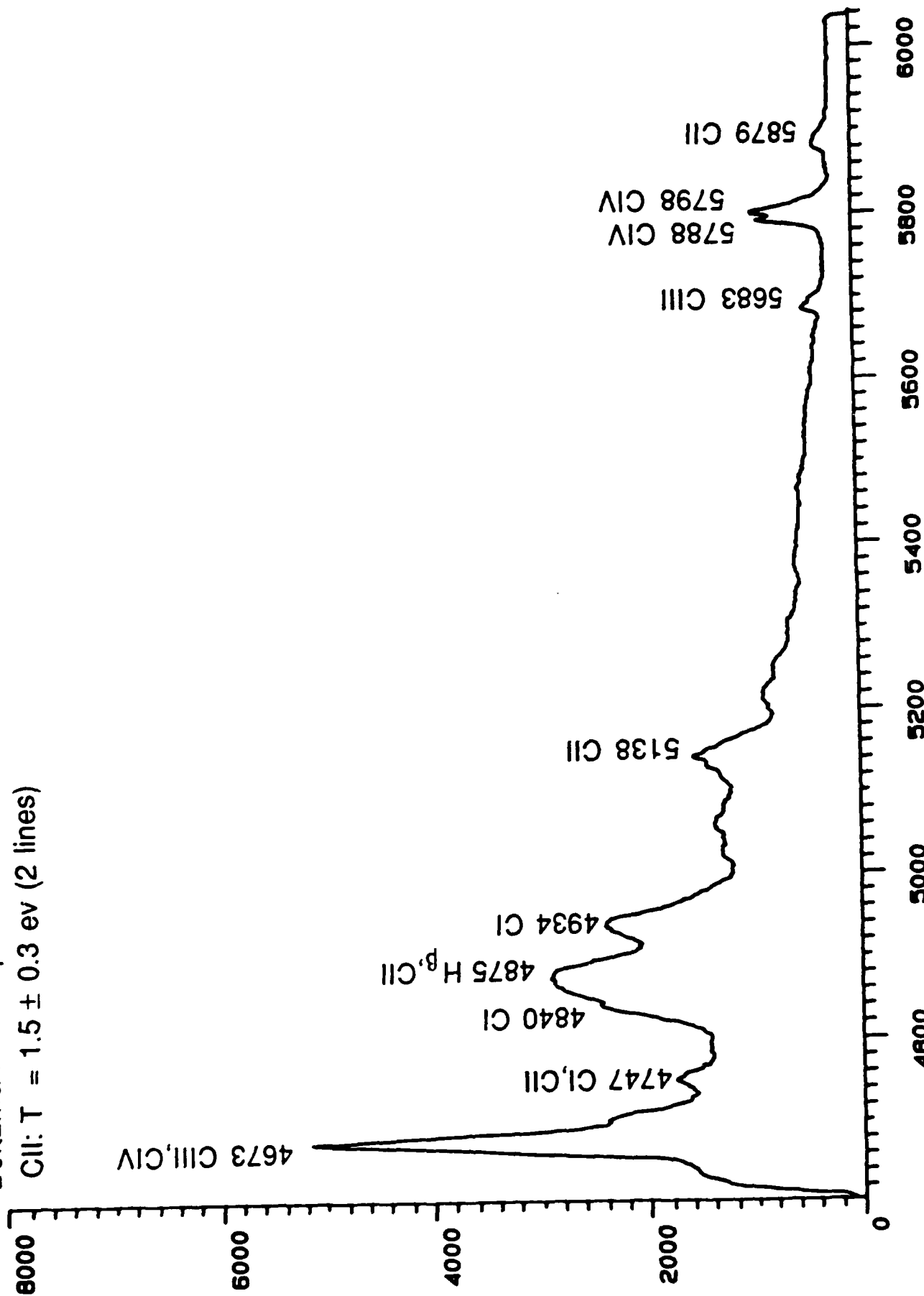
Angstroms

Figure 1.27a

Figure 1.27b

OMA GATE
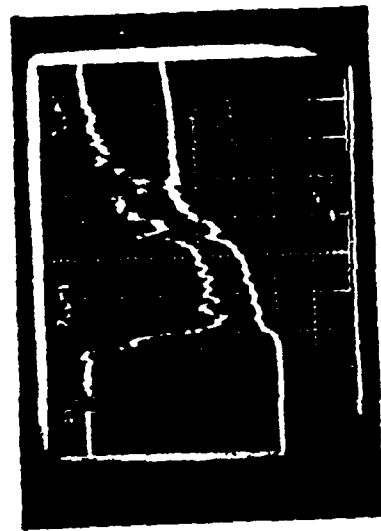
VOLTAGE ≡ 200 KV/DIV

CURRENT 8.4 KA/DIV

NONCROWBAR   M837

Stage: Middle III

Boltzmann Temperatures
CII: T = 2.15 ± 0.6 ev (2 lines)

4673 CIII,CIV
4704 CIII
4743 CI,CII,CIII
4781 CI
4830 CI
4872 H$_\beta$,CII
4929 CI
5051 CII
5154 CII
5787 CI
5889 CII
6020 CI
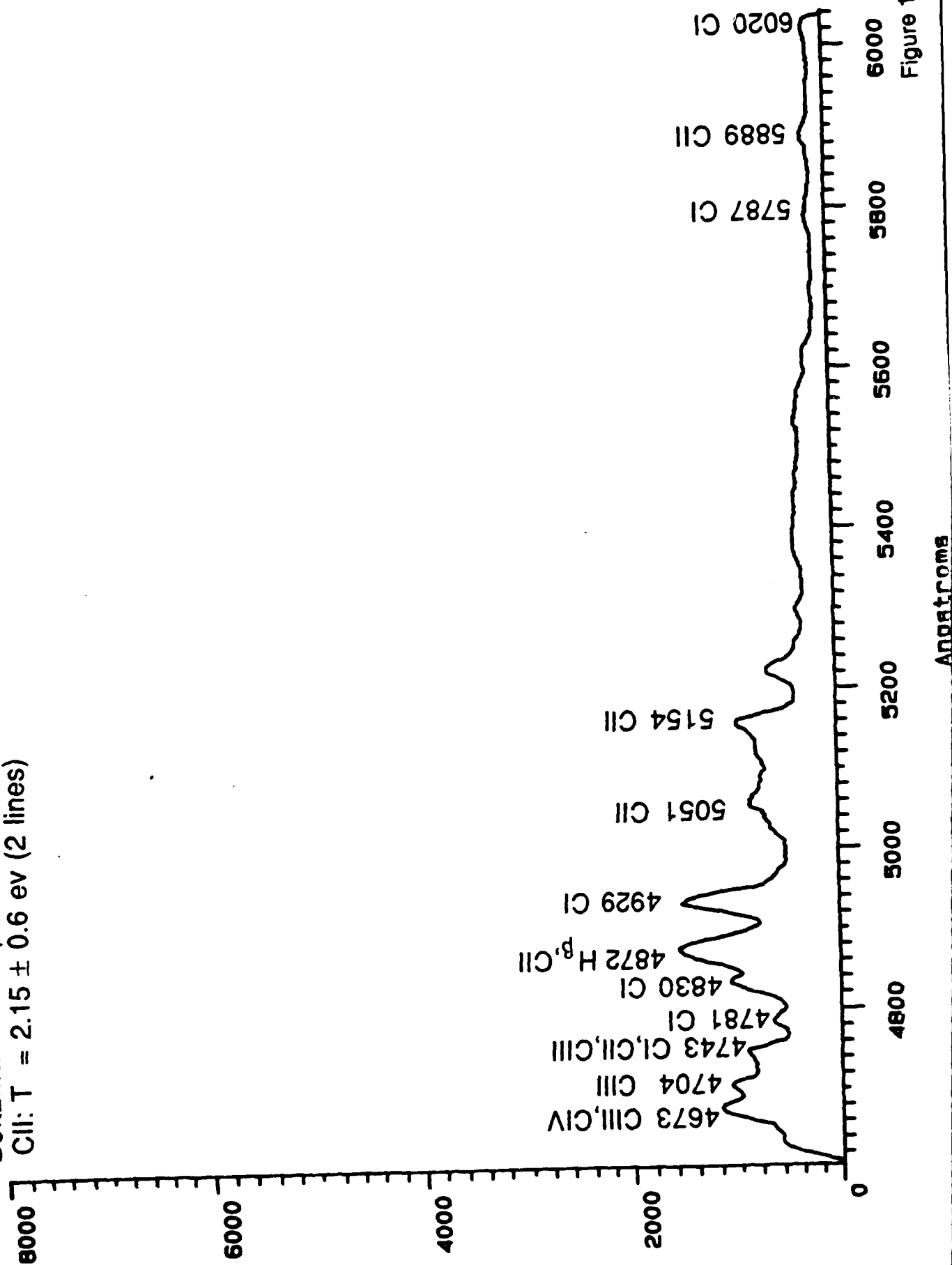
Angstroms
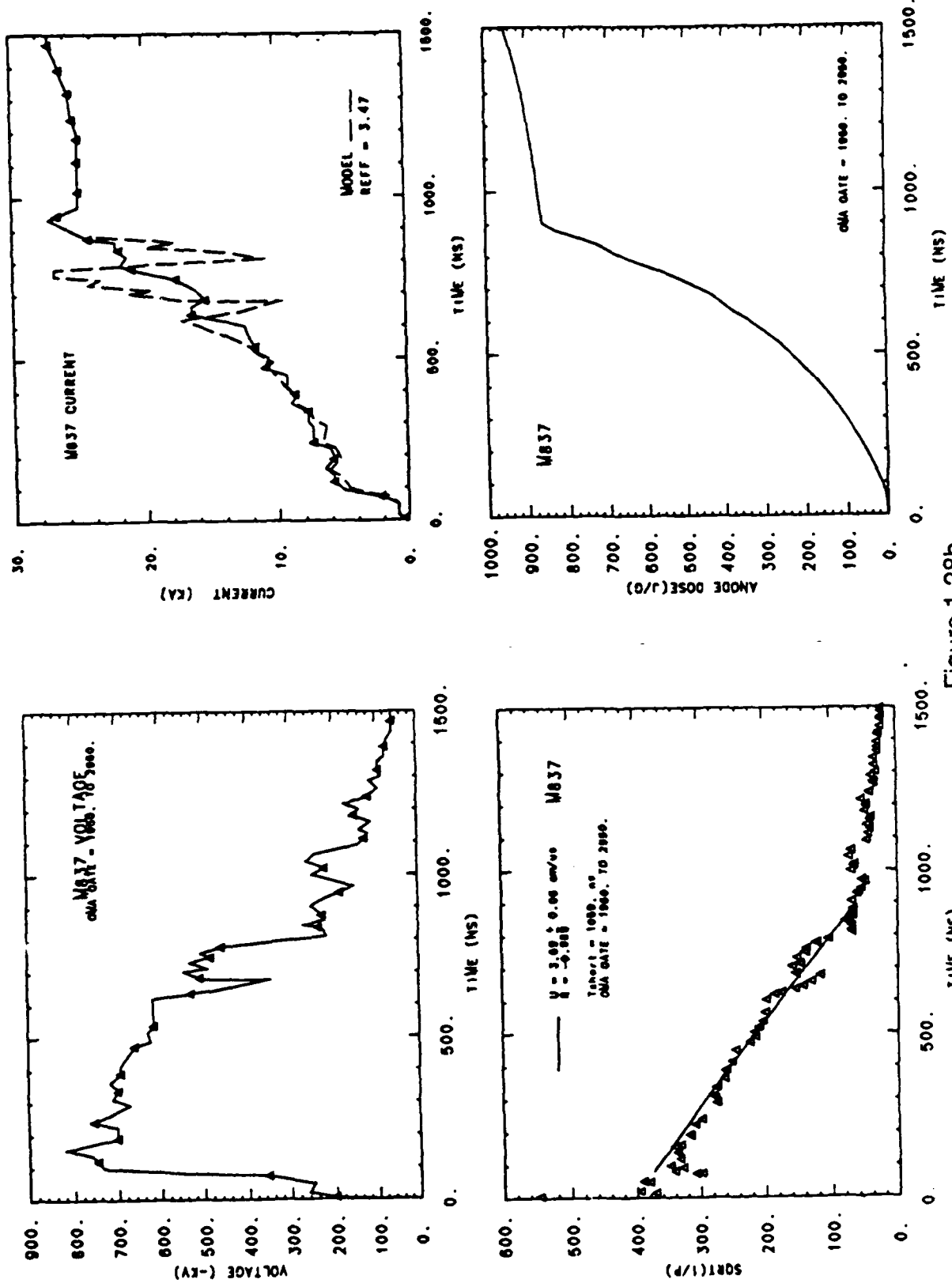
Figure 1.28a

Figure 1.28b

NONCROWBAR

M838

Stage: Late III

Boltzmann Temperatures
CII: T = 1.7 ± 0.4ev (2 lines)

6013 CI

5882 CII

5782 CI

5154 CII

4926 CI

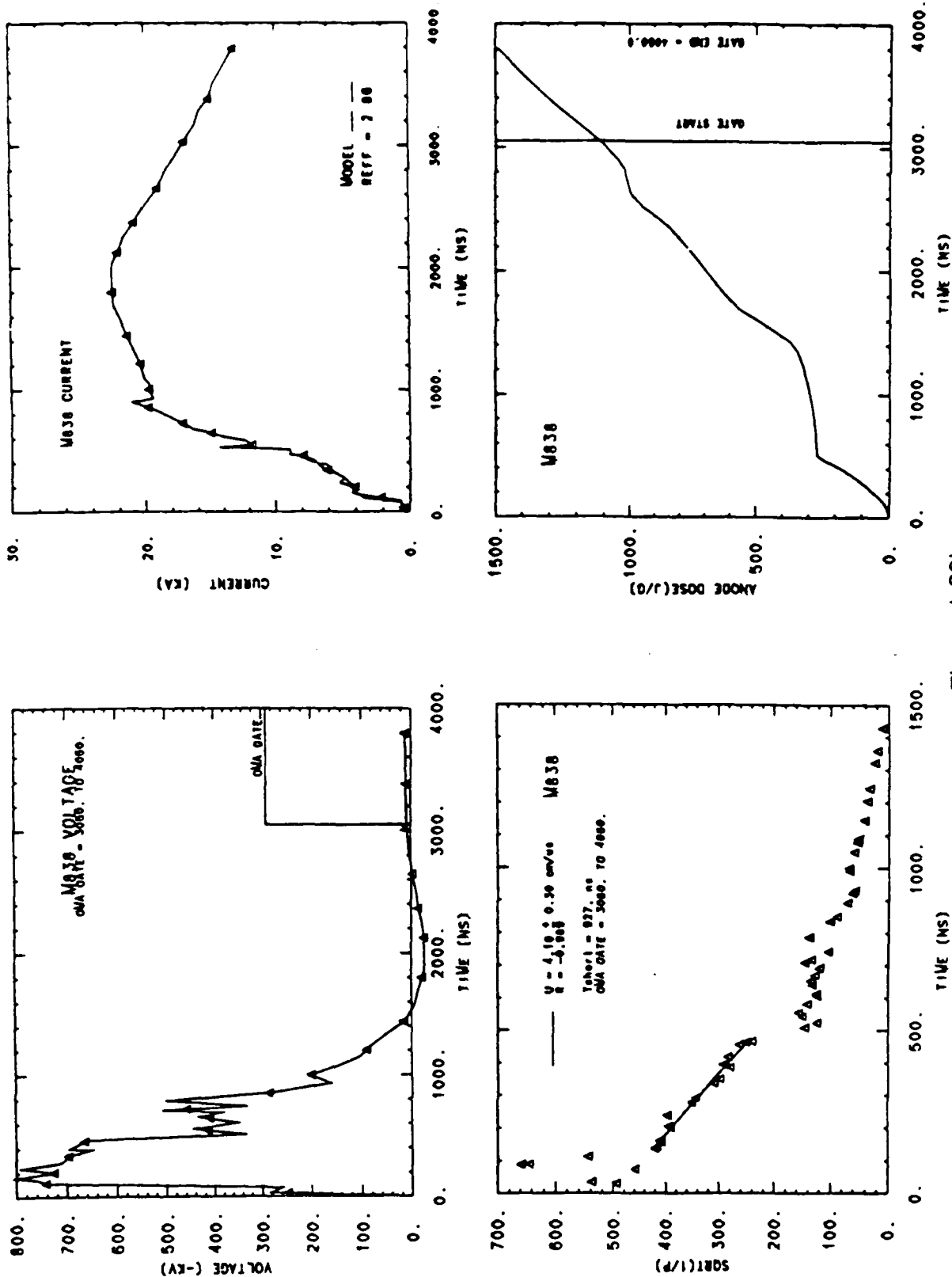4877 Hβ,CII

4832 CI

4743 CI,CII
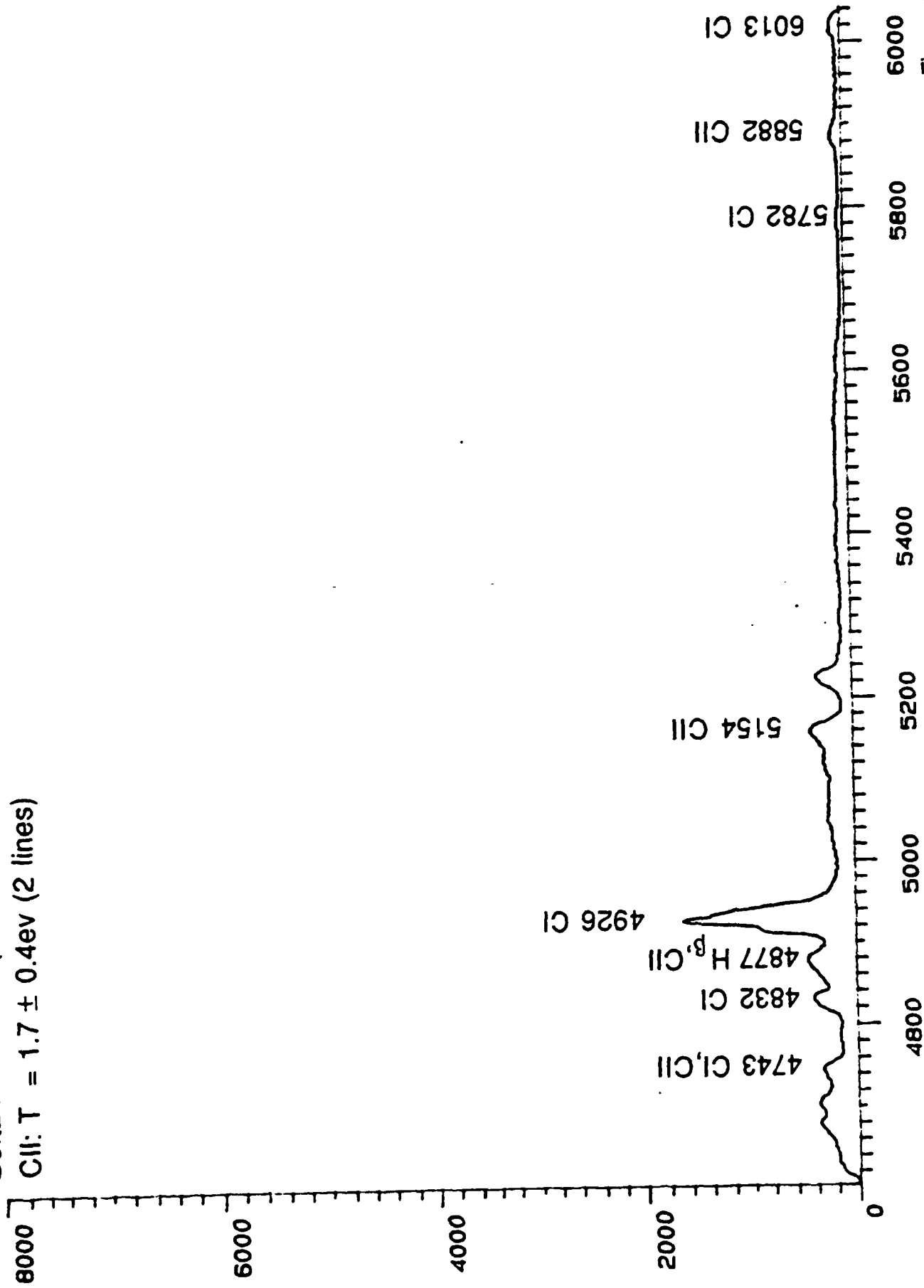
Angstroms

Figure 1.29a

Figure 1.29b

In Table 1.3 are the total number of counts detected in the given wavelength regions (normalizing out differences in OMA gain), and the principal detected species. Table 1.4 presents the same data normalized to the largest integrated intensity overall (on the left) and largest integrated intensity for that wavelength region (on the right). The normalization on the left shows that the most intense emission is immediately following the pulse in the 3597 - 5066 region (shot M835). This is also the period with the most highly ionized plasma. The normalization on the right shows that the time decay of the light intensity is similar in each range. This is significant as the shots were obtained through differently clouded windows. Note also that the sequential time points were not obtained completely sequentially in the shots, which should minimize the systematic error.

Table 1.5 presents the total integrated intensity for the wavelength region 4602 - 5066 Å, the region common to both studies. The numbers in parenthesis are the fraction of the total intensity measured that was in this region. Discounting the randomly varying window attenuation, and randomly varying electron pulse/arc characteristics, the only difference in total light detected at the different settings would be due to the difference in grating sensitivity. The numbers in the third column are the fraction of light detected by the 275 setting (4602-6043 Å) relative to that detected by the 225 setting (3597-5066 Å). If these numbers are fairly constant, the above two effects are either constant or not significant. It appears that the two shots in the 3 - 4 μs period are not consistent. This is probably an effect due to differences in diode behavior.

Table 1.3

Å Region:	3597-5066	4602-6043	principal
Time	Number of Counts		species
0 - 1 μs	32,967		
	M831		
1 - 2 μs	2,085,640	1,008,775	CIII,CII,CIV
	M835	M836	
2 - 3 μs	868,208	507,170	CII,CIII
	M840	M837	
3 - 4 μs	707,713	189,379	CI,CII
	M842	M838	

Table 1. 4
Normalized Counts

Time	3597-5066	4602-6043
0 - 1 μs	0.01/0.02	
1 - 2 μs	1.00/1.00	0.48/1.0
2 - 3 μs	0.41/0.41	0.24/0.50
3 - 4 μs	0.34/0.34	0.09/0.19

Table 1.5

Setting	225	275	
Total Range:	(3597-5066)	(4602-5066)	
Time	Integrated Intensity in 4602 - 5066		275/225
0 - 1 μs	10,155 (0.31)		
1 - 2 μs	876,943 (0.42)	636,659 (0.63)	0.73
2 - 3 μs	374,357 (0.43)	278,155 (0.55)	0.74
3 - 4 μs	411,247 (0.59)	111,151 (0.59)	0.27

On one shot (M839) we gated the OMA just after the pulse from 1.08 - 1.32 μs. This gave an integrated intensity of 62,989 counts. Compare to shot M836 which had a gate from 1 - 2 μs (4 X as long), but gave an integrated intensity of 1,008,775 counts (16 X as many). From the current traces for the two shots we note that the current is still either rising or steady from 1.25 - 2 μs, thus plasma production and/or heating may still be increasing. The time region from 1-2 μs is quite interesting due to the intense light emission and high ionization states detected (up to CIV) and requires further study.

The gates used in this study are very wide, and a lot of integration over the plasma evolution is performed. Tentatively it seems as though recombination begins as the arc current falls. Rising arc current seems to drive the higher ionization states. This study used wide gates to get an initial idea of the species present. Use of shorter gates will alleviate some of the problems associated time averaging and with swamping of details by intense lines. Excitation temperatures versus time are shown in Figure 1.30, derived from the analysis in section 1.2.b.ii. More weight should be given to the data points higher on the plot as they are obtained with more lines in the Boltzmann analysis. The excitation temperature

ELECTRON TEMPERATURES VS. TIME
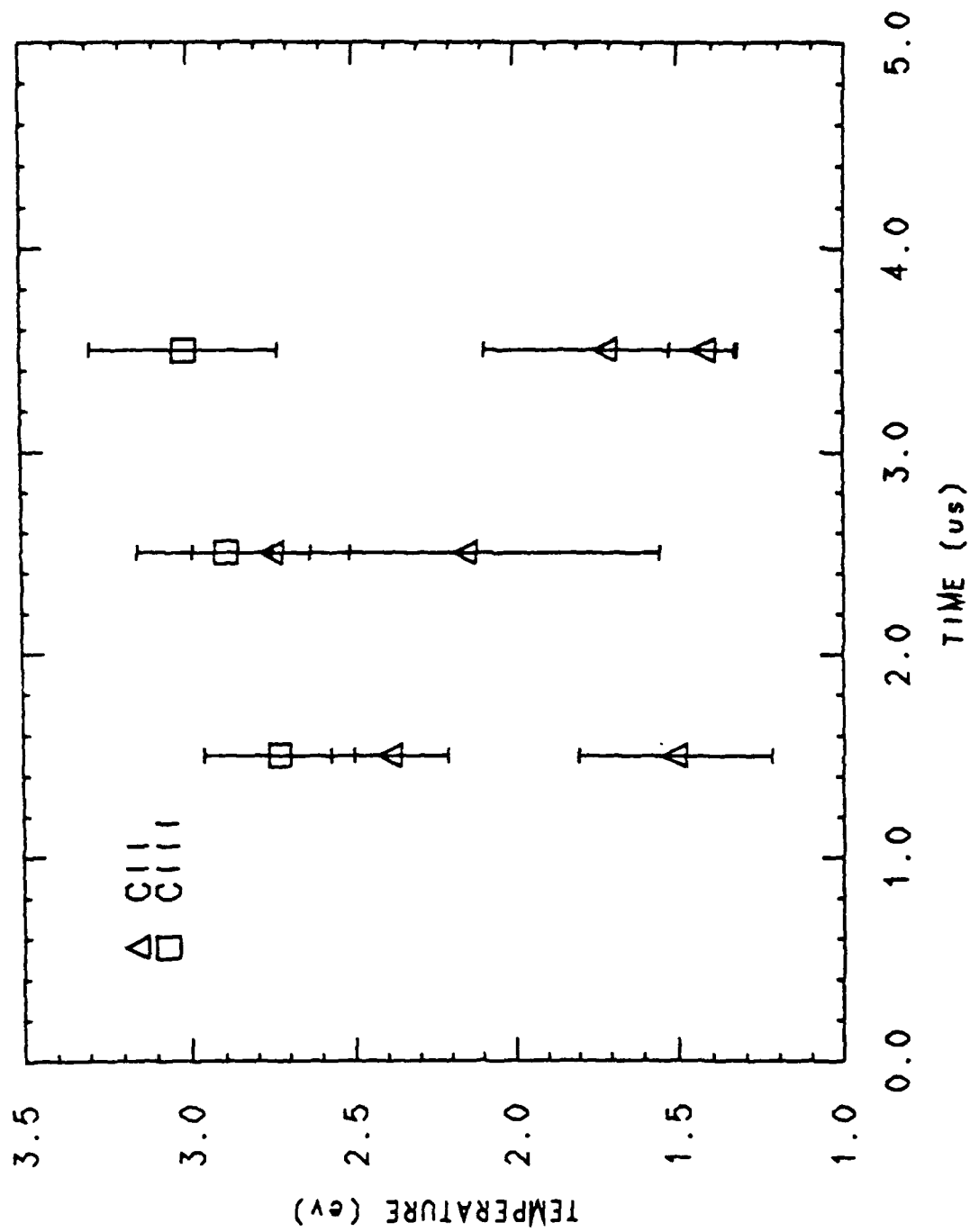FROM BOLTZMANN PLOTS
STAGE III NONCROWBARS

Figure 1.30

appears to be constant in time within experimental error.

The data from Figures 1.24b to 1.29b have been compiled in Table 1.6 to illustrate the irreproduceability of the shots.

Table 1.6

Shot	U (cm/μs)	Reff (cm)	TEND (ns)	TSHORT (ns)	TEND/TSHORT
M831	4.35	2.91	652	874	0.75
M835	3.96	2.55	803	960	0.84
M836	data not available				
M837	3.32	3.68	635	1145	0.56
M838	3.99	2.86	456	952	0.48
M839	2.71	3.60	1089	1402	0.87
M840	5.3	3.25	610	717	0.85
M842	3.75	2.77	876	1013	0.87

In the transition region between stage II and stage III we believe that there is both arc-like behavior and beam behavior (with $V \approx 100$ kV). From the above analysis this is the region with the most intense light emission and the highest ionization states. We have measured up to CIV. Higher ionization states can be detected only at shorter wavelengths than we have explored. We intend to explore this transition region in detail. Shot M835 is an example of a spectrum taken in this region.

The doses during the initial space charge regime are all > 550 J/gr, and keeping in mind the uncertainty in the transition region and arc dose model, the doses approach 2 kJ/gr. Although the mechanism for plasma formation and heating in the arc are essentially different, reaching these high doses during the space charge portion of the pulse could be very important. As discussed above and in the conclusion section, there are several methods we can use to do this. The plasmas created in stage III are also interesting themselves as tentative analysis (see section 1.3.b.ii) indicates they may be nonequilibrium plasmas. The high currents and low energies in stage III result in substantial coupling giving very intense light emission from a highly ionized plasma. This is probably due to both heating of stage II plasma inventory and the creation of new plasma inventory through anode spot mechanisms.

1.4) Conclusions on Electron Beam Pumped Carbon Experiments

In stage I the deposited electron dose is smaller than that required for anode plasma formation. No light is detected in this phase.

In stage II the deposited electron dose is large enough for anode plasma formation before diode shorting. Spectroscopic data for noncrowbarred shots (dose $\approx$ 500-800 J/g) indicate the presence of CII and CIII with a high level of background radiation.

In stage III the cathode plasma begins shorting the anode cathode gap or anode and cathode plasmas meet. For crowbarred shots (dose>300 J/g) molecular emission from C_2 and CH and atomic emission from CII and H is observed. Noncrowbarred shots exhibit intense atomic emission; at early times CII and CIII are the primary components, however emission from CIV has also been observed. Excitation temperatures from Boltzmann plots are 2-3 eV. At later times the emission is primarily from CI and CII with $T_{ex} \approx$ 2-3eV. The electron density is found to be $\approx 10^{18}$ cm^{-3} from the Saha equation.

Future experiments will emphasize increasing the current density to obtain higher anode doses. The principal method for increasing the current density will be the use of an external magnetic field. Diode aspects which will increase the current density are decreasing the gap, and redesign of the cathode/anode geometry.

2.0) Spectroscopy of Electron Beam Interactions with Helium

Visible emission spectroscopy was performed on electron beam produced helium plasmas using the experimental set-up shown in Figure 2.1. The Febetron electron beam accelerator was used for these intial studies because it operates with a higher repetition rate and does not destroy the anode foil, permitting many more shots.

Typical emission spectra for helium is shown in Figure 2.2. We did not observe the 468.5 nm (4-3) transition, which had been observed by Bunkin et al.[2.1] to undergo stimulated emission. All of the emitted spectral lines were identified as neutral helium. The electronic temperature calculated by comparing the individual helium line intensities was found to be ≈ 0.8 ev. This is much lower than the 2 ev electronic temperature measured for argon and krypton under similar experimental conditions. Further studies are in progress to account for this discrepancy and also to investigate the production of HeII. We are currently running high pressure (100 torr to 2 atms) experiments to determine the effect of pressure on temperature and degree of ionization.

During the course of examining the emission spectra from helium plasmas produced by a relativistic electron beam we found that if very small amounts of air (as small as 50 millitorr or less) were present as an impurity in the interaction chamber that two very large intense lines were observed at 391.4 and 427.8 nm. These two lines correspond to the (0-0) and (0-1) vibrational transitions in the first negative band of N_2^+, $B^2\Sigma_u^+$ - $x^2\Sigma_g^+$. When the N_2 lines were present, the lines originating from helium had negligible intensities! We pursued this important effect as is described in the following paragraphs and published in Applied Physics Letters, (reprint attached).

We very carefully added measured amounts of N_2, which ranged from 0.1 to 10 Torr partial pressure and helium, partial pressures from 0.1 to 500 Torr. In time-resolved studies performed with the Optical Multichannel Analyzer (OMA), gates of 50 ns delayed by 20 ns for each pulse, the N_2^+ light emission was found to follow the beam voltage after the initial rise time (see Figure 2.3). During the time resolved studies, no other lines were observed except for the 391.4 nm and 427.8 nm nitrogen

bands. Figure 2.4 shows the relative intensity of the 391.4 nm band as a function of helium to nitrogen ratio for nitrogen partial pressures of 0.1, 1 and 10 Torr. Figure 2.5 shows similar results for the 427.8 nm band. Figure 2.6 shows emission spectra for a variety of helium pressures.

As seen in Figs. 2.4 and 2.5, the largest light intensities at 391.4 and 427.8 nm for a given pressure of nitrogen occur for the largest ratio of He/N_2, i.e. the smallest amount of N_2. Also, the more helium present, the more light is produced up to total pressures of about 300 Torr where the intensity levels off. The linear portion of the curves correspond to a slope of about 1 for the range of total pressure 10 - 300 Torr for the cases where the N_2 partial pressure was 1 and 0.1 Torr. The slope was 0.5 when the partial pressure of N_2 was 10 Torr. For cases where the helium partial pressure is smaller or about the same as the nitrogen partial pressure, there is very little increase in the N_2^+ lines compared to the case of nitrogen alone.

As seen in Fig. 2.2, the largest intensity lines observed when no added nitrogen was present were 388.8, 447.1, 501.5, and 587.5 nm. In the case of the 388.8 nm line, the energy of this transition is very close to that of the N_2^+ 391.4 nm band. Therefore, a possible mechanism for the excitation of this band is

$$N_2^+ (X^2\Sigma) + He (3^3P) -> N_2^+ (B^2\Sigma) + He (2^3P).$$
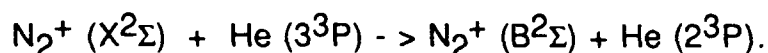
Since the slope of the log of the intensity as a function of the log of He/N_2 is close to 1 for small N_2 partial pressure cases, there appears to be a one to one correspondence between the number of photons emitted for the given bands and the number of helium atoms present, above a particular helium to nitrogen threshold. This one to one correspondence is consistent with the above reaction and a simple kinetics model. The details of the kinetics model are given in the attached reprint.

For formulating a model of four simple reactions, we can solve for the time rate of change of the $He(^3P)$ state, which is then used to find the time rate of change of $N_2^+(B^2\Sigma)$. From these solutions we can show that the emission rate for N_2^+ $(B^2\Sigma - X^2\Sigma)$ is linearly proportional to the electron beam density (which we observe), the ground state population of

71

N_2^+ and most importantly linearly proportional to the He ground state concentration. This is an important result because other investigators who have examined the effects of helium on the N_2^+ laser have felt that the N_2^+ emission is the result of interactions with He_2 or He_2^+ or more complicated processes which turn out to be precluded by our results.

We recently published these results in Applied Physics Letters and presented a paper at the 38th Annual Conference on Gaseous Electronics where they were well received.

As mentioned previously, now that we have fully investigated the effects of air impurities on our helium emission spectra, we are setting up our experiment to eliminate this effect so that we can examine the interaction of the electron beam with helium alone. We plan to investigate the possibility of stimulated emission in helium, particularly for high pressures (> 1 atm).
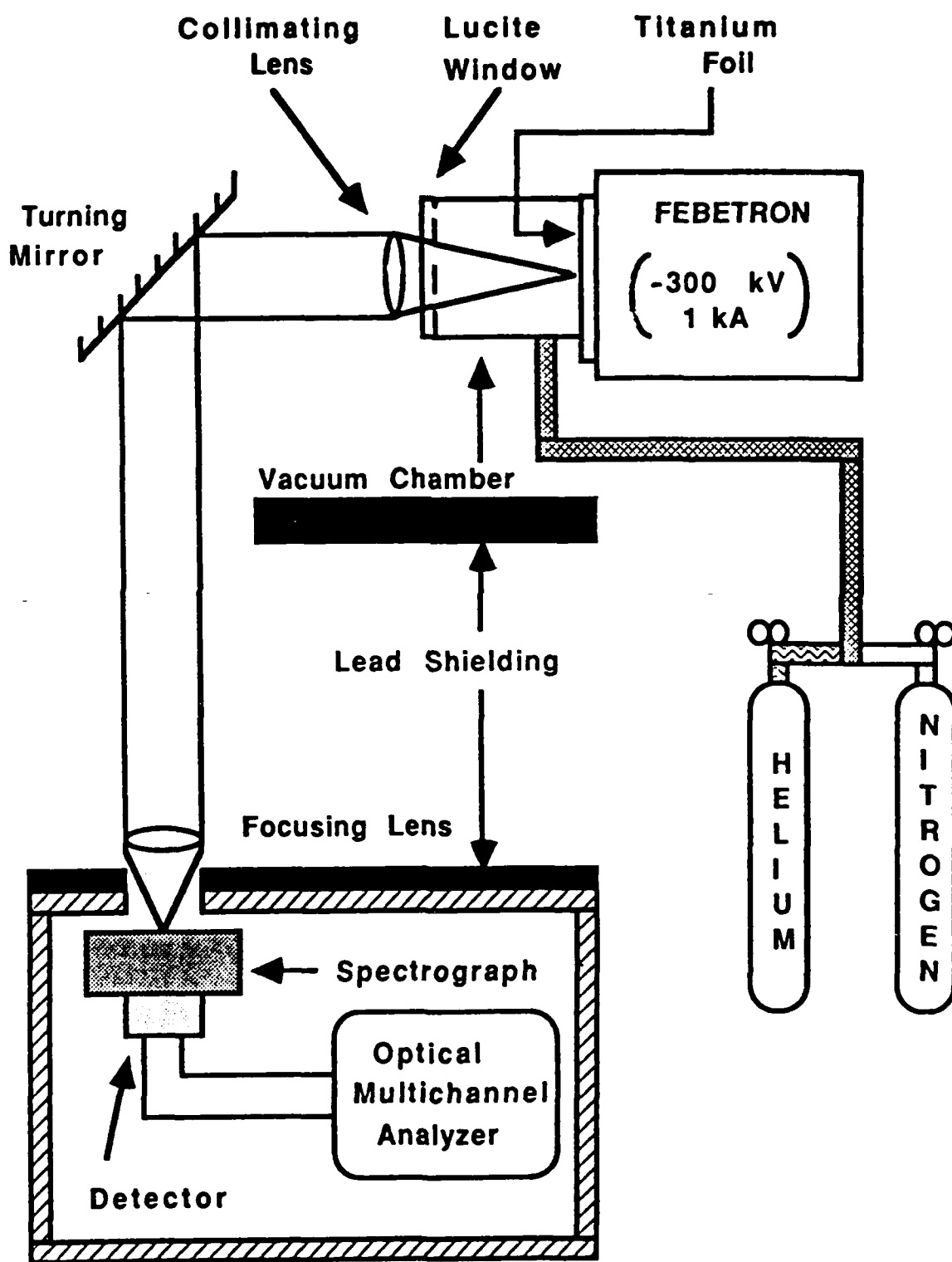
Figure 2.1

Spectrum of Beam Interacting with Helium (10 Torr)

F5057

5016 HeI

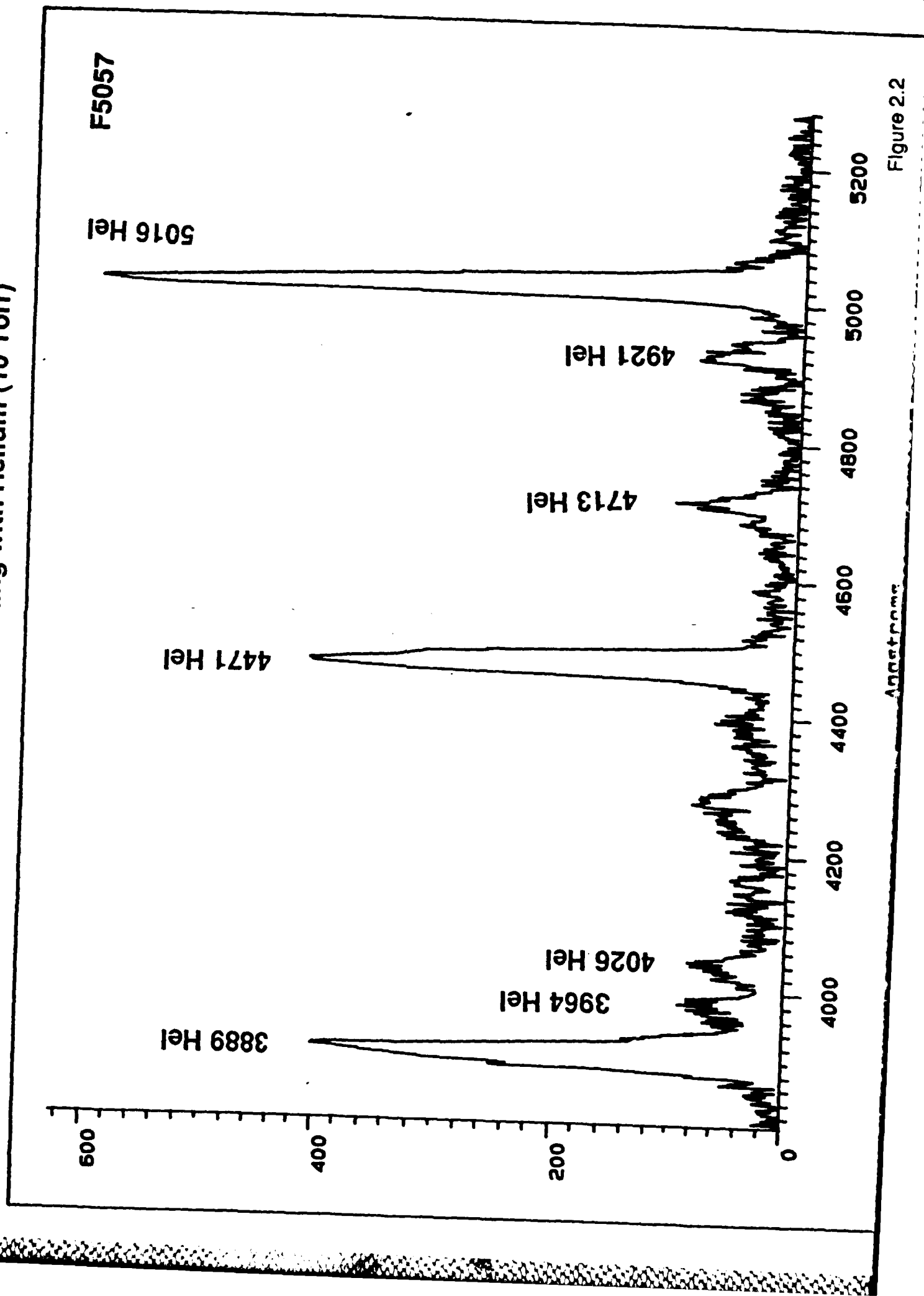4921 HeI

4713 HeI

4471 HeI

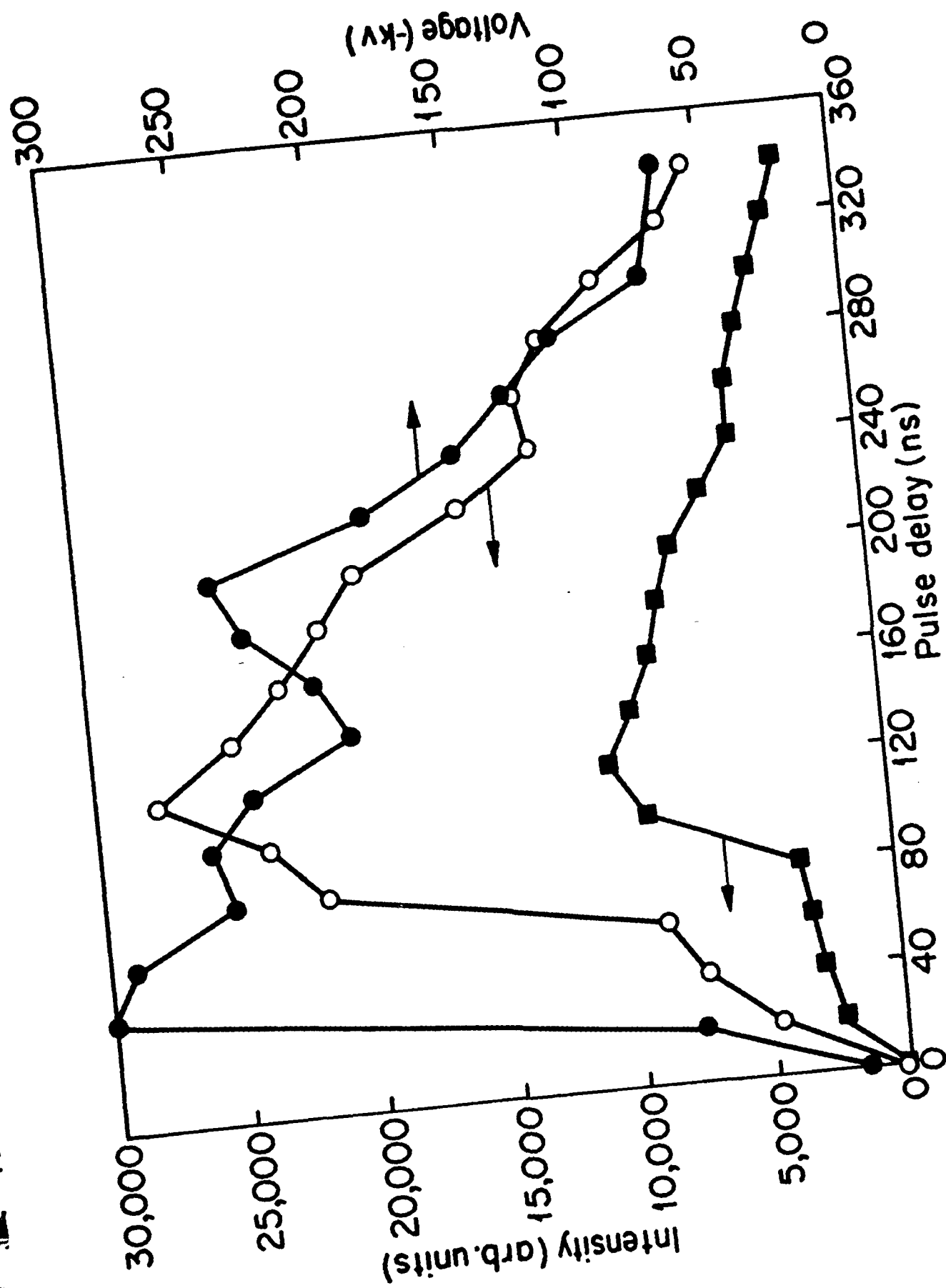4026 HeI
3964 HeI

3889 HeI

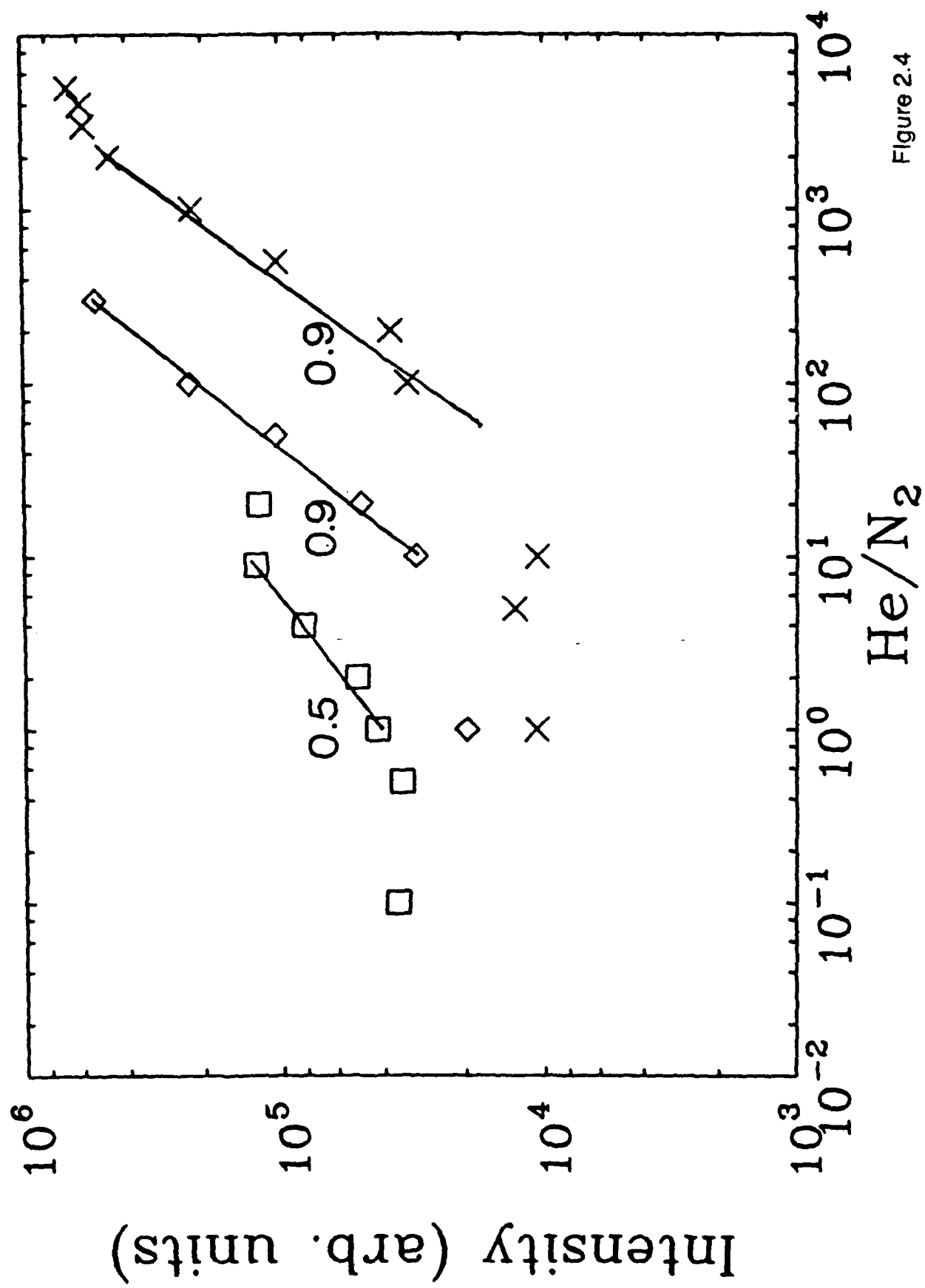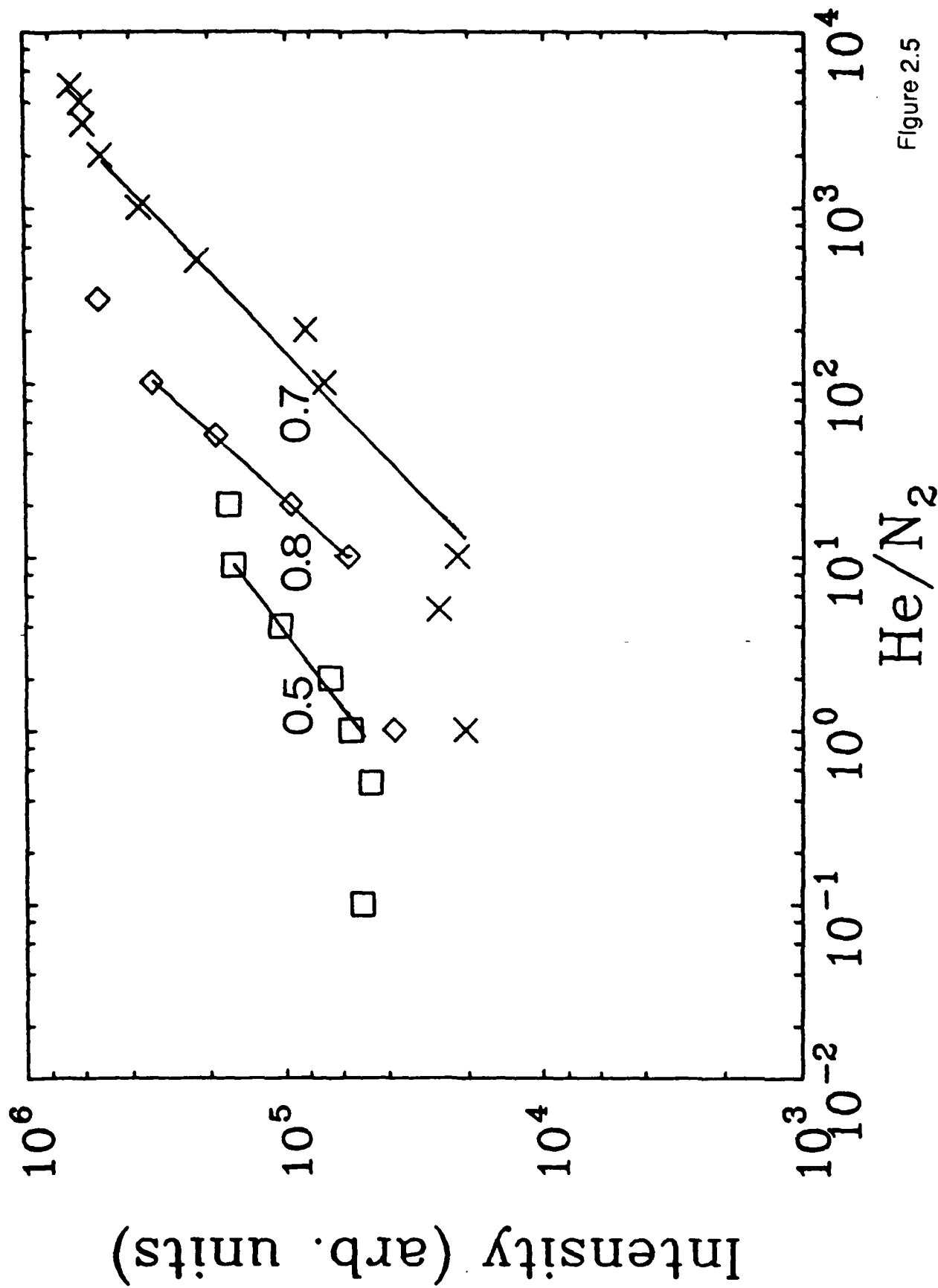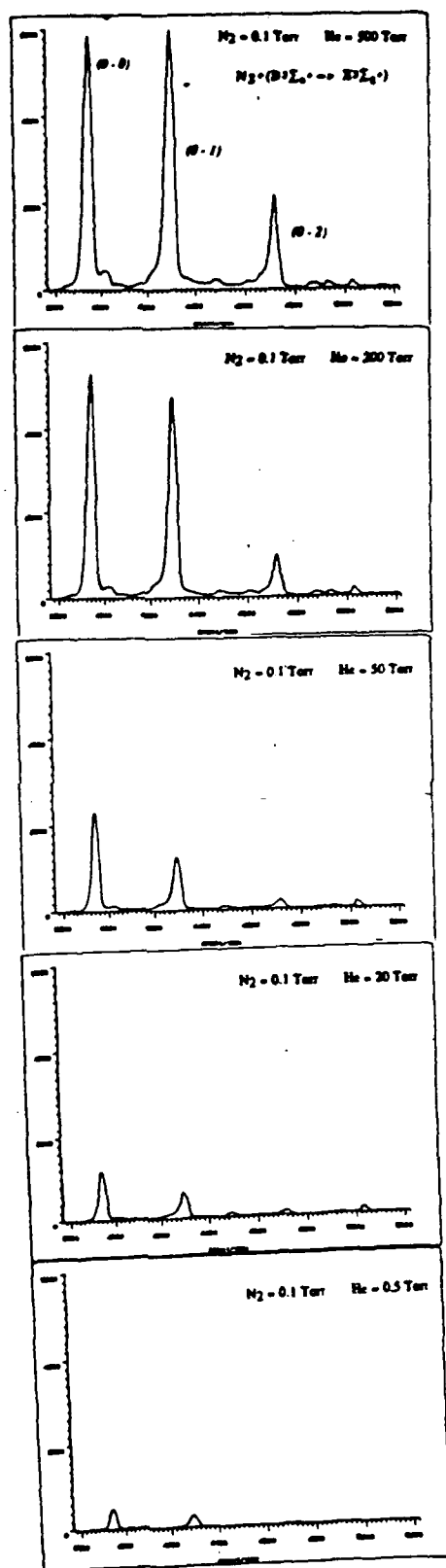Angstroms

Figure 2.2

Figure 2.3

Figure 2.4

Figure 2.5

Figure 2.6

3.0) Theoretical Research

This is a summary of the work being done, as of November 1986, to explain the experimental observations of a carbon plasma heated by an incident electron beam. An overveiw of the theory is presented as well as a description of proposed work.

The main goal of the investigation is to formulate a theoretical model which will describe the motion of the carbon plasma and predict the spectrum of emitted light. The predicted spectra may then be directly compared to spectra which are experimentally measured. The model being currently developed is based on work done by J.W. Thornhill.[3.1] Three main areas must be addressed: hydrodynamic description of the plasma, an ionization dynamics model, and the energy deposition of the incident particle beam. The work done in each of these areas is presented and explained. Due to the complexity of the problem numerical methods are used to obtain results. The code which is being developed is not described here.

The main hydrodynamic assumption is that the plasma can be described using single fluid and temperature equations. This places a constraint on the time scale of the problem. Namely that the electron-ion thermalization time should always be smaller than the hydrodynamic time. This constraint is not serious but should be kept in mind. The model is developed in one dimensional Lagrangian coordinates. This simplifies the conservation equations and allows for simulation of situations where extensive compression or expansion occurs.

The equation of motion (Eq. 3.1) is obtained by performing a force balance on an incremental volume of plasma. The plasma is assumed to be inviscid. The Von Neumann artifical viscosity is introduced to allow finite difference techiques to be used in situations where discontinuities in pressure and density occur.[3.2]

$$\frac{\partial u}{\partial t} = x^{\delta-1} \frac{\partial}{\partial m} \left[P + q \right] + \frac{1}{\rho \delta v} \Delta MOM \qquad (3.1)$$

u - fluid velocity   q - Von Neumann artificial viscosity

P - plasma pressure δv - volume of incremental element

ρ - plasma density   m - Lagrangian mass

ΔMOM - momentum imparted by beam electrons to plasma

δ - 1 for cartesian geometry, 2 for cylindrical, 3 for spherical

The energy conservation equation (Eq. 3.2) is obtained by performing an energy balance on the incremental volume element. It is assumed that Fourier's Law accurately describes the heat transfer. No flux limiter is needed since the electron mean free path is assumed smaller than the temperature gradient. This should be true in the plasmas we are considering. The final form after some manipulation is given below.

$$
C_v \frac{\partial T}{\partial t} + T \left(\frac{\partial P}{\partial T} \right)_V \frac{\partial V}{\partial t} = -q \frac{\partial V}{\partial t} + \frac{\partial R}{\partial t} + \frac{\partial S}{\partial t} + \frac{1}{\rho x^{\delta-1}} \frac{\partial}{\partial x} \left[x^{\delta-1} K \frac{\partial T}{\partial x} \right] \quad (3.2)
$$

T - plasma temperature   V - specific volume
S - energy source to plasma   K - thermal conductivity
C_v - specifc heat at constant volume $( )_V$ - implies at constant volume
R - radiation emitted/absorbed by plasma

The ionization dynamics model is used to calculate the equation of state information that is needed in the hydrodynamic simulation. The parameters of interest are the internal energy, the effective charge, and the radiated power from free-free, free-bound, and bound-bound transitions. This information is obtained in tabular form as a function of temperature and ion density and supplied as input to the hydrodynamics model. In addition, the ionization dynamics model is solved concurrently with the hydrodynamics model to provide current state populations and the plasma spectrum. This arrangement allows the calculation of both spatially and temporally dependent spectra.

The Collisonal-Radiative Equilibrium[3.3] (CRE) model is used to describe the ionization dynamics of the system. This model consists of a set of rate equations, one for each quantum state included, which describe the effect of atomic processes on the population and depopulation of a given state. The model used is an equilibrium model since no time dependence is included in the rate equations.

Our version of the CRE model has a few additional restrictions placed on it. The effects of photon stimulated emission and absorption are not included. This is done to avoid the complication of including radiation transport and having to solve a nonlinear set of equations. The nonlinearity is a result of the direct coupling of the radiation transport and rate equations. The neglect of these effects restricts the applicability of the model to optically thin plasmas.

Lowering of the ionization potential is not explicitly included. This phenomenon

sets a bound on the number of discrete quantum states available. It implicitly affects the model by allowing use of a finite number of states be adequate to describe the plasma.

The atomic processes included in our model are: collisional ionization, three body recombination, collisional excitation, collisional de-excitation, spontaneuos emission, radiative recombination, and dielectric recombination. The rate coefficients are calculated using various methods and the ones we are using were obtained by J.W. Thornhill from D. Duston at the Naval Research Laboratory in Washington, D.C. Recent work by D. Duston summarizes how the rate coefficients were calculated.[3.4]

The model currently includes 56 states. It should be noted that many of these states actually represent several degenerate levels of carbon which have been averaged over the angular momentum and magnetic quantum numbers. The population of the degenerate levels can be recaptured by assuming that they are in equilibrium and using a partition function to extract their populations from the CRE calculated state population.

The final component of our theory is the energy deposition model. The approach is simplistic at the present. The stopping power of an incident relativistic electron is integrated over the plasma. This is then multiplied by the current density of the beam at each point in the plasma to obtain the desired result. The stopping power is based on the work by D. Mosher for relativistic electrons interacting with a plasma which has both free and bound electrons.[3.5] A collision term was found using Fokker-Planck formalism. Assuming the incident beam can be treated as a delta function in momentum space, the appropriate moment of the collison term yields the stopping power (Eq. 3.3). Note that the energy loss due to electron-ion collisions and bremsstrahlung has been ignored.

$$\frac{\partial E}{\partial x} = -4\pi N r^2 \; \alpha_e \; E_o \; \frac{E^2}{E^2 - E_o^2} \tag{3.3}$$

$$\alpha_e = Z_A \ln \left[\beta^2 \gamma (\gamma - 1)^{1/2} E_o / I_z \right] + Z \ln \left[\lambda_D I_z / 2\gamma r E_o \right]$$

$$\beta = v/c \qquad \gamma = E/E_o$$

E - incident electron total energy	N - plasma density
E_o - electron rest mass energy	r - classical electron radius
I_z - ionization energy	λ_D - debey length
Z_A - ion atomic number	Z - effective charge of plasma

... stopping power was found to yield ranges which are in good agreement with ... standard formulas. Thus it is assumed to be accurate enough for the

level of developement thus far. It should be noted that the attenuation of the beam electrons by the plasma is not accounted for when calculating the energy deposition.

Much work is planned and under way to revise the theory and hopefully extend its validity. The hydrodynamic portion of the code is being reveiwed and rewritten so that it is more applicable to describing the experimental configuration. Also subroutines which calculate and output the line emission spectrum are being developed.

In addition the energy deposition model will be reveiwed. The attenuation of the incident electrons as they tranverse the plasma must be accounted for to have a satisifying theory. It is felt that an exponential attenuation might be adequate and consistent with the level of the model's sophistication.

Another problem arises when one attempts to compare with experiment. It is not clear how to calculate the incident beam's current density after a period of time. This information is vital to the energy deposition and the question needs to be addressed. If it becomes possible to measure the current density instead of the current, then the current density could be input directly to the code and the problem circumvented. Also at this time it is felt that most of the energy deposition occurs when the plasma arcs the anode-cathode gap. How to accurately describe the energy deposition during this phase of the experiment needs to be considered for accurate simulation of experimental conditions.

The ionization dynamics model needs to be carefully reveiwed. The CRE model is valid for dynamic plasmas with free electron densities above 10^{18}/cm^3. This threshold is obtained by requiring the relaxation times for atomic processes be shorter than the hydrodynamic time scale. The longest relaxation times are those to ground states and these set the density limit. It desired to describe plasmas with free electron densities below this threshold. The Quasi-Stationary Collisional Radiative Model which retains time dependence in the ground state rate equations might be used to extend to lower density plasmas.[3.6] This is one model which will be considered. Note that if the plasma is static the CRE model would be valid at lower densities.

The adequacy of the number of states used in the model must also be adressed. One method to include additional states is the brute force approach of simply adding them. This approach increases the number of rate equations which must be solved and may become prohibitively expensive from a computational veiwpoint. Another possibility is to use a Partial Local Thermodynamic Equilibrium Model[3.7] This approach uses the reduced ionization potential to find a threshold energy above which the quantum states are in local thermodynamic equilibrium (LTE). One uses the LTE model above this threshold to determine the state populations. Another model such as the CRE is used

below the threshold to obtain populations of the low lying states.

These additions and alterations to the current theory will be reveiwed. The appropriate changes will be implemented where necessary.

4.0) References

1.1 "Microsecond Electron Beam Diode Closure Experiments", R.M. Gilgenbach et. al., Presented at the 1985 IEEE pulsed power conference, Washington D.C., June 3-5, 1985.

1.2 J. Richter in, Plasma Diagnostics, ed. by W. Lochte-Holtgreven (North Holland, Amsterdam, 1968).

1.3 "The Hydrodynamics and Ionization Dynamics of Particle Beam Heated Carbon Ablation Plasmas", Joseph Ward Thornhill, Thesis, University of Michigan, 1985.

1.4 "Nonequilibrium Effects in an Atmospheric Argon Arc Plasma", R.J. Giannaris and F.P. Incropera, J. Quant. Spectros. Radiat. Transfer, 11, 291 (1971).

1.5 Spectrophysics, Anne P. Thorne, (Chapman and Hall, London, 1974).

1.6 "Emission spectroscopy of long pulse relativistic electron-beam-produced argon plasmas",M. L. Brake, T. Repetti, K. Pearce, R. Lucey, J. Appl. Phys., 60, 99(1986).

2.1 F. V. Bunkin, V. M. Bystritskii, V. I. Derzhier, A. N. Didenko, Sov. J. Quantum Electronics, 13, 679(1983).

3.1 see reference 1.3

3.2 J. Von Neumann and R. Richtmeyer, J. Appl. Phys. , 21, 232 (1985).

3.3 see reference 1.2

3.4 D. Duston, R.W. Clark, J. Davis and J.P. Apruzese, Phys. Rev. A , 27, 1441(1983).

3.5 D. Mosher, Physics of Fluids, 18, 846(1975).

3.6 R.W.P. McWhirter in Plasma Physics and Nuclear Fusion Research.

3.7 W. Englehardt, Phys. of Fluids, 16, 217(1973).

5.0) Graduate Students Involved in this Project

Mike Cuneo	Ph.D. Candidate
Ron Kensek	Ph.D. (Dissertation Defended July 1986)
Joe Meachum	Ph.D. (Dissertation Expected January 1987)
Tom Repetti	M.S. Candidate
Sean Wetstone	Ph.D. Candidate

6.0) Dissertations and Publications since May 1986

1. "The Stopping Power for Structured Atomic Projectiles in Cold or Ionized Solids", Doctoral Dissertation, July 1986, Ronald P. Kensek

2. "Effects of helium upon electron beam excitation of N_2^+ at 391.4 and 427.8 nm", presented at the 38th International Conference on Gaseous Electronics, Oct. 7-10 1986, Madison, Wis., M. L. Brake, R. M. Gilgenbach, R. F. Lucey. Jr., K. Pearce, P. E. Sojka, T. Repetti.

3. " Effects of helium upon electron beam excitation of N_2^+ at 391.4 and 427.8 nm", Appl. Phys. Lett., 49, 696(1986), M. L. Brake, R. M. Gilgenbach, R. F. Lucey. Jr., K. Pearce, P. E. Sojka,T. Repetti.

4. "Spectroscopic Sudies of Electron Beam Driven Anode Plasmas", M. E. Cuneo, R. M. Gilgenbach, M. L. Brake, T. Repetti, J. E. Tucker, BAPS, 31,1478(1986).

Effects of helium upon electron beam excitation of N_2^+ at 391.4 and 427.8 nm

M. L. Brake, R. M. Gilgenbach, R. F. Lucey, Jr., K. Pearce, and T. Repetti

Intense Energy Beam Interaction Laboratory. Department of Nuclear Engineering. University of Michigan. Ann Arbor, Michigan 48109

P. E. Sojka

Department of Mechanical Engineering. Purdue University. West Lafayette, Indiana 47907

Relativistic electron beam interactions with very small ratios of nitrogen to helium (10^{-1}–10^{-4}) have been found to produce extremely large N_2^+ ($B^2\Sigma_u^+ - X^2\Sigma_g^+$) intensities at 391.4 and 427.8 nm, compared to line intensities originating from helium. These results occurred in the total pressure regime of 0.1–500 Torr. The pressure scaling results presented here are inconsistent with previously proposed kinetic mechanisms for the N_2^+ laser pumped by helium. With a simple model of the chemical kinetics, we show that this effect is due to the collisional transfer of energy between excited states of helium atoms and the ground state of N_2^+.

It is well known that population inversions of the $B^2\Sigma_u^+ - X^2\Sigma_g^+$ electronic transition of N_2^+ can be achieved in the presence of helium.[1] Two possible mechanisms have been used to describe the pumping process. Collins[1] believes the upper laser level is pumped by charge transfer from He_2^+ to N_2. Kokawa et al.[2] believe that electron impact excitation is the dominant pump mechanism. Most of the research performed on the N_2^+ laser has involved large overall $He-N_2$ discharge pressures (1–36 atm)[1,2] where the presence of He_2^+ may be feasible. Investigations of lower (< 50 Torr) overall pressures, however, have observed population inversions in atomic nitrogen[3,4] rather than in molecular nitrogen. Population mechanisms proposed for atomic nitrogen lasers range from excitation of nitrogen atoms by collisions between metastable excited atoms of helium (2^1S) and nitrogen molecules[3] to the recombination of electron-ion pairs.[4] In this letter, we present intensity measurements for a wide range of helium to nitrogen ratios for relativistic electron beam pumped gases in the intermediate pressure range of 0.1–500 Torr and show that these results are inconsistent with the above mentioned mechanisms. We also present a simple chemical kinetic model which is consistent with our experimental observations.

The experimental apparatus has been described previously.[5] The experiment consisted of a relativistic electron beam at a peak voltage of 300 keV, a peak current of 1 kA, and a pulse width of 300 ns. The diode consisted of a 2.5-cm-diam carbon brush cathode and a 0.025-mm titanium anode foil. The beam was injected into an aluminum vacuum vessel with lucite windows on the sides and end. The emitted light at several helium partial pressures each with nitrogen partial pressures of 0.1, 1, and 10 Torr was sampled axially. The light was analyzed by a 0.275-m spectrograph coupled to an optical multichannel analyzer (OMA). The OMA was gated with pulses of 50 and 500 ns.

For all experiments where helium was present with small to large amounts of nitrogen, two very intense lines were observed at 391.4 and 427.8 nm. These lines correspond to the (0–0) and (0–1) vibrational transitions in the first negative band of N_2^+, $B^2\Sigma_u^+ - X^2\Sigma_g^+$. Lines originating from atomic or molecular helium had negligible intensities for these cases. When no nitrogen was present, the major lines were attributed to neutral atomic helium at 388.8, 447.1, 501.5, and 587.5 nm. In time-resolved studies performed with OMA gates of 50 ns delayed by 20 ns for each pulse, the N_2^+ light emission was found to follow the beam voltage after the initial rise time (see Fig. 1). During the time-resolved studies, no other lines were observed except for the 391.4- and 427.8-nm nitrogen lines. Figure 2 shows the relative intensity of the 391.4-nm band as a function of helium to nitrogen ratio for nitrogen partial pressures of 0.1, 1, and 10 Torr. Figure 3 shows similar results for the 427.8-nm band.

As seen in Figs. 2 and 3, the largest light intensities at 391.4 and 427.8 nm for a given pressure of nitrogen occur for the largest ratio of He/N_2. That is, the more helium present, the more light is produced up to total pressures of about 300 Torr where the intensity levels off. The linear portion of the curves corresponds to a slope of about 1 for the range of total
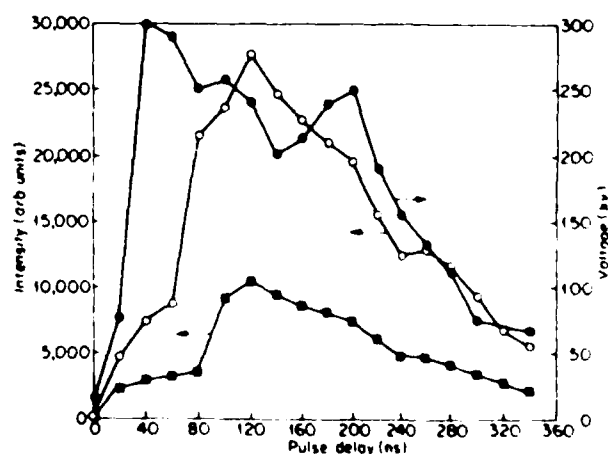

FIG. 1 Beam voltage (●) and 391.4 nm (○) and 427.8 nm (■) emission band intensities as a function of time. The partial pressures of N and helium were 0.5 and 100 Torr. Optical multichannel analyzer gates were 50 ns and times plotted are for the center of the gate.
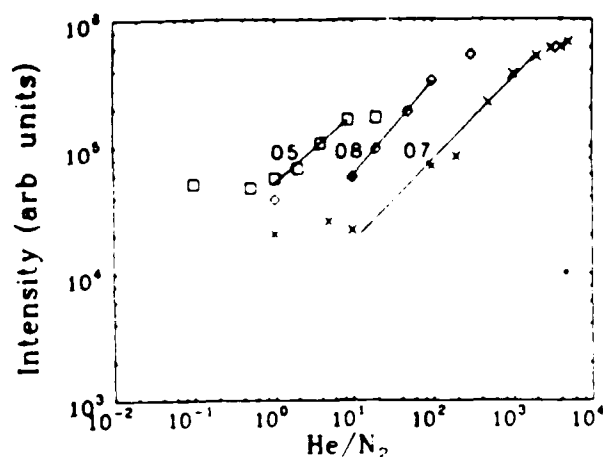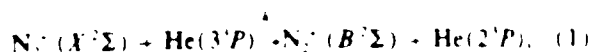
FIG 2 Intensity of the 391 4-nm emission band as a function of He/N ratio for N_2 pressures of 0 1 Torr (×), 1 Torr (◇), and 10 Torr (□) The slopes of the linear portions of the curves are as indicated

pressure 10–300 Torr for the cases where the N_2 partial pressure was 1 and 0.1 Torr The slope was 0.5 when the partial pressure of N_2 was 10 Torr For cases where the helium partial pressure is smaller or about the same as the nitrogen partial pressure, there is very little increase in the intensity of the N_2^+ lines compared to the case of nitrogen alone

As mentioned previously, the largest intensity lines observed when no added nitrogen was present were 388 8, 447.1, 501.5, and 587 5 nm In the case of the 388 8-nm line, the energy of this transition is very close to that of the N_2^+ 391 4-nm band Therefore, a possible mechanism for the excitation of this band is

$$N_2^+ (X^2\Sigma) + He(3^3P) \rightarrow N_2^+ (B^2\Sigma) + He(2^1P), \quad (1)$$

where k_1 is the reaction rate constant Since the slope of the log of the intensity as a function of the log of He/N_2 is close to 1 for the small N_2 partial pressure cases, there appears to be a one to one correspondence between the number of photons emitted for the given bands and the number of helium atoms present, above a particular helium to nitrogen threshold. This one to one correspondence is consistent with reac
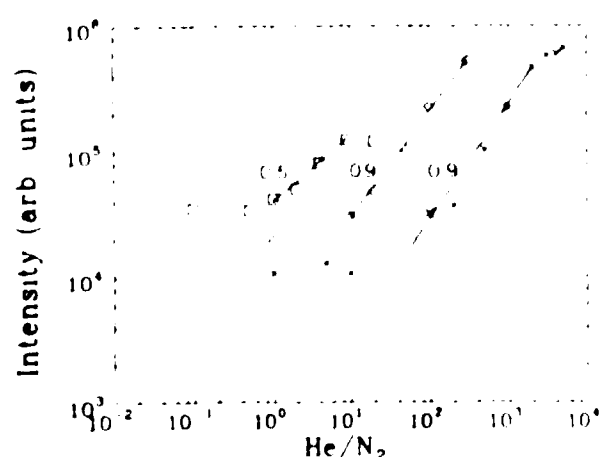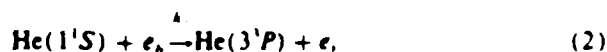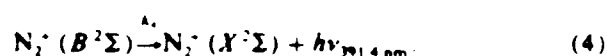

FIG 3 Intensity of the 427 8-nm band emission as a function of He/N ratio for N_2 pressures of 0 1 Torr (×), 1 Torr (◇), and 10 Torr (□) The slopes of the linear portions of the curves are as indicated

tion (1) as illustrated by a simple kinetic model. Assume that the electron beam excites the helium from the ground state to the 3^1S state as follows:

$$He(1^1S) + e_b \rightarrow He(3^3P) + e, \quad (2)$$

where k_2 is the rate constant for reaction (2) and is a function of the electron beam energy. At low pressures, the main deactivation mechanism of He(3^3P) and N_2^+ ($B^2\Sigma$) is radiative decay.

$$He(3^3P) \rightarrow He(2^1S) + h\nu_{388.8 nm}. \quad (3)$$

$$N_2^+ (B^2\Sigma) \rightarrow N_2^+ (X^2\Sigma) + h\nu_{391.4 nm}. \quad (4)$$

Note that He(2^1S) is a metastable state. We also make the following assumptions: all back reactions are negligible, collisional decay of He(3^3P) is unimportant because the exchange reaction He(3^3P) + He(2^1S)→He(2^1S) + He(3^3P) does not alter the He(3^3P) concentration, the collisional quenching of N_2^+ ($B^2\Sigma$) is unimportant for low pressures (although this assumption is discussed later), and that the electron beam density can be approximated by an exponential of the form $[e_b] = [e_b]^0(e^{-u_1 t} - e^{-u_2 t})$ where $[e_b]^0$ is some constant characteristic of the beam density and u_1 and u_2 are constants which describe the beam current temporal profile We now write a differential equation for He(3^3P) as

$$\frac{d[He(3^3P)]}{dt}$$

$$k_2[He(1^1S)][e_b]^0(e^{-u_1 t} - e^{-u_2 t})$$

$$k_3[He(3^3P)] - k_1[He(3^3P)][N_2^+ (X^2\Sigma)] (5)$$

Now assume that the ground state populations He(1^1S) and N_2^+ ($X^2\Sigma$) stay approximately constant Then a linear, homogeneous, ordinary differential equation exists for [He(3^3P)] and can be solved using standard techniques The solution is

$$[He(3^3P)] = A\left(\frac{e^{-u_1 t}}{k - u_1} - \frac{e^{-u_2 t}}{k - u_2}\right) (6)$$

where $k = k_1[N_2^+ (X^2\Sigma)] + k_3$ and $A = k_2[He(1^1S)] \cdot [e_b]^0$ We can also write the rate equation for $[N_2^+ (B^2\Sigma)]$

$$\frac{d[N_2^+ (B^2\Sigma)]}{dt}$$

$$k_1[N_2^+ (X^2\Sigma)][He(3^3P)] - k_4[N_2^+ (B^2\Sigma)] (7)$$

Substituting [He(3^3P)] from Eq (6) and solving for $[N_2^+ (B^2\Sigma)]$ gives

$$[N_2^+ (B^2\Sigma)] = k_1[N_2^+ (X^2\Sigma)][e_b]$$

$$\cdot \left(\frac{(u_2 - u_1)(e^{-k_4 t})}{(k - u_1)(k - u_2)(k_4 - k)}\right.$$

$$\frac{e^{-u_1 t}}{(k - u_1)(k_4 - u_1)}$$

$$\left. \frac{e^{-u_2 t}}{(k - u_2)(k_4 - u_2)}\right) (8)$$

A rate equation for the time rate of change of the photon emission at 391.4 nm can be written as

$$\frac{d[hv_{391.4\,nm}]}{dt} = k_4[N_2^+(B^2\Sigma)].\qquad (9)$$

Substituting the results of Eq. (8) gives

$$\frac{d[hv_{391.4\,nm}]}{dt} = k_2 k_4 k_1 [N_2^+(X^2\Sigma)][He(1^1S)][e_h]^n$$

$$\times\left(\frac{(w_2 - w_1)(e^{-k_1t} - e^{-k_2t})}{(k - w_2)(k - w_1)(k_4 - k)}\right.$$

$$+ \frac{e^{-w_1t} - e^{-k_4t}}{(k - w_1)(k_4 - w_1)}$$

$$\left. - \frac{e^{-w_2t} - e^{-k_4t}}{(k - w_2)(k_4 - w_2)}\right)\qquad (10)$$

Thus, the emission rate for N_2^+ $(B^2\Sigma - X^2\Sigma)$ is linearly proportional to the He ground-state concentration, the electron beam density, and the ground-state population of N_2^+. If collisional quenching of N_2^+ $(B^2\Sigma)$ is included as

$$N_2^+(B^2\Sigma) + M \xrightarrow{k_5} N_2^+(X^2\Sigma) + M,\qquad (11)$$

then k_4 in Eq. (10) would be replaced by $k' = k_4 + k_5[M]$, where M is any collisional partner such as He or N_2. Equation (10) would then have a more complicated dependence upon helium concentration than the simple linear one shown here. Obviously, to best investigate the effects of collisional de-excitation and to remove the assumption that $N_2^+(X^2\Sigma)$ and $He(1^1S)$ remain constant would require accurate rate constants and a computer solution of the differential equations.

Another important result of the data shown in Figs. 2 and 3 is that as the nitrogen partial pressure increases, the overall amount of line enhancement decreases, as well as the slope of the linear part of the intensity versus pressure ratio curves. For nitrogen partial pressures of 0.1 Torr, the emitted intensity increases by almost a factor of 100 whereas for nitrogen partial pressures of 10 Torr, the overall increase is less than a factor of 10 compared to the no helium case. It appears that a very important collisional depopulating mechanism of N_2^+ $(B^2\Sigma)$ is collisions with other nitrogen molecules.

Never at any time was emission due to He_2^+ or postulated He^- (see Ref. 6) observed. This, in addition to the fact that the highest overall pressure examined was 500 Torr, leads to the conclusion that charge transfer between He_2^+ was probably negligible, also since for example the 388.8-nm helium line which populates the metastable state of helium was not observed to increase or decrease with the 391.4-nm band, in contrast to the results of Atkinson and Sanders.[3] Instead, the 388.8-nm helium line was observed only in the absence of nitrogen, thus it is doubtful that direct transfer between the metastable state of helium (2^3S) and the N_2^+ $(B^2\Sigma)$ was significant. Kokowa et al.,[2] claim that electron impact ionization is the major pumping process and that the presence of helium only helps to raise the electron temperature rather than supplying reactants for the pumping process. The results presented here show a definite helium dependency, particularly since we have shown previously[5] that the electron temperature is pressure insensitive for our e-beam produced discharges.

Relativistic electron beam produced plasmas in helium-nitrogen mixtures produce very large intensity lines at 391.4 and 427.8 nm. These lines originate from the vibrational transition of (0–0) and (0–1) in the first negative system of N_2^+. The line intensities increase as the ratio of helium to nitrogen increases. The greatest increase is seen for the lowest nitrogen concentrations. The increased intensity is linear with helium pressure between the total pressure of 10–300 Torr for small partial pressures (0.1–1.0 Torr) of nitrogen. This increase is believed to be due to collisional transfer of energy between helium excited states and the N_2^+ ground state as shown by the agreement between our simple kinetic model and experimental results.

[1] C. Collins, IEEE J. Quantum Electron. QE-20, 47 (1984).
[2] M. Kokawa, M. Saito, S. Horiguchi, and T. Nakaya, J. Phys. D 18, 177 (1985).
[3] J. Atkinson and J. Sanders, J. Phys. B (Proc. Phys. Soc.) Ser. 2, 1, 1171 (1968).
[4] G. Cooper and J. Verdeyen, J. Appl. Phys. 48, 1170 (1977).
[5] M. Brake, T. Repetti, K. Pearce, and R. F. Lucey, Jr., J. Appl. Phys. 60, 99 (1986).
[6] J. Tucker, M. Brake, and R. Gilgenbach, J. Appl. Phys. 59, 2251 (1986).

END

4-87

DTIC